Fall 2021

Cyclic Triaxial Testing to Evaluate Factors Affecting The Unsaturated Cyclic Behavior of a Silty Sand

Zachary R. Howard

CYCLIC TRIAXIAL TESTING TO EVALUATE FACTORS AFFECTING THE UNSATURATED CYCLIC BEHAVIOR OF A SILTY SAND

by

Zachary R. Howard

Bachelor of Science
University of South Carolina, 2020

Submitted in Partial Fulfillment of the Requirements

For the Degree of Master of Science in

Civil Engineering

College of Engineering and Computing

University of South Carolina

2021

Accepted by:

Inthuorn Sasanakul, Director of Thesis

Charles E. Pierce, Reader

Sarah L. Gassman, Reader

Tracey L. Weldon, Interim Vice Provost and Dean of the Graduate School

DEDICATION

To the collective memories of my father, Gregory Russell Howard, my grandfather, Ruben Wright Clark, my cousin, Daniel Alexander Kirk, and my favorite musician, Chester Bennington.

ACKNOWLEDGEMENTS

I would like to thank all of those who have helped me along my academic journey from elementary school through my graduate studies. From my experience in high school, I would like to thank my teachers Mr. Todd Matthews and Mr. Stephen Jeffcoat, for encouraging me to pursue engineering in college. During my time at the University of South Carolina, several professors have granted me insight into civil engineering, namely, Dr. Charles Pierce, Dr. Juan Caicedo, Dr. Inthuorn Sasanakul, Dr. Emad Gheibi, and Dr. Sarah Gassman. I would like to specifically thank my research advisor Dr. Inthuorn Sasanakul for guiding me through the research process and helping me to organize my thesis. Thank you for also being a great teacher in the five courses I have taken with you.

I would like to acknowledge Dr. Muwafaq Awad for conducting the "M-series" tests used in this study. Dr. Awad performed these tests before I started my graduate studies, and he showed me how to perform the unsaturated cyclic triaxial test. It was an honor to continue and complete the work he began. My fellow graduate students Kazi Islam, Pitak Ruttithivaphanich, and Siwadol Dejphumee have assisted me many times in conducting the "Z-series" tests. Their technical support has been valuable during both laboratory work and during data analysis.

I also want to thank my friends and family for supporting me during this research experience. Their support increased my self-confidence and provided me with the energy required to complete the study.

ABSTRACT

This study assesses the cyclic resistance of a non-plastic silty sand, representative of a common mine tailings material. Two series of unsaturated cyclic triaxial tests were conducted, which varied wetting and drying path specimen preparation techniques, initial matric suction, initial net normal stress, and cyclic stress ratio. Specimens prepared using the wetting path experienced significantly higher cyclic resistance than those prepared using the drying path. Specimens that were exposed to higher initial matric suction values experienced higher cyclic resistance than those consolidated with lower initial matric suction values. Initial net normal stress was found to contribute more to specimen cyclic resistance than initial matric suction. Cyclic stress ratios used during the study ranged from 0.20 to 0.35.

TABLE OF CONTENTS

LIST OF TABLES

LIST OF FIGURES

LIST OF SYMBOLS

B	Skempton (1954) pore pressure coefficient
DA_{ε}	Double-amplitude axial strain
D_r	Relative density
e	Void ratio
e_0	Initial void ratio
E	Modulus of elasticity
G	Shear modulus
G_{max}	Maximum shear modulus
k	Increase in cohesion due to matric suction
M	Critical state line
N	Cycle number
p	Net mean stress
p^c	Arbitrary reference mean stress
p_i	Initial net mean stress
p_o	Preconsolidation stress
p_o^*	Base preconsolidation stress at saturated conditions
p_y	Net mean stress at yielding
q_i	Deviator stress applied
r	Infinite stiffness relation term
r_n	Net normal stress reduction ratio
S	Degree of saturation
S_o	Initial degree of saturation
$S_r^d(\psi)$	Degree of saturation for the drying SWCC
$S_r^d(\psi_m)$	Degree of saturation on drying SWCC at matric suction ψ_m.

$S_r^w(\psi)$	Degree of saturation for the wetting SWCC
u_a	Pore air pressure
u_w	Pore water pressure
v	Specific volume
v_o	Initial specific volume
β	Coefficient describing the increase in stiffness with matric suction
γ_{dry}	Dry unit weight
γ_{do}	Initial dry unit weight
$\Delta S_r^d(\psi_m)$	Difference between $S_r^d(\psi)$ and $S_r^w(\psi)$
ε_a	Axial strain
κ	Elastic stiffness parameter used for change in p in the elastic region
κ_s	Compressibility coefficient for increments of suction in the elastic region
λ_s	Compressibility coefficient for increments of matric suction in the plastic region
$\lambda(o)$	Stiffness of a specimen not exposed to suction
$\lambda(s)$	Stiffness of a specimen exposed to suction
ρ_{dry}	Dry density
σ_m	Mean stress
σ'_m	Mean effective stress
σ_n	Net normal stress
σ_{no}	Initial net normal stress
σ'_p	Preconsolidation stress
ψ	Matric suction
ψ_m	Matric suction applied before wetting SWCC is measured
ψ_o	Initial matric suction

LIST OF ABBREVIATIONS

AEV ..... Air Entry Value

ASTM ..... American Society for Testing and Materials

CSR ..... Cyclic Stress Ratio

EOC ..... End of primary consolidation

LC ..... Load collapse

NC ..... Normally consolidated soil

OC ..... Overconsolidated soil

SI ..... Suction increase

SM ..... Silty sand

SWCC ..... Soil water characteristic curve

CHAPTER 1

INTRODUCTION

1.1 – Purpose of Research

Tailings are the unusable rock or soil that results as a by-product of any mining operation. These tailings can range in size from boulders to clay size particles. In mines all over the world, tailings are deposited for long-term storage behind earth embankments, such as the one shown in Figure 1.1. If one of these embankments failed, it would result in a landslide that would devastate the surrounding area. This occurred in January 2019 in Brazil, resulting in 270 human deaths (Nogueira & Plumb, 2020). This disaster is believed to have been caused by flow liquefaction of soils within the tailing dam leading to a significant loss in soil shear strength (Robertson et al., 2019). This event sparked interest in other mining companies to understand the seismic liquefaction behavior of soils that are unsaturated. The soil used in this study is a non-plastic silty sand (SM) that is representative of material stored in tailings embankments.

In saturated soils, the effective stress (σ'), the difference in vertical overburden stress and pore water pressure, is the main contributor to soil shear strength and cyclic resistance. Undrained saturated soils exposed to cyclic loads develop excess pore water pressure (u_w), which reduces the effective stress within the specimen. In specimens that experience a significant reduction in σ' due to the development of u_w during cyclic loading, seismic liquefaction can occur. In the case of saturated specimens tested using a cyclic

Triaxial device, the excess pore water pressure ratio (r_u), the ratio of u_w over the minor effective confining pressure (σ_{3c}'), is used to identify the onset of liquefaction (Idriss & Boulanger, 2008). A r_u value of 1.0 is considered the initiation of liquefaction as the effective stress within the specimen has reduced to zero, leading to a severe reduction in shear strength. Unlike saturated soils, the presence of pore air pressure (u_a) within unsaturated soils causes the determination of effective stress to be less straightforward.

The net normal stress (σ_n), the difference in σ_{3c}' and u_a, is used in this study as this parameter is representative of the effective stress of unsaturated soils. An unsaturated specimen exposed to a cyclic load may experience a severe reduction in σ_n as the excess u_a develops throughout the cyclic load application. The reduction in σ_n can lead to the failure of the specimen in a manner similar to liquefaction in saturated specimens. Unsaturated conditions can exist within mine tailings dams in soils located near the groundwater table (GWT), and a previous study by Troncoso (1990) showed these soils might liquefy during a seismic event. The current understanding of the cyclic behavior of unsaturated tailings material is limited, and further research needs to be completed so the seismic slope stability of tailings embankments can be more accurately predicted.

The findings of this study will be useful for field applications, including seismic slope stability analyses of mine tailings dams and the liquefaction potential of unsaturated soils located in natural, horizontal soil deposits. For instance, a geotechnical engineer can assess the cyclic resistance of unsaturated tailings for both the wetting and drying path. Tailings are deposited in layers over time by pumping, which raises the GWT as shown in Figure 1.1. The addition of a new tailings layer will cause a wetting and drying cycle of the new and the in-situ tailings. Also, rain events can generate a wetting and drying cycle

by raising the GWT as shown in Figure 1.2. The engineer can consider the GWT variation and choose the most conservative cyclic resistance value of the wetting and drying paths for use in the assessment of liquefaction potential in the tailings material. Also, the engineer can consider the change in cyclic resistance with depth due to the increase in σ_n during a slope stability analysis of a tailings dam. In another application, a geotechnical engineer tasked with designing a building foundation in a seismically active region may consider the change in cyclic resistance of soils located near the (GWT) after rain events. The most conservative cyclic resistance should be used when assessing the liquefaction potential of the soils located near the GWT to ensure a safe, functional foundation is designed.

The difference in cyclic resistance of mine tailings between the first wetting and drying cycle after placement is in question. This difference would lead to a difference in design strength parameters used in slope stability analyses. Subsequent wetting and drying cycles show an increase in intrinsic effective stress by the creation of desiccation bonds between soil particles, resulting in higher shear strength and a stiffer stress-strain response (Allam & Sridharan, 1981). For these reasons, during slope stability analysis of tailings embankments, exceptional care must be given to the analysis of the strength parameters corresponding to the wetting and drying cycle. The difference in cyclic resistance of the unsaturated tailings specimen between the wetting and drying stages needs to be explored.

In the process of studying the cyclic resistance of soil specimens in unsaturated cyclic triaxial tests, the initial matric suction and cyclic stress ratio (CSR) needed to cause failure are closely related. Therefore, in order to observe the increase in the number of cycles at failure for increased matric suction values, the CSR must be kept constant throughout the test series. The increase in measured cyclic resistance would represent the

drying of a tailings embankment and the corresponding increasing seismic resistance. The selection of undrained shear strength for the tailings material could then be determined from the expected field matric suction and design CSR.

A constitutive model proposed by Alonso et al. (1990) accounts for increased specimen stiffness for soils exposed to matric suction. The matric suction values for the model ranges from 0 to 300 kPa, while field matric suction values are generally much lower. For this reason, the low matric suction range of 0 to 30 kPa needs special attention during cyclic resistance studies as these are reasonable field matric suction values. The stiffness of specimens with initial matric suction values in the range of 0 to 30 kPa needs to be examined to see if specimens in this range demonstrate a stiffer response.

1.2 – Research Questions

This study seeks to answer four main questions:

1. How does the cyclic resistance of soil deposits differ when exposed to a wetting and drying cycle representative of a change in groundwater table depth?
2. Does the initial net normal stress contribute more to the cyclic resistance of unsaturated soil?
3. For a given net normal stress, how does the variation in matric suction affect the cyclic resistance of an unsaturated soil deposit for a given earthquake magnitude?
4. Does suction hardening exist at the relatively low values of matric suction commonly found in natural unsaturated soil deposits?

1.3 – Research Goal and Objectives

The study seeks to achieve the goal of improving the understanding of the cyclic behavior of unsaturated silty sand affected by several key factors. These factors are wetting and drying processes, initial matric suction, and initial net normal stress.

To achieve this goal, the following objectives are developed through the utilization of two series of unsaturated cyclic triaxial tests:

1. Assess the difference in cyclic resistance of unsaturated specimens prepared using the wetting and drying paths.
2. Determine if initial net normal stress has a higher impact on cyclic resistance than initial matric suction.
3. Evaluate the effects of the variation of matric suction on the cyclic resistance of unsaturated specimens exposed to a constant cyclic stress ratio.
4. Discover if suction hardening behavior exists in specimens exposed to a relatively low range of matric suction.

1.4 – Document Organization

Following Chapter 1, Chapter 2 will provide the current understanding of unsaturated dynamic soil behavior as well as showcase the historical development of unsaturated soil research. Chapter 3 will give a detailed description of the methodology utilized in the study. Chapter 4 will present and discuss the findings of the study. Chapter 5 will provide a summary of the study and offer conclusions based on this work. Recommendations for future research will also be stated.

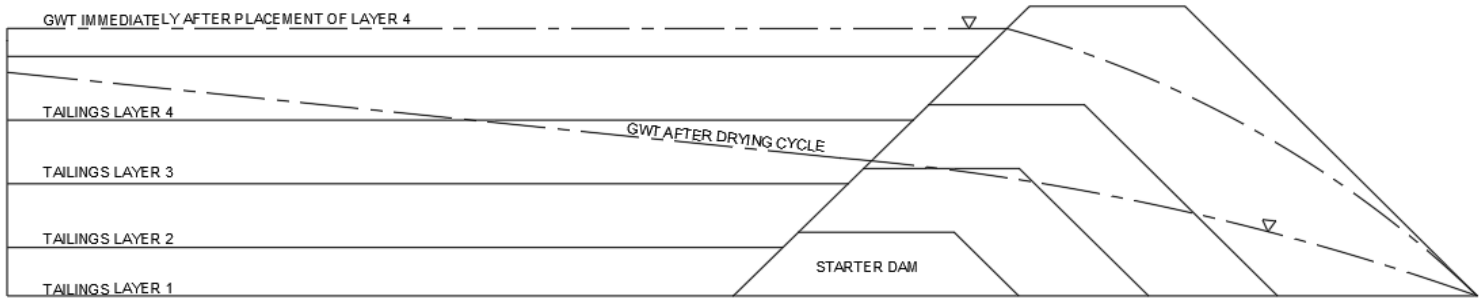

Figure 1.1 – Common tailings dam design with varying GWT

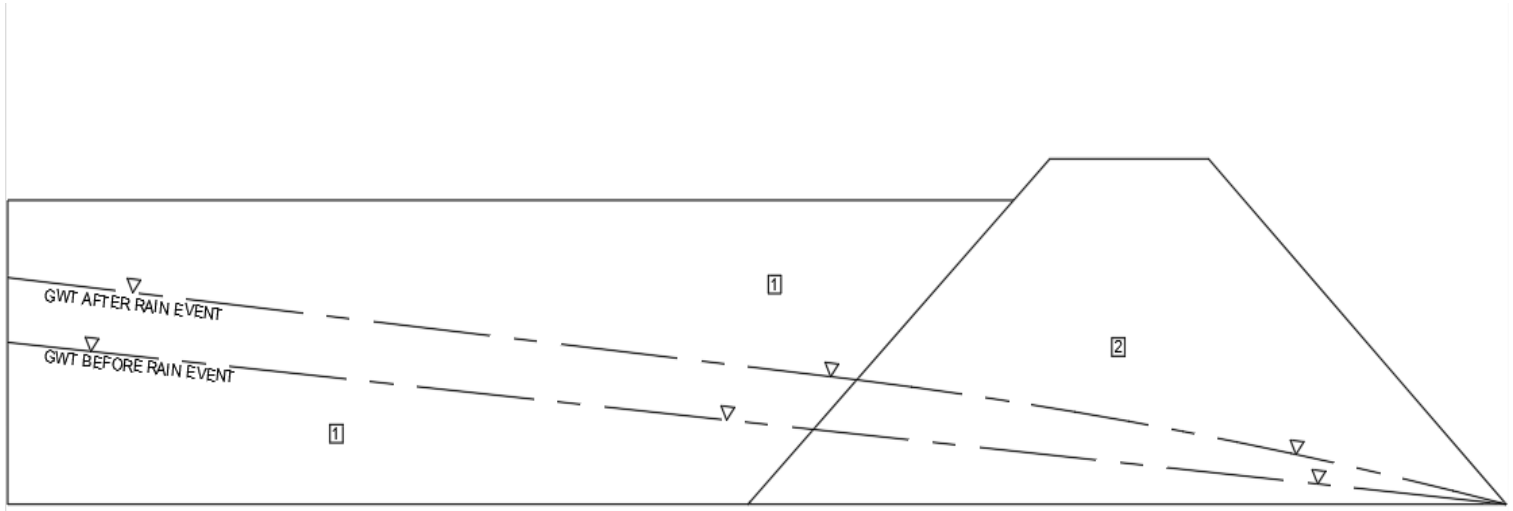

Figure 1.2 - Variation of GWT within tailings dam due to rain

CHAPTER 2

BACKGROUND

2.1 – Soil Saturation and Shear Strength

Soil behavior, particularly shear strength and stiffness, is greatly affected by the degree of saturation (S). Tsukamoto et al. (2014) classified soils as saturated, partially saturated, or unsaturated based on the location of the soils in relation to a ground water table (GWT). Saturated soils possess values of S approaching 100% and are located well below the GWT. Partially saturated soils have values of S less than 100% and can be located up to 5 m below the GWT (Tsukamoto et al., 2014). Unsaturated soils possess values of S less than 85% and are located above the GWT (Tsukamoto et al., 2014). Pore water in the voids of soils creates a pore water pressure (u_w) to develop. Unlike saturated soils, partially saturated and unsaturated soils possess an air phase and a corresponding pore air pressure (u_a). The net normal stress (σ_n), the difference in u_a and u_w, is representative of the effective stress of unsaturated and partially saturated soils. The difference in u_a and u_w, known as the matric suction (ψ), is one of the most important parameters controlling the shear strength and stiffness of partially saturated and unsaturated soils.

As the value of ψ increases, the value of S decreases non-linearly as the pore air in the soil encompasses a larger portion of the total void space. A plot comparing the variation

of S or volumetric water content (θ_w) with ψ is known as a soil-water characteristic curve (SWCC), and Figure 2.1 shows typical SWCCs for sands, silts, and clays (Yeh et al., 2016). In sands, for values of ψ less than the air entry value (AEV), the rate of S change is relatively low. Once the AEV is reached, the rate of S change increases significantly until the residual degree of saturation (S_r) is reached. Further reduction in S after S_r is reached extremely high ψ values. The reduction in S is more gradual for silts and clays, which require higher values of ψ to desaturate.

When a soil experiences a wetting cycle, the shape of the SWCC differs from the shape of the SWCC during a drying cycle. This hysteresis causes the value of S for the wetting cycle to be less than the value of S during the drying cycle for the same value of ψ, as shown in Figure 2.2 (Fredlund & Xing, 1994). The reduced S for the wetting path is commonly attributed to the "ink-bottle effect," which describes how water infiltrating into the soil will have much higher resistance to flow than water flowing out of a soil that is drying (Hillel, 1980). A study by Zhai et al. (2019) proposed Equation 2-1 quantify the magnitude of the hysteresis between the drying and wetting SWCCs, where the parameter $\Delta S_{r,1}(\psi)$ is the difference in saturation for a given matric suction between the two curves. The terms $S_r^d(\psi)$ and $S_r^w(\psi)$ are the degree of saturation for a given matric suction for the drying and wetting curves, respectively. The matric suction applied before the wetting cycle begins represented by ψ_m while $S_r^d(\psi_m)$ is the drying path degree of saturation at ψ_m. Measuring the wetting path SWCC is time-consuming and cost-prohibitive, and Equation 2-2 can be used to estimate the wetting SWCC. Also, denser soil specimens tend to have drying SWCCs that plot above the drying SWCCs of less dense specimens of the same soil (Fredlund & Xing, 1994).

$$\Delta S_{r,1}(\psi) = S_r^d(\psi) - S_r^w(\psi) = [1 - S_r^d(\psi)][S_r^d(\psi) - S_r^d(\psi_m)] \quad (2\text{-}1)$$

Soils along the wetting path also tend to have higher shear strength than those along the drying path. Studies to quantify the shear strength of unsaturated soils exposed to matric suction have yielded different equations for calculating the shear strength (Bishop, 1959; Fredlund & Morgenstern, 1977). The Bishop (1959) study proposed a modification to the classical Terzaghi effective stress equation as shown in Equation 2-2. Equation 2-2 can be inserted into the Mohr-Coulomb failure envelope to provide a solution for shear stress, as shown in Equation 2-3 (Lu & Likos, 2006). The term χ is a function of S and ranges in value from zero for perfectly dry conditions and one for saturated conditions. The use of the Bishop (1959) shear strength relation has been limited due to the difficulty of accurately determining the value of χ (Lu & Likos, 2006).

$$\sigma' = \sigma - u_a + \chi(u_a - u_w) \quad (2\text{-}2)$$

$$\tau_f = c' + [(\sigma - u_a) + \chi(u_a - u_w)] \tan \varphi' \quad (2\text{-}3)$$

Fredlund and Morgenstern (1977) developed a relation for shear stress shown by Equation 2-4 which treats the contributions of σ_n and ψ as separate, independent entities. The first two terms come directly from the classical Mohr-Coulomb failure criterion, and the third term describes the contribution of matric suction to overall shear strength. The parameter φ^b is an additional internal friction angle that accounts for the increased shear strength due to matric suction (Lu & Likos, 2006). Similar to the Bishop (1959) relation, due to the difficulty of determining φ^b experimentally and the uncertainty of φ^b over a wide range of saturation, it has led to the Fredlund and Morgenstern (1977) shear strength equation receiving limited practical use (Lu & Likos, 2006).

$$\tau_f = c' + (\sigma - u_a)\tan\varphi' + (u_a - u_w)\tan\varphi^b \quad (2\text{-}4)$$

A study by Lu and Likos (2006), in an attempt to develop an equation for effective stress in unsaturated soil, developed the concept of "suction stress" (σ^s). Their study grouped interparticle forces into three types. Type I forces include active skeletal friction forces between the soil grains (Lu & Likos, 2006). Type II forces include concentrated forces at the particle contact points. These include electrical double-layer forces, van der Waals forces, cementation forces, surface tension, and negative pore water pressure forces, the combined effect of which is considered the suction stress (Lu & Likos, 2006). Type III forces are the equal and opposite forces counteracting the forces of Types I and II. The suction stress characteristic curve (SSCC) is the relation between matric suction (ψ), volumetric water content (θw), or S and σ^s (Lu & Likos, 2006). Equation 2-5 relates these factors together in mathematical form (Lu & Likos, 2006).

$$\sigma^s = f(u_a - u_w) = f(S) = f(\theta_w) \quad (2\text{-}5)$$

In a plot of σ^s versus S or θw, the SSCC follows a similar shape to the SWCC, where as σ^s increases, S or θw decreases. However, in a plot of σ^s versus ψ, as ψ increases, σ^s also increases in a non-linear fashion (Lu & Likos, 2006). The SSCC can be used to find net interparticle stress (σ_c) at a given matric suction using Equation 2-6 where σ_t is the total overburden stress and σ_{co} is the apparent tensile stress at in the saturated state (Lu & Likos, 2006). The parameter σ_{co} is estimated as the apparent effective cohesion (c') divided by the tangent of the effective friction angle (φ') as shown in Equation (2-7) (Lu & Likos, 2006).

$$\sigma_c = \sigma_t - u_a + \sigma^s + \sigma_{co} \quad (2\text{-}6)$$

$$\sigma_{co} = \frac{c\prime}{\tan\varphi\prime} \quad (2\text{-}7)$$

The study conducted by Lu et al. (2010) developed a closed-form equation for the suction stress (σ^s) based on the Genuchten (1980) SWCC model as shown in Equation 2-8. The parameter α is equal to the inverse of the air entry value (AEV), and n is based on the pore size of the soil (Lu et al., 2010). Guidance for selecting α and n values for soils is given by (Guber & Pachepsky, 2010). Equation 2-6 simplifies to Equation 2-9 when Equation 2-8 is inserted (Lu et al., 2010). In Equation 2-9, σ' represents the effective stress of the unsaturated or partially saturated soil, and σ_t is the total overburden stress.

$$\sigma^s = -(u_a - u_w)\left(\frac{1}{1+[\alpha(u_a-u_w)]^n}\right)^{1-\frac{1}{n}} \quad (2\text{-}8)$$

$$\sigma' = (\sigma_t - u_a) - \sigma^s \quad (2\text{-}9)$$

The shear strength of unsaturated and partially saturated soils can be determined using suction stress as shown in Equation 2-10 (Oh et al., 2013). In triaxial conditions, the mean stress is defined as, $p' = (\sigma_1+2\sigma_3)/3$ and the deviatoric stress is defined as $q = \sigma_1 - \sigma_3$. The parameter d is the isotropic tensile stress at saturated conditions or the y-axis intercept in p-q space. The term M is the slope of the failure envelope in p-q space and q_f is the deviatoric shear stress at failure (Oh et al., 2013).

$$q_f = d + M(p - u_a)_f - M\sigma^s \quad (2\text{-}10)$$

There is no consensus on the most appropriate method for determining the effective stress and, therefore, shear strength of unsaturated soils. However, the Lu et al. (2010) suction stress equation has seen significant use in recent years (Rong & McCartney, 2021; Ghayoomi et al., 2017; Oh et al., 2013). Further studies need to be conducted in order to

determine the most robust approach to finding the effective stress of partially saturated and unsaturated soils.

2.2 – Stiffness Variation in Unsaturated Soils

Unsaturated soils have stiffness values that vary based on matric suction and wetting and drying cycles. In a study utilizing resonant column tests and isotropic compression tests on unsaturated Bonny silt, Khosravi et al. (2016) found that specimens following the wetting path of the SWCC experienced a stiffer response than those following the drying path. The study found that the maximum small-strain shear modulus (G_{max}) increased with higher matric suction. Higher magnitudes of G_{max} were observed along the wetting path of the SWCC. The results from the isotropic compression tests show the mean preconsolidation stress (σ_p') increased by 50% with an increase in matric suction from 0 to 55 kPa. However, when the samples were rewetted and taken from a matric suction of 71 kPa to 45 kPa, the mean σ_p' decreased from an unspecified value to 1,110 kPa, a mean σ_p' value higher than the mean σ_p' observed during drying. A higher mean σ_p' value during wetting explains the higher specimen stiffness for the specimens of the current study.

Soils exposed to matric suction experience an increase in stiffness (Ghayoomi et al., 2017; Alonso et al., 1990; Khosravi et al., 2016). A constitutive model has been developed to predict the increase in specimen stiffness with matric suction (Alonso et al., 1990). While the matric suction values used in the Alonso et al. (1990) study were much greater than the matric suctions used in this study, both studies found an increase in specimen stiffness for increased matric suction. The Alonso et al. (1990) model shows how

unsaturated soils exposed to matric suction develop a preconsolidation stress (p_0) that increases with higher matric suction from a base preconsolidation pressure at saturated conditions (p_0*). Essentially, a normally consolidated (NC) unsaturated soil will begin to act as if it is over-consolidated (OC) when suction hardening occurs. The net mean stress is the difference between the mean stress and the pore air pressure (u_a) ($p = \sigma_m - u_a$), which is the same as the net normal stress. The mean stress is defined in a general case as ($\sigma_m = (\sigma_1+\sigma_2+\sigma_3)/3$). For triaxial testing, the intermediate and minor principle stresses are equal, leading to a simplification ($\sigma_m = (\sigma_1+\sigma_3)/2$). When the net mean stress (p) is plotted against matric suction (s), referred to as (p- s) space, the p_0 for given soil increases non-linearly from p_0* to a yielding net mean stress value (p_y). The study proposed a yield curve constitutive model to describe the path quantitatively in between p_0* and p_y, and this is shown in Equation 2-11 (Alonso et al., 1990).

$$\left(\frac{P_0}{P^c}\right) = \left(\frac{P_0^*}{P^c}\right)^{\frac{\lambda(0)-\kappa}{\lambda(s)-\kappa}} \tag{2-11}$$

The curve developed by this equation best represents the wetting path behavior of soil specimens. Wetting specimens were shown to experience collapse phenomena upon loading, and for this reason, the curves developed using Equation 2-11 are referred to as load-collapse (LC) curves. Conversely, the suction-increase (SI) yield curve is a horizontal line in p-s space which intersects the LC curve at high values of p. The interaction between the LC and SI curves is shown in Figure 2.3.

The parameters $\lambda(s)$ and $\lambda(0)$ represent the slope of a straight line plotted on a ln(p) vs specific soil volume ($v = 1 + e$) graph. The parameters $\lambda(s)$ and $\lambda(0)$ are shown in Figure 2.4, and these are stiffness parameters that describe the change in specific volume for a

change in p for an unsaturated specimen. The term λ(s) represents the stiffness of a specimen exposed to matric suction, while λ(0) represents the stiffness of a specimen not exposed to matric suction. The study developed Equation 2-12 in order to approximate λ(s) (Alonso et al., 1990).

$$\lambda(s) = \lambda(0)[(1 - r)\exp(-\beta s) + r] \tag{2-12}$$

λ(0) is larger than λ(s), showing how specimens not exposed to suction experience more volume change and are therefore less stiff than specimens not exposed to suction. Unlike the elastic modulus (E), which is larger for more stiff materials, λ(s) is smaller for more stiff materials as the volume change for specimens exposed to matric suction is smaller than the volume change for specimens not exposed to matric suction. The term (κ) is an elastic stiffness parameter that is used for changes in p within the elastic region. The term (p^c) is an arbitrary reference mean stress selected by the experimenter. The parameter (β) is a term that describes the increase in stiffness with matric suction. The term (r) is a constant that relates the maximum stiffness at an infinite matric suction with the stiffness of soil with no matric suction. This term is described by Equation 2-13.

$$r = \lambda(S \to \infty)/\lambda(0) \tag{2-13}$$

Also, the maximum past suction for the soil specimen (s_0) is considered the boundary between the elastic and plastic ranges. The terms p_0*, p_y, v, λ(0), κ, β, r, and S_0 must be determined experimentally. Even though the Alonso et al. (1990) study utilized matric suctions at magnitudes ten to one hundred times greater than the matric suctions used in this study, the principle of increased specimen stiffness due to matric suction can be seen in the results of this study.

Even though this study did not utilize the constitutive model proposed by Alonso et al. (1990), the parameters required for the implementation of the model are described in four groups, a) through d) which can be used to develop LC curves for the soil of this study. Group a) includes the parameters needed to describe the initial stress state. These are the initial net mean stress (p_i), the deviator stress applied (q_i), initial matric suction (s_i), initial specific volume (v_0), initial preconsolidation stress at zero suction (p_{0i}*), and initial maximum past suction (s_{0i}). Group b) includes parameters directly related to the loading-collapse (LC) yield curve, which are p^c, $\lambda(0)$, κ, r, and β. Group c) are terms that correspond to the SI yield curve. These are the compressibility coefficient for increments of matric suction in the plastic range (λ_s) and the compressibility coefficient for changes in suction in the elastic region (κ_s). Group d) includes parameters associated with shear stress and shear strength. These are the shear modulus (G) within the elastic range, the slope of the critical state line (M), and the coefficient that controls the increase in cohesion with matric suction (k). Once the beforementioned terms are determined, the LC and SI yield curves can be developed. These curves can be used to predict the suction-hardening behavior of soil specimens such as the ones tested in this study. However, time did not permit the determination of the parameters required to develop the LC and SI curves for the silty sand studied. This is an area of possible future research.

2.3 – Dynamic Behavior of Unsaturated Soils

Unsaturated and partially saturated soils often experience dynamic loads from earthquakes such as the 2011 Great East Japan Earthquake (Tsukamoto et al., 2014). Unsaturated soils are also exposed to vibratory loads from machine foundations such as wind turbines (Fang & Gazetas, 1991). When exposed to dynamic loads, unsaturated and

partially saturated soils have been shown to experience liquefaction, a severe reduction in shear strength and stiffness where the soil begins acting as a liquid as opposed to a solid mass (Tsukamoto et al., 2014). A study by Unno et al. (2008) defined liquefaction in unsaturated and partially saturated soils as the development of excess u_a and u_w, which equal the initial confining stress in triaxial conditions. The cyclic stress ratio (CSR) is the applied shear stress experienced by soil during cyclic loading divided by the vertical effective stress (σ_v'). The CSR is representative of the magnitude of the applied cyclic stress, which leads to the build-up of u_a and u_w and to possible liquefaction of partially saturated and unsaturated soils. Specifically for unsaturated soils in triaxial conditions, the CSR is defined by Equation 2-11 where $\Delta\sigma$ is the applied deviator stress, and σ_{no} is the initial net normal stress (Tsukamoto et al., 2014). The cyclic resistance ratio (CRR) is the CSR required to achieve liquefaction in a specific number of cycles (Idriss & Boulanger, 2008). The study by Tsukamoto et al. (2014) defined the CRR as the CSR necessary to cause a double-amplitude axial strain (DA_ε) of 5% after 20 cycles. As the relative density and effective confining stress increase, the CRR also increases (Idriss & Boulanger, 2008).

$$CSR = \frac{\Delta\sigma}{2\sigma_{no}} \tag{2-11}$$

Dynamic axial strain behavior of soils is crucial to the design of foundations in seismically active regions. In the event an earthquake caused a large axial compression of a foundation soil supporting a building, the building would experience settlement which may lead to serviceability or structural failure. Furthermore, differential settlement caused by dynamic loads may lead to differential settlement of foundations which can cause structural failure. During the 1964 Niigata earthquake in Japan, apartment buildings experienced differential settlements of their foundations after the foundation soils

liquefied, causing the apartment buildings to overturn (Idriss & Boulanger, 2008). This reiterates the importance of understanding the dynamic axial strain behavior of foundation soils. Double-amplitude axial strain (DA_ε) is the absolute value of the difference between the maximum axial strain in compression and the maximum axial strain in extension. The Tsukamoto et al. (2014) study used a DA_ε of 5% to identify the number of cycles required to cause soil liquefaction during a series of cyclic triaxial tests.

Cyclic damping is the portion of energy input into an object that is dissipated. For soils, the damping ratio is not constant for soils, and it is known that cyclic damping increases with increased axial strain. In a plot of axial strain and CSR, the cyclic loading and unloading pattern creates a hysteresis loop that grows in an area with increased axial strain. The area inside the hysteresis loop is representative of the damping of the specimen.

An accurate value of the dynamic shear modulus (G) is required for evaluating the response of soils to dynamic loads (Ghayoomi et al., 2017). The stiffness of soils in shear is represented by G, which decreases with increased shear strain (γ). A study by Ghayoomi et al. (2017) conducted a series of cyclic triaxial tests on unsaturated sand and found G varied with the degree of saturation (S) and matric suction (ψ). The value of G decreases with increased S while G increases for increased ψ. The Ghayoomi et al. (2017) study normalized the maximum shear modulus (G_{max}) measured for specimens exposed to different values of matric suction by dividing the measured G_{max} by the square root of the mean effective stress. This was done to observe the increase in G_{max} due to increased matric suction without the influence of mean effective stress. The value of G decreases with increased S while G increases for increased ψ as shown in Figure 2.5. However, the Ghayoomi et al. (2017) study did not specifically analyze the magnitudes of the

contributions to cyclic resistance provided by increased initial net normal stress and initial matric suction.

2.4 – Laboratory Dynamic Behavior Measurement

Laboratory testing programs have been conducted to study the dynamic properties of partially saturated and unsaturated soils, including CSR, CRR, volumetric strain, axial strain, dynamic shear modulus, and excess pore pressure development leading to liquefaction (Ghayoomi et al., 2017; Sawada et al., 2006; Tsukamoto et al., 2014; Rong & McCartney, 2021). Common laboratory tests for assessing the liquefaction behavior of soils are cyclic triaxial tests and cyclic simple shear tests (Sawada et al., 2006; Rong & McCartney, 2021). These tests typically utilize a loading pattern that is regular with a constant load amplitude and frequency. A plot of time versus applied load for one of these tests would appear sinusoidal. A typical triaxial device used for cyclic triaxial tests is shown in Figure 2.6. These devices apply cyclic axial deviator stress ($\Delta\sigma$) to a cylindrical soil specimen. A cell confining pressure (σ_3) is applied to the specimen during a consolidation stage before the triaxial test is conducted. While customized triaxial equipment has been developed for volume measurements, such as the apparatus utilized by Sawada et al. (2006), the triaxial device used in the current study does not have the ability to directly measure specimen volume change.

Cyclic simple shear devices such as the one utilized by the Rong and McCartney (2021) study utilize a cylindrical soil specimen that is confined within a wire-reinforced rubber membrane. Vertical stress is applied to the specimen from above while a shear force is applied horizontally, generating shear stress within the specimen. The cyclic simple shear device is more representative than a cyclic triaxial test in replicating an earthquake

shearing motion as the cyclic simple shear device shears the specimen horizontally in a fashion similar to the horizontal displacement induced by an earthquake shear wave. Due to the presence of the wire reinforcement in the specimen membrane, the specimen diameter is considered constant throughout the test. Vertical deformation is measured throughout the test, and therefore the volume of the specimen can be computed at any given cycle.

The cyclic frequency applied during testing is an important consideration in the study of unsaturated soil cyclic behavior. The Tsukamoto et al. (2014) study utilized a cyclic frequency of 0.05 Hz in their unsaturated cyclic triaxial test series. This frequency was selected as the frequency is high enough to replicate an earthquake vibration while also being low enough to allow for equal pore water pressure distribution throughout the specimen (Tsukamoto et al., 2014). Due to the success of this frequency in the Tsukamoto et al. (2014) study, the frequency of 0.05 Hz was used in the current study.

2.5 – Volume Change Behavior of Unsaturated Soils

Seismic compression of soils often occurs in soils during earthquakes as contractive volumetric strain is developed due to the cyclic shearing motion of the earthquake (Rong & McCartney, 2021). The Rong and McCartney (2021) study measured volumetric strain during undrained cyclic simple shear tests and found seismic compression is most closely related to the change in mean effective stress as the specimen which experienced the greatest amount of seismic compression also experienced the largest decrease in mean effective stress. The Rong and McCartney (2021) study also found seismic compression followed a non-linear trend with increasing initial degree of saturation (So), with the largest seismic compression occurring in an intermediate range of S_o of 30% to 45%. Specimens

with an initial degree of saturation outside this range experienced smaller seismic compressions (Rong & McCartney, 2021). This behavior contradicts the findings of the drained cyclic simple shear tests conducted by Rong and McCartney (2020), which showed seismic compression increased linearly with an increased initial degree of saturation. These findings show how during a liquefaction analysis of soil, a wide range of initial degrees of saturation should be studied, and the drainage condition of the soil needs to be evaluated.

The response spectra of earthquakes are irregular. For instance, when ground acceleration measured during an earthquake is plotted against the time duration of the earthquake, the wave does not follow a regular, sinusoidal pattern. A study by Sawada et al. (2006) conducted a series of undrained cyclic triaxial tests on silty sand (SM) using an earthquake response spectrum measured during the Geiyo earthquake of 2001. Since the response spectrum was not symmetrical, a specimen was tested with the maximum deviator stress ($\Delta\sigma$) directed in axial compression (CM) while an identical specimen was tested with $\Delta\sigma$ directed in axial extension (EM) (Sawada et al., 2006). The initial degree of saturation (S_o) of the specimens tested were 50, 75, and 100%. The study found unsaturated specimens with S_o of 50% experienced more contractive volumetric strain during the undrained cyclic shearing than the specimens with S_o of 75 and 100%. The main contribution to the contractive volumetric strain was the compression of pores within the specimens (Sawada et al., 2006).

2.6 – Tailings Storage Application

Tailings are a mixture of crushed rock and fluids which remain after the removal of valuable commodities from mined material. Tailings are produced by several different extraction industries, including those which mine precious metals, base metals such as iron,

oil sands, and uranium (Kossoff et al., 2014). It is common in the mining industry to store tailings within an impoundment created behind an earth dam which can fail, leading to significant environmental impacts and large losses of life (Kossoff et al., 2014; Nogueira & Plumb, 2020). Tailings are often stored in impoundments in excess of 100 meters in height and are often poorly compacted and can be unsaturated (Robertson et al., 2017). Slope stability during static and seismic loading events is a major design consideration for tailings dams as a loss in shear strength could endanger the lives of individuals living downslope of the facility.

Tailings are generally angular to very angular, leading to a high effective angle of internal friction (φ') (Mulligan, 1996). The grain size of tailings varies significantly for clay to boulder size particles; however, a study by Sarsby (2000) defined hard rock tailings as mostly gravel and clay free, with a vast majority of the material being classified as sand instead of silt (Kossoff et al., 2014). The specific gravity of tailings varies based on the parent rock mineralogy and ranges between 2.60 and 2.80 (Sarsby, 2000).

Tailings dams are constructed in stages as subsequent layers of tailings are impounded behind the dam. Tailing dams typically consist of locally sourced materials instead of concrete (Kossoff et al., 2014). The initial starter dam is generally constructed of local soils; however, the subsequent layers of the tailings dam are often made of waste rock from the mining operation or of the tailings themselves. The tailings are typically pumped from the mine mill into the impoundment as a slurry with larger particles being placed near the upstream dam face while finer particles form a low permeability barrier which reduces the piping and seepage across the dam (Kossoff et al., 2014). This placement

process can lead to the presence of unsaturated soils within the soil mass, which can experience wetting and drying cycles (Kossoff et al., 2014).

Tailings dams typically fail during the active stage, when additional tailings material is being continually added (Kossoff et al., 2014). Rico et al. (2008), in a study of European tailings dam failures, 83% of the dams failed during the active stage as opposed to 17% that failed during the inactive stage, after the tailings dam is no longer expanded. Oxidation of the tailings material in the unsaturated zone creates cementation, which is likely the factor contributing the most to inactive tailings dam slope stability. Troncoso (1990) proposed that cementation of tailings material may increase the seismic resistance of the tailings by up to 250% over an extended time period. In seismically active regions, the greatest danger for tailings dams is earthquakes (Kossoff et al., 2014). At least 6 tailings, dams failed during an earthquake in Chile in 1965 (Dobry & Alvarez, 1967). For this reason, a comprehensive understanding of the seismic behavior of tailings material is required for safe and economical tailings dam designs. Currently, few studies have assessed the cyclic behavior of unsaturated tailings, and this area needs to receive more attention due to the risks associated with tailings dam slope failures.

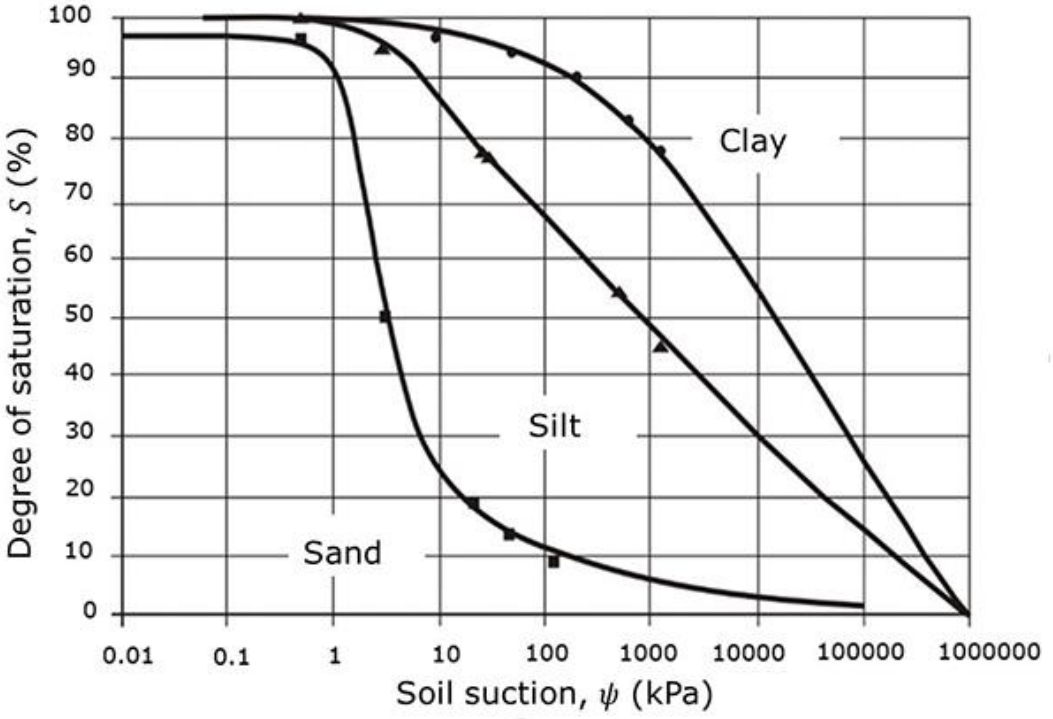

Figure 2.1 – Typical SWCCs (Adapted from Yeh et al., 2016)

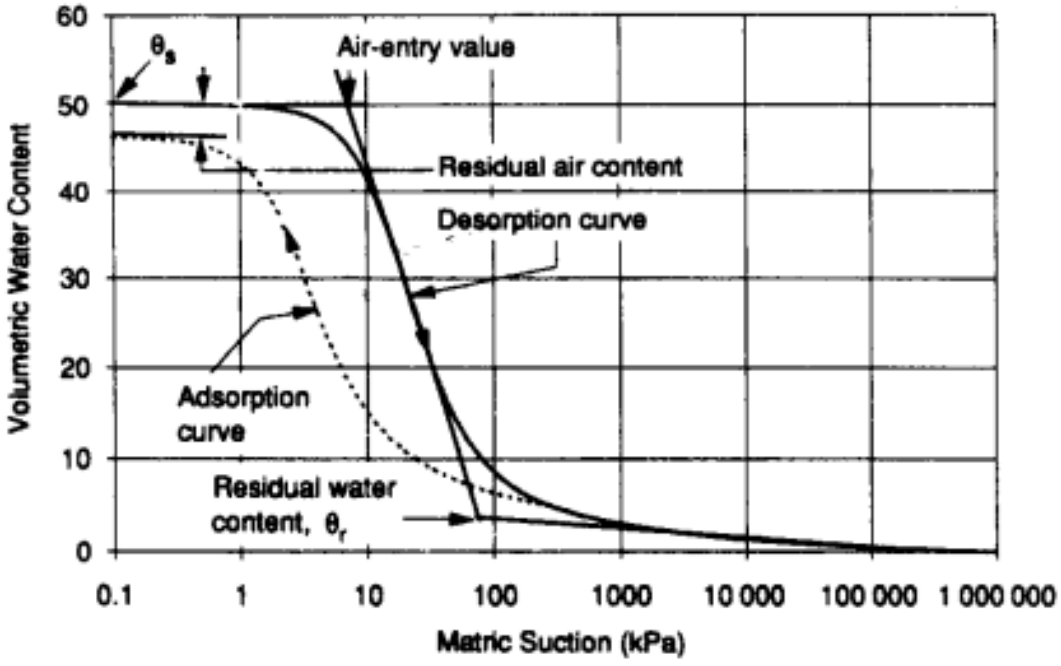

Figure 2.2 – Wetting and drying SWCCs (from Fredlund & Xing, 1994)

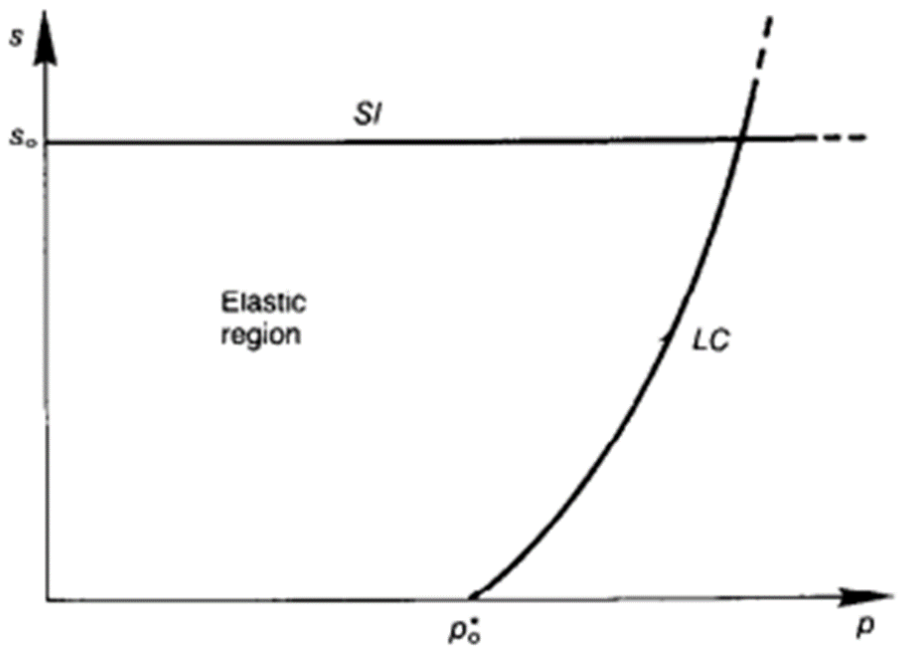

Figure 2.3 – Relation between the loading-collapse (LC) yield curve and suction-increase (SI) yield curve. From Alonso et al. (1990).

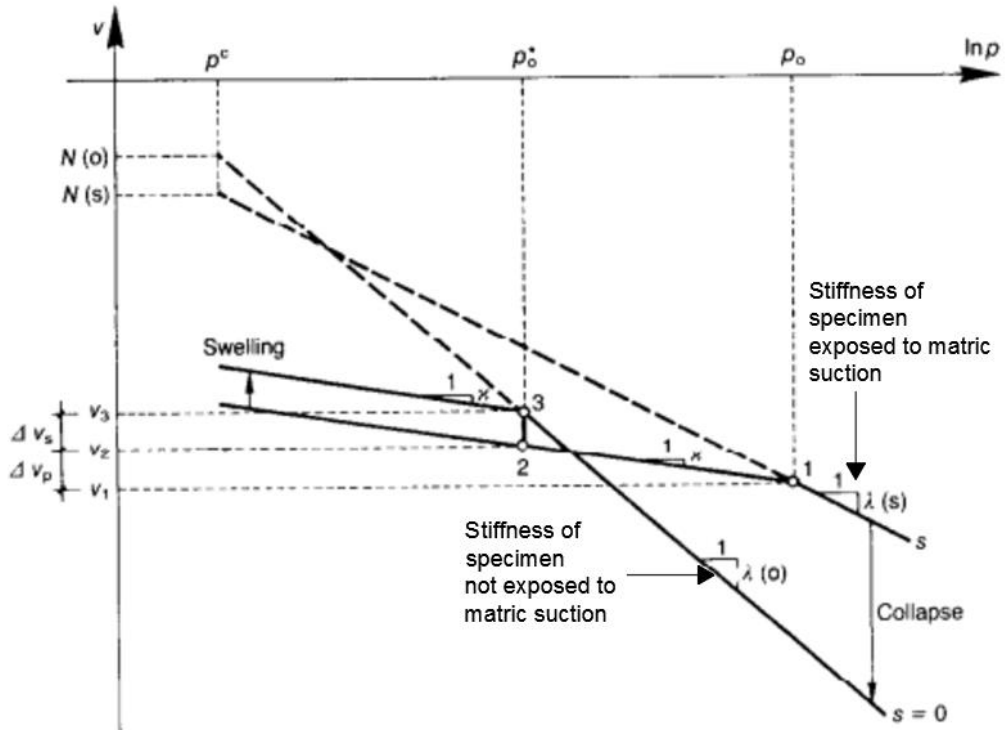

Figure 2.4 – The relation between the increase in net mean stress (p) and specific volume (v). Adapted from Alonso et al. (1990).

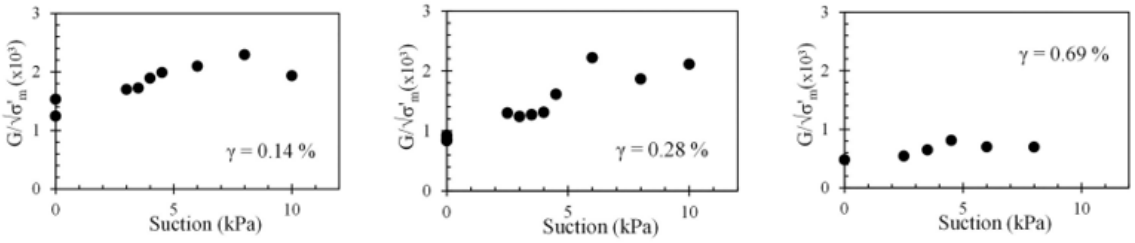

Figure 2.5 – Matric suction versus the normalized shear modulus (Adapted from Ghayoomi et al., 2017)

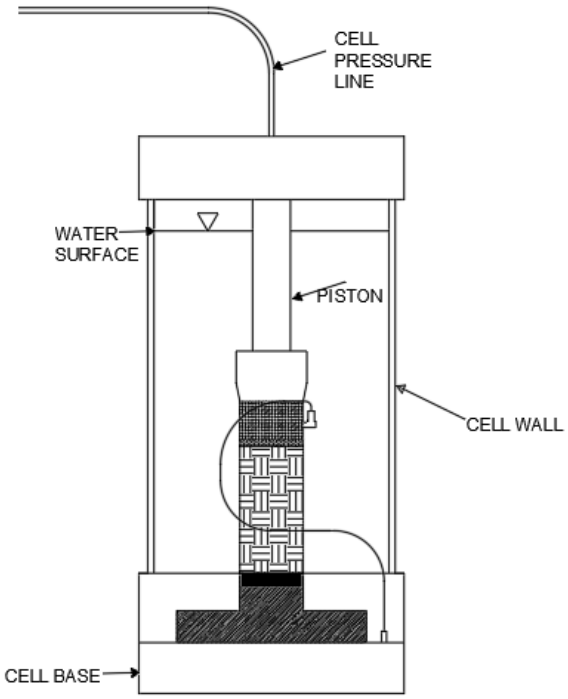

Figure. 2.6 – Triaxial cell components.

CHAPTER 3

METHODOLOGY

3.1 – Introduction

The following is a rigorous, detailed description of the entire process required to conduct a proper unsaturated cyclic triaxial test. Required equipment preparation procedures are described in sections 3.2 through 3.4, while specimen preparation procedures are described in sections 3.5 through 3.8. Sections 3.6 and 3.7 apply to the drying path specimen preparation method, while the wetting path method does not include these procedures. The unsaturated cyclic triaxial test and specimen removal are described in sections 3.9 and 3.10, respectively. Analysis of the collected data and figure preparation are described in section 3.11.

The equipment utilized in the study was an Enterprise Level Dynamic Triaxial Testing System (ELDYN) developed by GDS Instruments. The ELDYN consists of a load frame, an electric driving motor, a triaxial cell, a back pressure tank, an air pressure tank, a cell pressure pump, and a data acquisition pad. The components of the ELDYN system are shown in Figure 3.1. Small diameter flexible plastic hoses were used to connect the cell pressure pump, the back pressure tank, and the air pressure tank to the triaxial cell. Cables delivered the pressure values measured by the pressure sensors used in the ELDYN system to the data acquisition pad, which relayed the data to the desktop computer. De-aired water was required for use in the triaxial test, and the de-aired water was produced through the

use of a de-aired water vacuum tank. The procedure of producing de-aired water is described in section 3.2.

3.2 – Filling the De-aired Water Tank

Unsaturated triaxial testing utilizes a porous ceramic disk with a very low air entry value. This ceramic disk must be saturated with water before specimen preparation can begin; otherwise, the specimen cannot be saturated. If typical tap water is used in the saturation of the ceramic disk, dissolved air in the water would prevent the entire void space of the ceramic from being filled with water. This would lower the permeability of the ceramic and significantly increase the time required to prepare the unsaturated soil specimen. De-aired water has had nearly all dissolved gases removed from the fluid. The dissolved gases are removed via a vacuum applied to the fluid while the water is spun by a rotary pump. The process of producing de-aired water is shown in Figure 3.2.

To begin, a purple water line is run across the ceiling of the laboratory connecting the water source to the vacuum tank. The water valve next to the tank is opened, and tap water flows into the tank. A black line on the tank wall represents the maximum fill line. Filling the tank above this mark will lead to water spilling out of the tank. Once filled, the rotary pump is activated to spin the water, and the white air line that allows the tank to vent to the atmosphere has to be closed in order to generate a vacuum. After the tank is sealed from atmospheric pressure, the vacuum pump located in the main geotechnical laboratory room is turned on, and the vacuum pump must read ~-27 in-Hg. Upon inspection of the vacuum tank, one can see hundreds of air bubbles form in the fluid. After 15 minutes, nearly all bubbles have disappeared. However, one should maintain the vacuum for 20 minutes to ensure as much air is removed as possible. After the 20 minutes end, the vacuum

pump is turned off, and the air line is opened to the atmosphere, and the valve connecting the vacuum tank to the de-aired water tank is opened. One can place ~2.5 vacuum tank volumes in the de-aired water tank before the elevation difference equalizes. This is more than enough de-aired water required for the test.

The valve connecting the vacuum tank and the de-aired water tank must be kept closed while the vacuum is in effect. Having the valve open can cause the water in the de-aired water tank to overflow the vacuum tank, which could damage the vacuum pump.

3.3 – Filling the Back Pressure Tank

The back pressure tank is used in every phase of the test and must be continually re-filled. The end of the de-aired water tank line is unscrewed and connected to a t-connector. The researcher places a finger on the end of the t-connector, as shown in Figure 3.3. The t-connector is rotated so that the opening is pointing upward. Water flows out of this opening, and when no air bubbles are visible, the cap is screwed on. The back pressure is set to 0, as shown in Figure 3.4. Assuming a small amount of water is in the tank, the device is unlocked, the “slow empty” option is selected, and the remaining opening in the t-connector is filled with water. When no air bubbles are visible, the nut is tightened, and the “STOP” button is pressed on the controller. The slow fill option is selected, and the tank is allowed to fill. The tank will stop filling automatically when it is filled.

The t-connector is disassembled, and a cap is placed in the de-aired water line. The back pressure line is attached to the center front valve by using the slow empty option to flush the connection with water and displace air in the valve. The nut is tightened onto the thread.

3.4 – Flushing of the Ceramic Disk

Two ways are known to flush the ceramic disk, which is currently a 500 kPa (5 bar) air entry ceramic. The first way tried was flushing the ceramic from below using the back-pressure tank. Due to the disk being glued to the triaxial pedestal, there is a risk that high applied water pressure would break the glue bond. Therefore, only pressures less than 50 kPa should be used for this method. The time required to flush the ceramic in this manner is 2-3 days. Through experimentation, it was decided that this is the most effective way to saturate the ceramic disk.

The second way to flush the ceramic is described below. A significant volume of water is required to fill the lines and valves in between the back-pressure tank and the ceramic disk. This void will have to be filled before any flushed water can be collected. For this reason, a back-pressure of 50 kPa is applied to fill this void. Once it is filled, the center front and rear right water valves are closed to hold the water inside. The back-pressure line is disconnected from the t-connector, and the following procedure is practiced.

The second way to flush the ceramic is to install the triaxial cell over the ceramic disk and apply a cell pressure that will saturate the disk from above. The cell is filled with de-aired water, as shown in Figure 3.5. It is imperative that de-aired water is used for this step. Tap water and de-ionized water contain dissolved air, which will desaturate the ceramic disk. The center front valve and the rear right valve (the one currently connected to the water pressure sensor) are opened. This will allow water to flow out of the triaxial cell. It is ensured that the hoses extending from each valve are connected with a t-connector, and another line extends from the t-connector to the collection device, as shown

in Figure 3.6. It is highly recommended that a graduated cylinder be used to collect the flushed water. This device will allow one to easily measure the quantity of flushed water. A piece of aluminum foil is placed over this graduated cylinder, enclosing the end of the drain line to limit the amount of evaporation. Once the hoses have been assembled, a 500 kPa cell pressure is applied.

For the first method, the ceramic disk is saturated once steady-state flow conditions have been established and no air bubbles exist on the surface of the ceramic. A measurement of the saturation of the ceramic disk by the first method was made from a nearly dry state to saturation. Figures 3.7, 3.8, 3.9, and 3.10 describe the flow characteristics of the de-aired water before a steady-state condition is achieved. Figure 3.7 shows the cumulative volume of water passed through the ceramic, while Figure 3.8 gives the flow rate through the ceramic with time. Figure 3.9 describes the change in flow rate before full saturation of the ceramic. Figure 3.10 shows the flow velocity of the de-aired water with time. The steady-state flow was established after 30 hours of flushing with 50 kPa of back pressure. Measurements of flushed water should be read from the volume of the back pressure tank (back volume). When no air bubbles were observed for 12 hours after steady-state conditions were achieved, the ceramic disk was considered saturated.

For the second method, no consistent criteria have been established for saturation. During one test, 6 liters of water were flushed through the ceramic without achieving saturation. It is believed that the high pressure applied during this procedure desaturates the ceramic disk and is counter-productive. This is based on the observation that the flow rate of water flushing through the ceramic disk decreases with time and eventually stops

after approximately 48 hours. For these reasons, this method is not recommended. Further study will need to be done before saturation criteria can be established for this method.

3.5 – Preparation of the Remolded Soil Specimen

A non-plastic silty-sand (SM) was tested. Since this soil has no cohesion, samples have to be created in a rigid mold. Due to the small grain size and corresponding low intrinsic permeability, the soil was very difficult to saturate.

To begin, the soil was placed in a steel pan and pulverized to remove any conglomerates. The soil was then placed in the drying oven for 24 hours with an aluminum foil label. A paper label cannot be used as this will combust in the oven and affect the soil properties. The sample is removed from the oven the day before creating the test specimen and is allowed to cool to room temperature. It is imperative that the soil reaches room temperature before the addition of water because the water could evaporate if placed on hot soil. Based on the desired gravimetric water content, the mass of water needed to achieve this water content is calculated. The weight of the fluid is measured in a plastic container after zeroing the scale for the mass of the container. The water is poured onto the dry soil. The water container is shaken to ensure as much of the water enters the soil as possible. While wearing a latex glove, the soil is mixed by hand in the pan until the color of the soil is uniform. The soil pan is encapsulated with food wrap, and the edges taped shut. The soil is allowed to sit for 24 hours to ensure full mixing. Figure 3.11 shows the de-ionized water after placement onto the soil before hand mixing. Figure 3.12 shows the thoroughly mixed soil, and Figure 3.13 shows the fully sealed soil mixing pan.

Once the soil is mixed, the triaxial cell is opened to allow for the construction of the soil sample. The water is drained out of the cell into the sink via a drainage hose. All

hoses except the hose connected to the water pressure sensor are disconnected from the cell, as shown in Figure 3.14. The piston is disconnected from the driving motor by using a hex-drive wrench to release the screw support, and the connection is then unscrewed. The cell is slid forward then each sealing rod is loosened. Two individuals lift the cell and lay it on its side between two pieces of angle iron on the counter. The inside of the cell, the piston head, the pedestal, and the cell floor must be thoroughly cleaned. Do not wipe the water off the ceramic disk, as this may desaturate the disk.

Vacuum grease ensures a good seal of the equipment and reduces errors. Vacuum grease is applied to the piston head, top cap, piston cup, and the sides of the pedestal. Vacuum grease is not applied to the bottom of the top cap or the ceramic disk. This will cause clogging and inaccurate results. Figures 3.15, 3.16, and 3.17 show the properly lubricated top cap and suction cap, triaxial piston head, and ceramic disk pedestal, respectively.

Filter papers are needed to ensure the soil particles do not flow out of the specimen cylinder. The specimens tested in both the M-series and Z-series were each 2 inches in diameter, and only 2.5-inch diameter filters are available. Therefore, the filters had to be trimmed to a 2-inch diameter. Figures 3.18 show how the top cap was used to measure the 2-inch diameter filter papers required for the specimen. Figure 3.19 shows the marked filter papers before trimming. The filters were soaked in deionized water for saturation. A filter was placed on the ceramic disk as shown in Figure 3.20. After inspecting a latex membrane for holes and other defects, the membrane was installed within the mold as shown in Figure 3.21. The O-ring is to ensure the membrane does not move during compaction. The mold and membrane are installed into the cell as shown in Figure 3.22.

Similar to the way embankments are constructed, soil lifts are required to build the specimen. The weight of the moist soil in each of the 10 lifts was calculated using Table 3.2. Once the mass of each layer was determined, the soil was weighed out, as shown in Figure 3.23. The tools required for compaction are assembled as shown in Figure 3.24.

Two people working in sync are needed for the compaction. The height of the mold lip to the ceramic disk was measured. The specimens tested were 100 mm tall. Ten lifts in total were placed in the mold, each 10 mm thick. One individual poured the soil into the funnel while another person struck the funnel lip with the scratching tool. The funnel is required to achieve the energy level needed to compact the soil to the desired density. The soil is compacted with the hammer until the desired thickness is achieved. The soil surface was thoroughly scratched before adding the next lift. This promotes homogeneity in the specimen and reduces error. To reduce the chance of a spill, the last two lifts were added in portions, compacted, and scratched until all required soil was added.

Once the specimen was completed, soaked filter paper and porous stone were added to the top of the specimen. The mold was removed, and the top cap was placed on the specimen. Five O-rings were added to the top and bottom of the specimen to prevent leaks. Following this, the piston cup was added to the top cap, as shown in Figure 3.25. The top cap and drainage valve were connected via the hose. All connections were tightened, and the triaxial cell was reinstalled, as shown in Figure 3.26.

The star pattern must be followed while screwing down the tightening rods. The triaxial cell was seated onto the leveling pedestal, and the piston was lifted by hand to its highest position. The upper piston was lowered with the computer by specifying a displacement in the software. The lower and upper piston rods were connected by screwing

the connector onto the upper piston. The security ring was raised to the bottom of the connector and was tightened with a hex-drive wrench.

A few times during the test series, the threads at the connection between the upper and lower piston segments did not line up. This is a common problem and has no definite solution. If the threads are not connected properly, the test cannot be conducted. A trial and error method was developed to solve this issue which involved rotating the piston and seeing if the threads lined up. If this did not work, the driving motor was slightly rotated by adjusting the load frame. It was easy to loosen and tighten the leveling nuts with a C-clamp. When the threads lined up, and the piston rods were connected, and the load frame was checked for levelness. The bar level was placed on the top of the load frame to do this.

3.6 – Specimen Flushing

If the sample is not flushed sufficiently, it will be impossible to reach the desired B-value in the following saturation phase. Therefore, it is necessary to pass at least one specimen volume of desired water through the specimen before moving to the saturation phase. Effective stress of 30 kPa is needed to ensure the sample does not fail prematurely. To generate this value, the cell pressure was set at 60 kPa and the back pressure at 30 kPa.

Flushing was completed by applying back pressure to the sample from the bottom and surrounding cell pressure. Through trial and error, this method was deemed the most effective at flushing the sample. The back pressure tank was filled with de-aired water and then connected to the front center valve of the triaxial cell. The void beneath the ceramic disk must be filled with water at all times during the test phases to maintain saturation of the ceramic disk. Therefore, the front center valve was kept closed until the back pressure was applied. The front center valve was opened, and the water was allowed to enter the

cell. The back pressure and cell pressure were maintained at the target values until 2 specimen volumes of de-aired water were collected in the drainage graduated cylinder.

In an attempt to increase the rate of flushing, a vacuum was applied to the top of the specimen through the use of a vacuum pump. While this method slightly increased the flow rate of water out of the specimen, it proved to be counter-productive because this method desaturated the specimen, exactly the opposite of the objective. After several attempts with the vacuum method, it was decided to flush the specimen with back pressure only.

3.7 – Specimen Saturation

Due to the nature of porous media, full saturation (S = 100%) is not achievable. There will always be a small air volume in the soil, no matter how long the water flows through. This is why a Skempton B-value equal to one is not possible. Ideally, one can achieve B = 0.95 after extended flushing. For this test, B = 0.90 was considered to be sufficient. By definition, the B-value is the ratio of the increase in pore water pressure in the soil over the increase in cell pressure as described in Equation 3-1 (Skempton, 1954).

$$B = \frac{\Delta uw}{\Delta cell\ pressure} \tag{3-1}$$

A series of saturation-ramp and B-check value phases were conducted until B = 0.90 was achieved. Each saturation test stage must be created individually and added to a list. This was done by first calculating the target cell pressure and back pressure. A difference of 30 kPa was used during all tests to maintain effective stress of 30 kPa, as shown in Equation 3-2. The cell pressure must always be higher than the back pressure to generate effective stress. For each saturation ramp, an increase in pressures of 100 kPa was used except when the cell pressure exceeded 500 kPa. In these cases, pressure increases of

50 kPa were utilized. The maximum cell pressure capacity of the triaxial cell was 800 kPa. With this limitation in mind, the consolidation and test cell pressures had to be kept below 800 kPa.

$$Cell\ pressure - back\ pressure = 30\ kPa \tag{3-2}$$

Once the desired pressures were calculated, the GDS software was activated, and "Choose Data File" was selected. The options "Single Directory" and "Next" were selected as shown in Figure 3.27. A folder was created, and the file was saved within it. The sample parameters given by the software were accepted, and "Add Test" was selected. The option "GDS_ttSatcon" was chosen, and "Create New Test Stage" was clicked. For the saturation test, "Saturation Ramp" was selected as the test type. The target pressures were entered as shown in Figure 3.28. A pressure increase of 1 kPa per minute was used to determine the time needed to reach the target pressures. The option "Next" was chosen, and the dialog box was filled out, as shown in Figure 3.29. The button "Next" was selected, and the "Undock specimen" box was left unchecked. The option "Add to Test List" was chosen, and the inputs were rechecked to ensure they were correct. The button "Go to Test" was selected, and "Start Test" was clicked.

During the test, a plot including time vs. cell pressure vs. back pressure was generated. Once the pressures stabilized at the target values, the next saturation test or B-check began. Through experience, it was found that at least 2 saturation ramps should be done before the first B-check. If this is not followed, a negative B-value will occur, which is not accurate.

For the B-check test, a new test was created with a cell pressure 25 kPa higher than the current cell pressure. The option "Create New Test Stage" was chosen, and "B-check"

was selected for the test type. The desired cell pressure was entered, and the "Next" button was clicked. The target cell pressure is entered as shown in Figure 3.30. The option "Next" was selected, and the "Undock specimen" box was left unchecked. The command "Add to Test List" was chosen, and the inputs were rechecked to ensure they were correct. The option "Go to Test" was selected, and "Start Test" was chosen.

A plot of the B-value vs. time was generated to see the change in the B-value. More than one B-check phase was required for each specimen with an average of 5 B-check tests in order to achieve B = 0.90. The B-value during the saturation phases was ignored as it is not accurate. To achieve a B-value closer to the target, each saturation phase was allowed to continue for 24 hours before the B-check was conducted. This step allowed for much higher B-values to be measured compared to the B-check measured directly after the target saturation back pressure and cell pressure were achieved.

3.8 – Consolidation

Unlike traditional triaxial tests, the unsaturated cyclic test involves both pore water (u_w) and pore air (u_a) pressures. This requires the calculation of target u_a, u_w, and cell pressure to achieve the net normal stress and matric suction described in Equations 3-3 and 3-4. The cyclic stress ratio (CSR) relates the deviator stress to the net normal stress and is found using Equation 3-5. In general, the higher the CSR and lower the matric suction, the smaller number of cycles are required to fail the specimen.

$$Net\ normal\ stress = \sigma_{net} = radial\ stress - u_a \tag{3-3}$$

$$Matric\ suction = \psi = ua - uw \tag{3-4}$$

$$Cyclic\ stress\ ratio = CSR = \frac{\Delta\sigma}{2\times\sigma net} \tag{3-5}$$

Before beginning the consolidation of the sample, the air tank was completely emptied. The air line was disconnected from the triaxial cell and was allowed to vent to the atmosphere, as shown in Figure 3.31. A very large negative pore air volume was specified to empty the air tank, as shown in Figure 3.32. This ensures all moisture that may accumulate in the tank was expelled before consolidation. The air tank was filled using air from the atmosphere by specifying a pore air volume of 900,000 mm^3.

Once the air tank and the back pressure tank were filled, a very small load cell (axial force value) was applied to ensure the specimen was docked. A load cell value of 0.001 kN was used in all tests. Two specimens were lost to necking because this step was not followed.

Following this, a consolidation stage was created, as shown in Figure 3.33. The pre-determined u_w, u_a, radial stress (cell pressure), and axial stress were input into the computer in the dialog box shown in Figure 3.33. To ensure the piston remains in contact with the specimen during consolidation, the axial stress must be 5 kPa greater than the radial stress. Also, a minimum displacement of -2 mm was input to prevent the specimen from failing due to extension during the consolidation phase. At least 2 specimens were lost due to this step not being followed.

The volume of air in the hoses was calculated in a spreadsheet. It is unclear how important this value is, and all values in Figure 3.34 are estimated. The rate at which the pressures increase to their target values can be specified, as shown in Figure 3.33. A researcher must be present to manually open the air valve when u_a and u_w equalize. Once all parameters were input, the test input box was closed and re-opened. All parameters were rechecked. It was crucial that the air valve shown in Figure 3.35 was closed until the pore

air pressure became greater than the pore water pressure. If this valve was opened before this point, the specimen would have a sudden drop in internal pressure and would collapse. One specimen was lost during the Z-series due to this error. The back pressure valve and the front center valve were left open during the consolidation phase to allow the pore water to either flow in or out to achieve equilibrium.

The options “Go to Test” and “Next Stage” were chosen. The axial stress, pore water pressure, and radial stress all increased at rates much higher than the pore air pressure. This is a limitation of the equipment and cannot be avoided. Once the equilibrium pressures were reached, the back volume vs. time plot was observed and the rate of water entering or leaving the specimen was observed. Once the flow rate of water in or out of the specimen approached zero, it was considered the end of primary consolidation. For the specimens tested in both the M-series and Z-series, primary consolidation ended within 48 hours. Figure 3.36 depicts the back volume change vs. time for test specimen Z5.

3.9 – Cyclic Triaxial Test

Due to the inability of the desktop GDS software to measure the pore air pressure during the cyclic triaxial test, a laptop utilizing the software “LabView” was used in conjunction with an external pore air pressure sensor to measure the change in pressure during the test. The air pressure sensor was powered by a DC power source, as shown in Figure 3.37. The sensor measured the air pressure most accurately when the power source provided exactly 24.0 volts. This value had to be manually controlled via the voltage adjustment knob. The pore air pressure was first measured as a voltage by the sensor and was transmitted to the laptop via a chassis device which recorded the change in voltage throughout the test. The connection between the chassis and the laptop is shown in Figure

3.38. A spreadsheet was developed to convert the measured potential difference from volts (V) to pressure (kPa). Before the test was conducted, the air pressure recorded by the sensor was checked against the pore air pressure being measured by the desktop software. If the two systems matched, then the triaxial test was conducted. For ease of later data analysis, it was imperative that the desktop and laptop recorded all pressure magnitudes at the same time rate. A sampling rate of 5 times per second or 5 Hz was selected for both systems.

For the undrained, unsaturated cyclic triaxial tests, the front center valve on the triaxial base was kept closed to prevent the escape of pore water through the ceramic disk. For the drained test Z3, this valve was kept open to prevent the buildup of pore water pressure. Even though the undrained tests prevented the escape of pore water and pore air, the front right drainage valve was kept open to allow for the pore air pressure to be recorded by the air pressure sensor. Since the air valve shown in Figure 3.35 was kept closed, the total triaxial system was considered undrained.

Once the laptop recording software was prepared, the triaxial test sequence was prepared in the desktop GDS software. To begin, the test type “GDS_tt4UNSAT” was selected, as shown in Figure 3.39. Next, the frequency, amplitude, and stiffness estimates are input into the dialog box shown in Figure 3.40. The stiffness estimate is a unitless value used by the triaxial test device to determine how much axial movement is required to generate the desired amplitude of axial force in the cyclic test. After trial and error, it was decided that stiffness of 2.5 was best suited to the specimens tested in both the M-series and Z-series. An accurate stiffness estimate will show a sinusoidal relation between test time and axial force. In the next dialog box, shown in Figure 3.41, the maximum number of cycles for the test was inserted. The maximum number of cycles was set at 220 cycles

because the specimen would be considered “non-failed” if the specimen reached 200 cycles without developing a double-amplitude axial strain of 5%. The additional 20 cycles were conducted to observe the residual strength of the specimen. A frequency of 0.05 Hz was utilized for all tests, as suggested by Tsukamoto et al. (2014). This frequency is high enough to replicate an earthquake vibration and low enough to allow for uniform pore pressure distribution within the specimen (Tsukamoto et al., 2014).

After a final check of the valves and water and air pressure recording systems, the unsaturated cyclic triaxial test was conducted. First, a timer was started to record the elapsed time of the test. Second, the LabView software was activated on the laptop, and the time relative to the timer was recorded. The time measurements during the test needed to be as accurate as possible to avoid errors caused by offset data. During this study, all-time measurements conducted with a timer were measured to the nearest second. Third, the triaxial test was started by selecting “Start Test” in the GDS desktop software. As with the laptop software, the elapsed time was recorded accurately. The test was observed closely for its duration to ensure the proper function of the triaxial equipment. If the tested specimen failed before reaching 220 cycles, the GDS software stopped the test immediately upon reaching high axial strain to avoid damaging the triaxial equipment. Fourth, the elapsed time corresponding to the end of the cyclic test was recorded. Fifth, the LabView software was stopped manually and the time elapsed time was recorded. Section 3.10 describes how the triaxial equipment was carefully disassembled, and the specimen gravimetric water content was measured.

3.10 – Sample Recovery and Equipment Deconstruction

Once all data files had been saved, the disassembly of the triaxial cell began. The air pressure sensor and air hoses were removed from the triaxial base. The tap water used as the confining fluid for the test was drained through the left front drainage valve through the use of a hose. Once the water had been drained, a cell pressure of 300 kPa was applied to the top of the specimen using the GDS desktop software to break the bond between the triaxial piston and the specimen suction cap. This was done to allow for the removal of the triaxial cell without a tensile failure of the specimen when the triaxial piston was moved upward. The cell pressure was applied by connecting the cell pressure hose to the rear hose port on the top of the triaxial cell. A series of short hoses and nuts were assembled in order to attach the cell pressure hose to the rear hose port. If the cell pressure of 300 kPa was insufficient to break the vacuum grease bond on the piston, higher cell pressure values were used until the bond broke. The bond always broke before a cell pressure of 500 kPa was reached.

A hex-drive wrench was used to disconnect the upper and lower piston rod segments, as shown in Figure 3.26. Once this connection was disconnected, a researcher had to continuously hold the lower piston rod segment to prevent the piston from rebonding with the specimen suction cap. If this occurred, the triaxial cell would have to be reassembled, and a cell pressure reapplied to break the bond. After disconnecting the piston rod segments, the triaxial cell was lifted off of the base plate and slid out from under the load frame. While continuing to hold the lower piston rod segment, the tightening rods were loosened, and the triaxial cell was removed. The soil specimen was then placed in a steel pan, and the membrane was cut open lengthwise using a knife. A portion of soil from the top, middle, and bottom of the specimen were collected in small steel cans. The wet

mass of the three portions was weighed on the scale shown in Figure 3.23. These portions were placed in a drying oven, and the dry mass was measured after 24 hours of oven time. The gravimetric water content of the specimen was determined by averaging the gravimetric water content of the three portions. This value was then used to calculate the degree of saturation in a spreadsheet shown in Table 3.1.

3.11 – Data Recovery and Analysis

The key challenge to the data analysis was to ensure the proper time alignment between the desktop collected data and the laptop collected data. Since the air pressure was recorded for a period of time before the test began, the point at which the test began had to be identified from the pore air pressure data. Once this was completed, the pore air pressure data was merged with the test data collected by the desktop GDS software. After the pore air pressure data was merged, the net normal stress and matric suction values were calculated using a spreadsheet. Plots of the desired test results were generated using "Igor Pro" software. All plots generated during the study are shown in Chapter 4 of this document.

Table 3.1 – Degree of Saturation Calculation Spreadsheet

	As-Compacted Condition	After Consolidation Condition	Units
Total unit weight	1.82	1.86	g/cm^3
Dry unit weight	1.53	1.55	g/cm^3
e	0.76	0.74	dec.
S	67.5	**71.6**	%
Wet soil weight	363.95	365.89	g
Axial displacement	-	0.46	cm
Lateral displacement	-	0.23	cm
Poisson's ratio	-	0.50	dec.
Height	9.50	9.04	cm
Diameter	5.04	5.27	cm
GWC	0.16	0.20	dec.
Section area	19.95	21.83	cm^2

Table 3.2 – Weight per Lift Calculation

Volume (cm3)	199.50
Intial Wet Unit Weight (g/cm3)	1.82
Weight (g)	363.95
No. of Layer	10
Weight per layer (g)	36.39

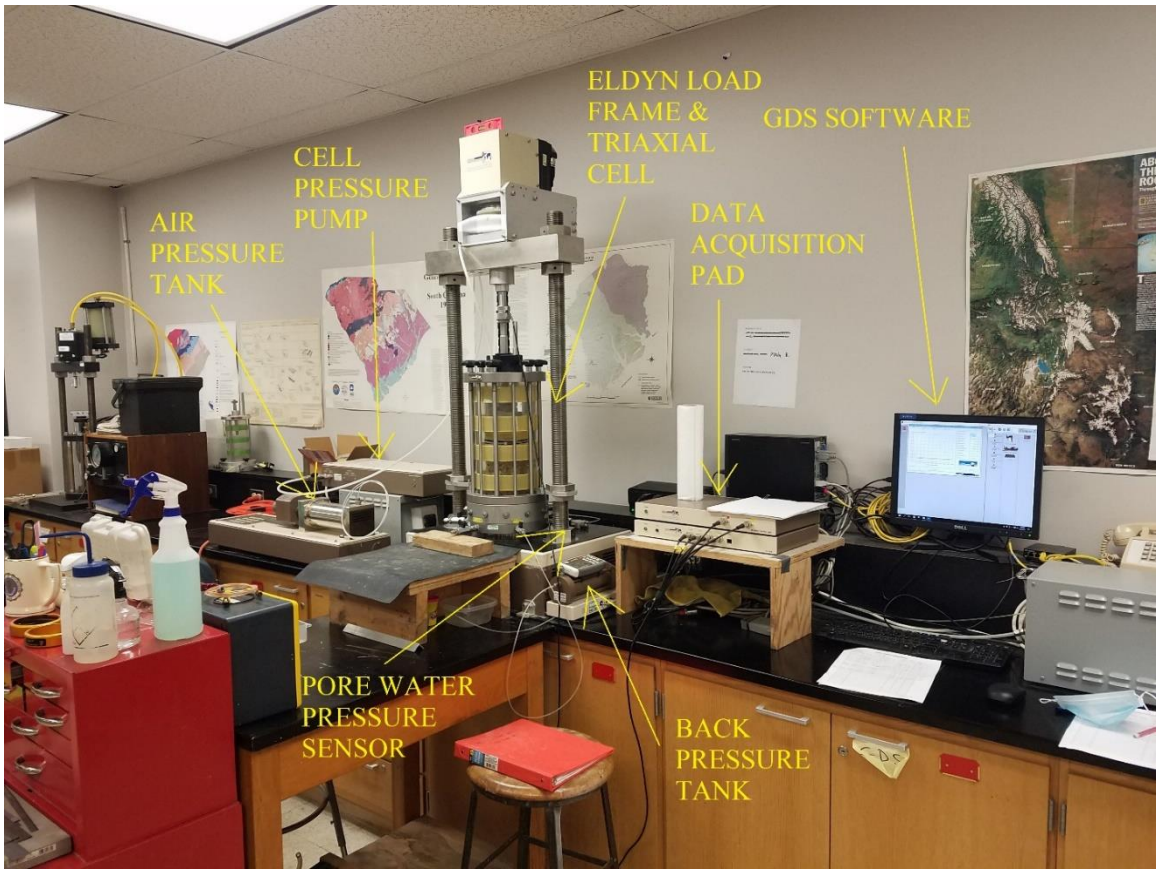

Figure 3.1 – Total ELDYN Triaxial Setup

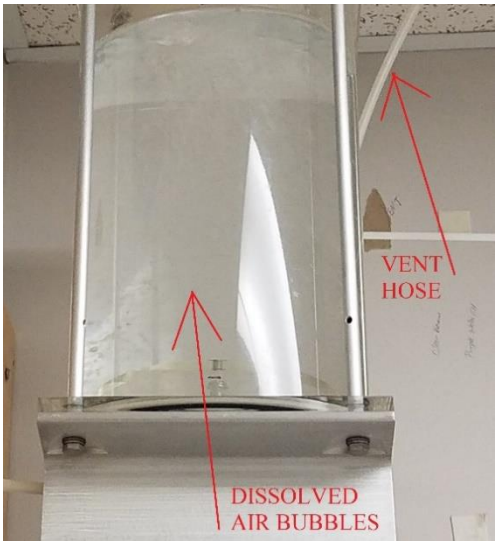

Figure 3.2 – Dissolved Water Process

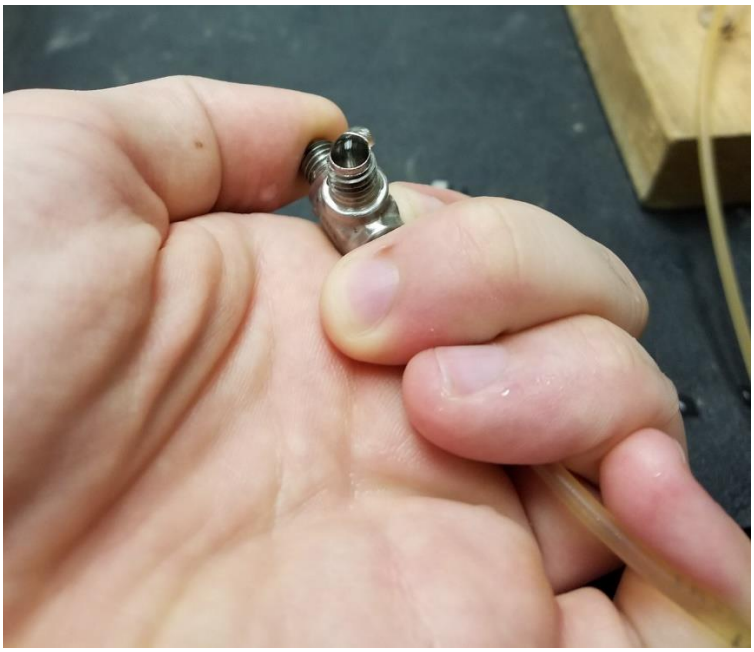

Figure 3.3 – Removal of air bubbles from the t-connector

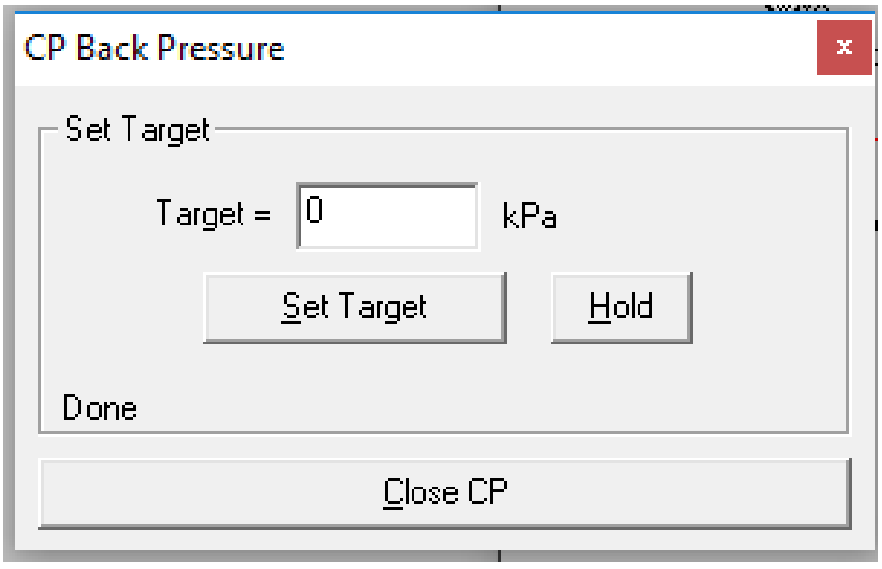

Figure 3.4 – Back Pressure Adjustment

Figure 3.5 – Triaxial Cell Filling Process

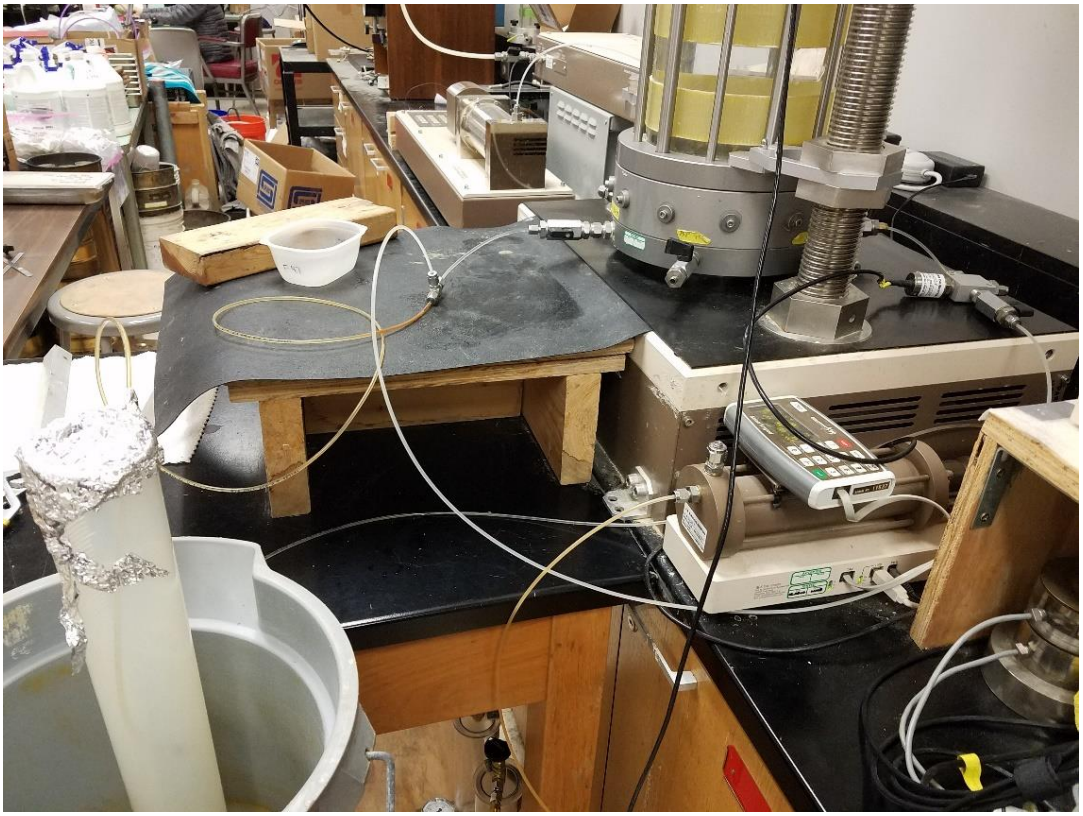

Figure 3.6 – High pressure ceramic disk flushing

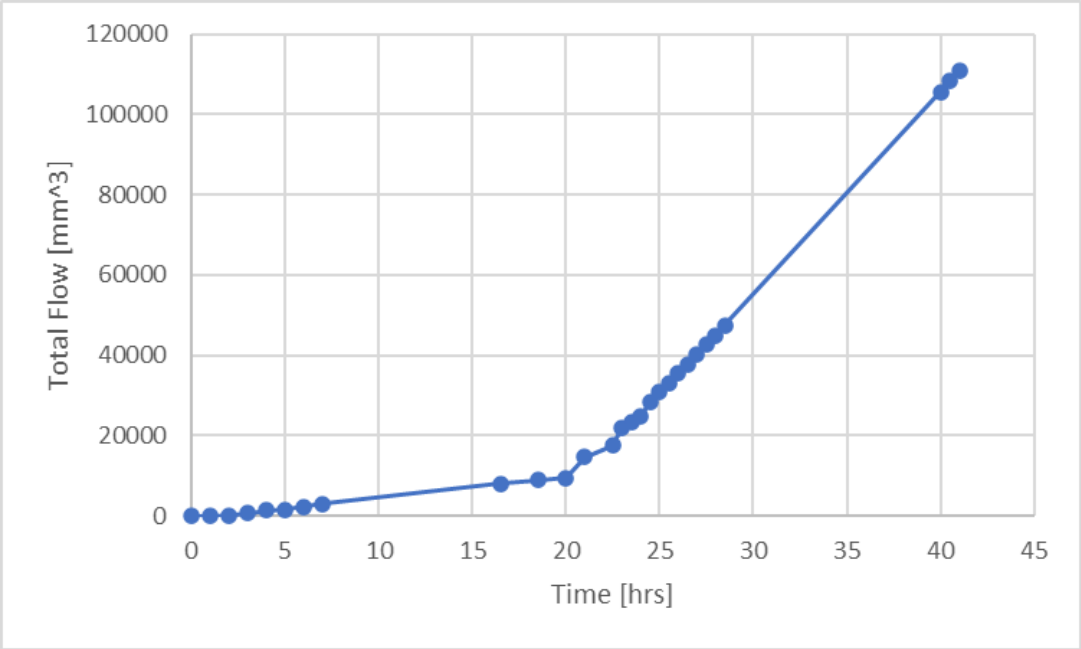

Figure 3.7 – Volume of de-aired water passed through ceramic disk

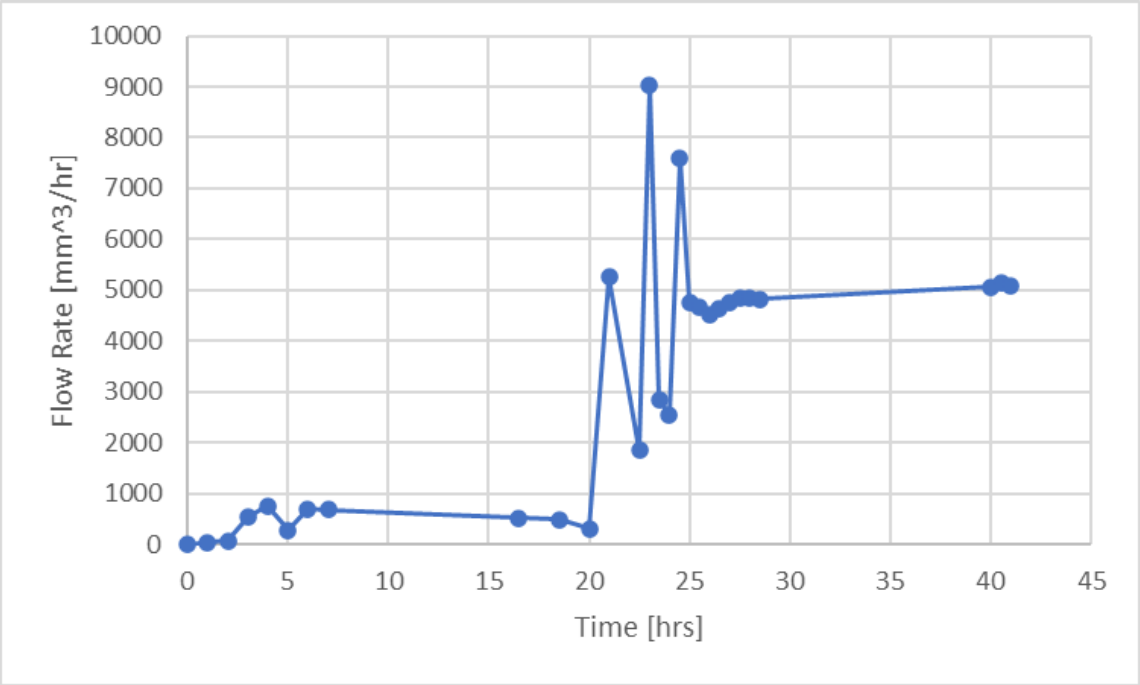

Figure 3.8 – Flow rate of de-aired water through ceramic disk at different times

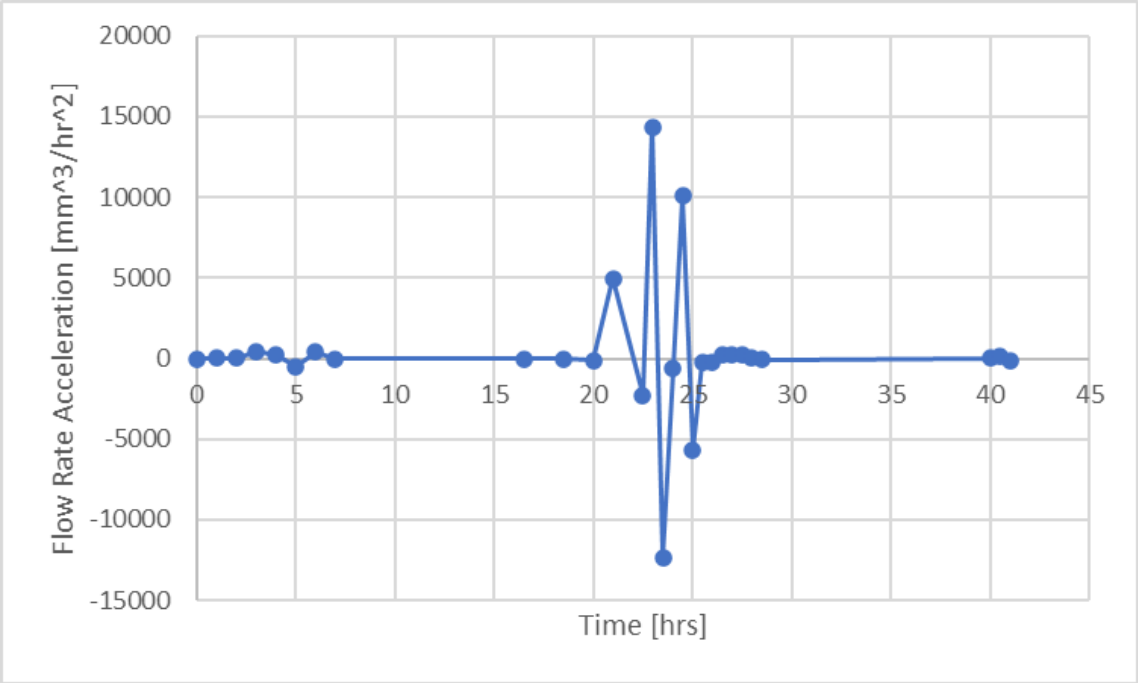

Figure 3.9 – Flow rate acceleration of de-aired water through ceramic disk

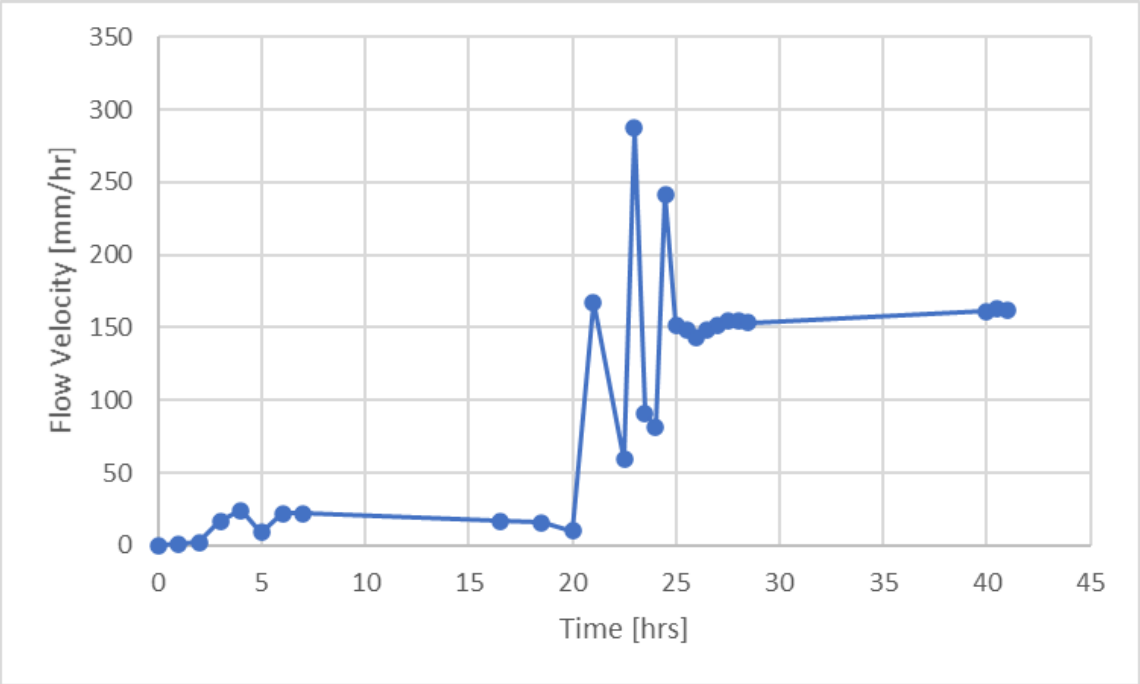

Figure 3.10 – Flow velocity of de-aired water through ceramic disk

Figure 3.11 – Water added to soil before mixing

Figure 3.12 – Soil and water after hand-mixing

Figure 3.13 – Sealed soil mixing pan

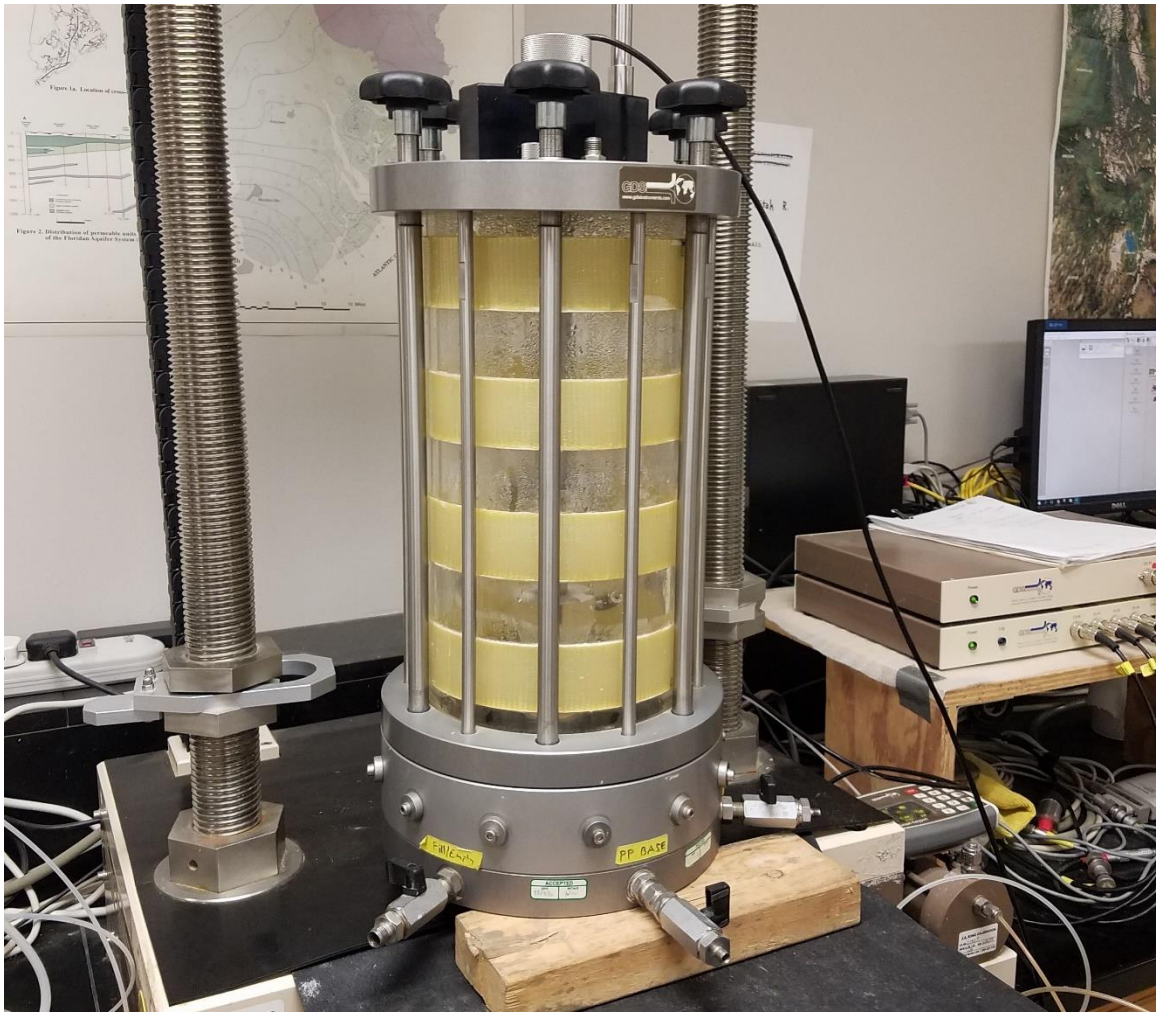

Figure 3.14 – Triaxial cell used in the study

Figure 3.15 – Lubricated top cap and suction cap

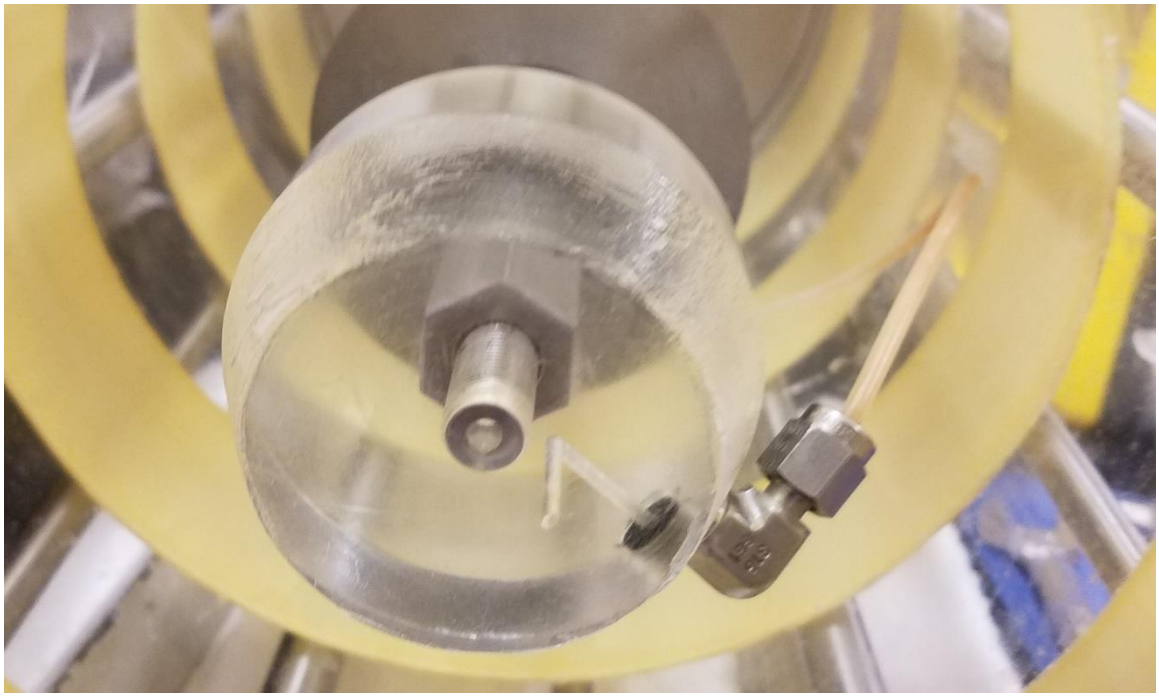

Figure 3.16 – Lubricated triaxial piston head

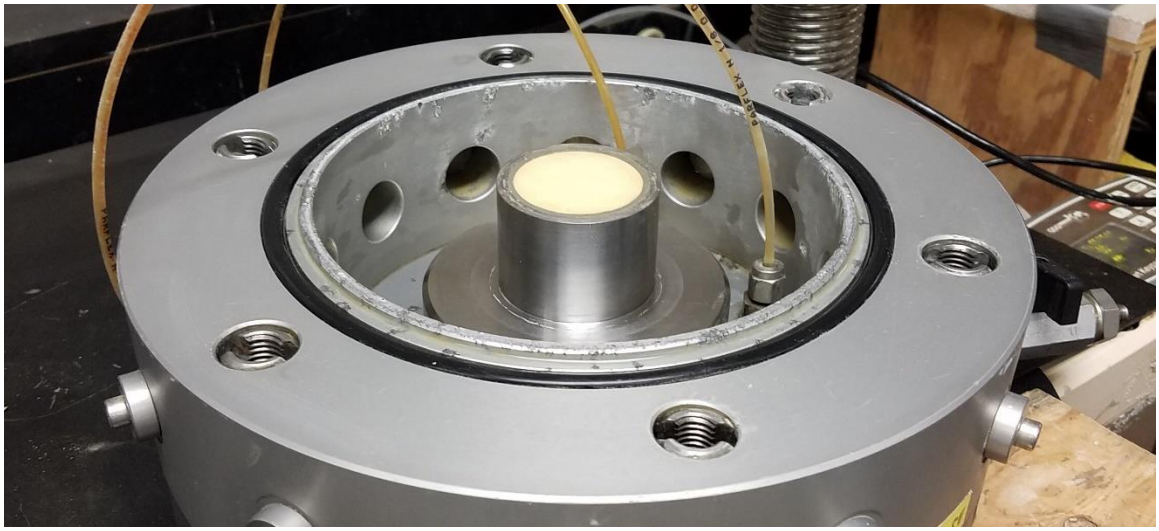

Figure 3.17 – Lubricated ceramic disk pedestal

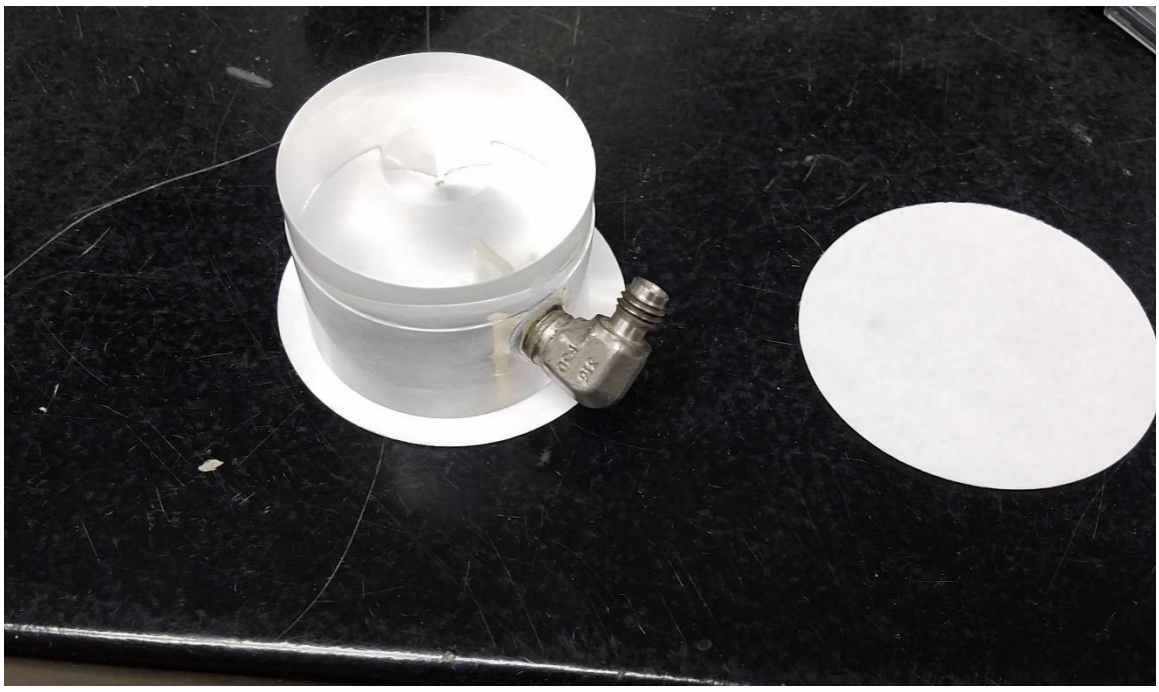

Figure 3.18 – Filter paper adjustment measurement

Figure 3.19 – Measured filter papers before trimming

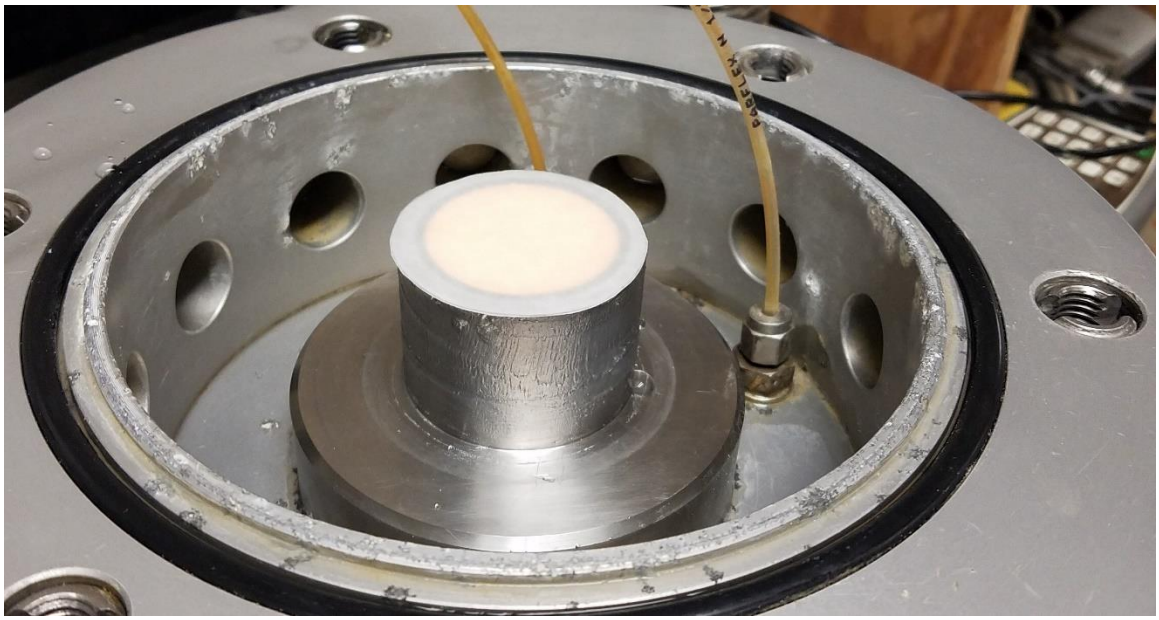

Figure 3.20 – Filter paper installed on ceramic disk

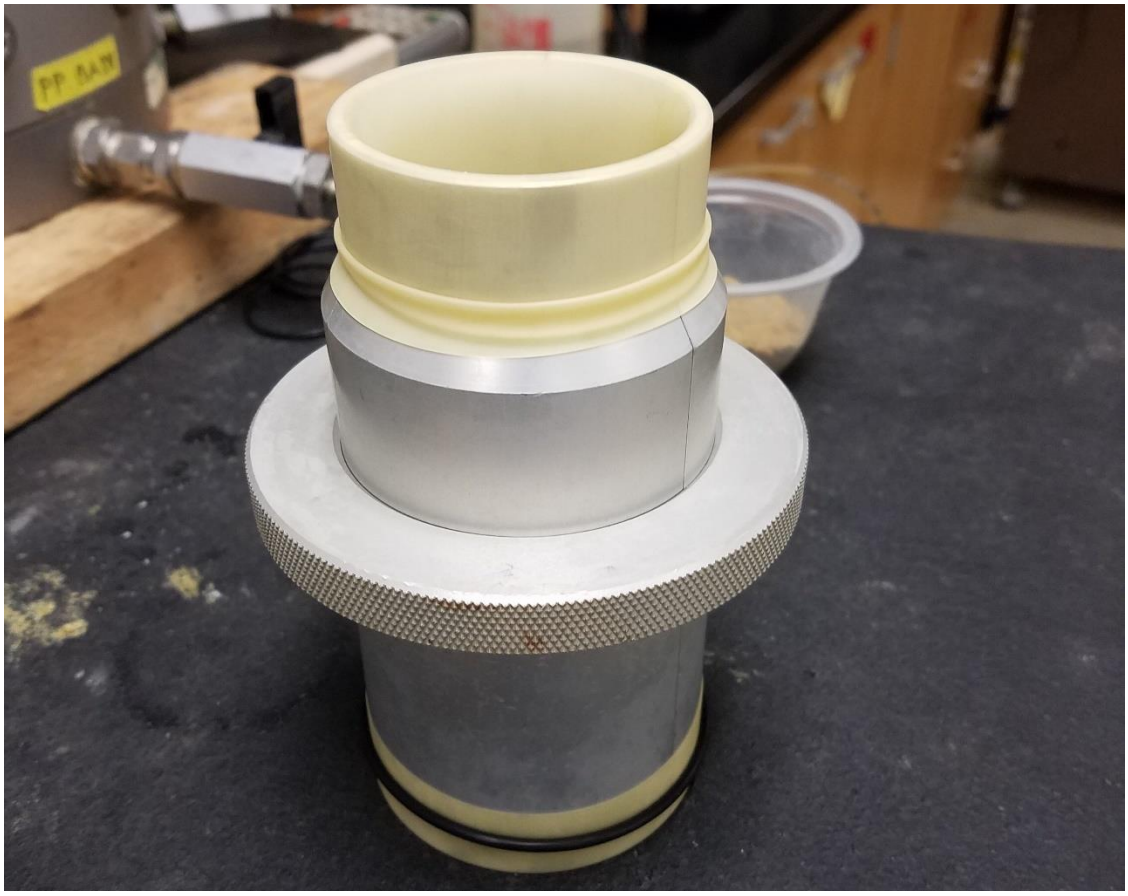

Figure 3.21 – Membrane installed in compaction mold

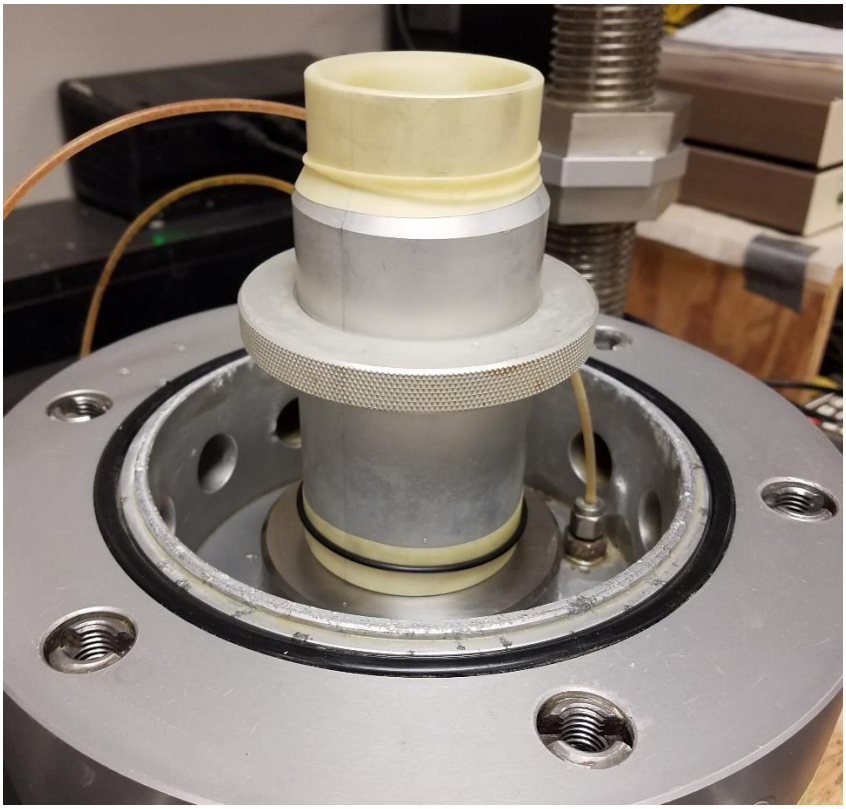

Figure 3.22 – Compaction mold installed in triaxial base

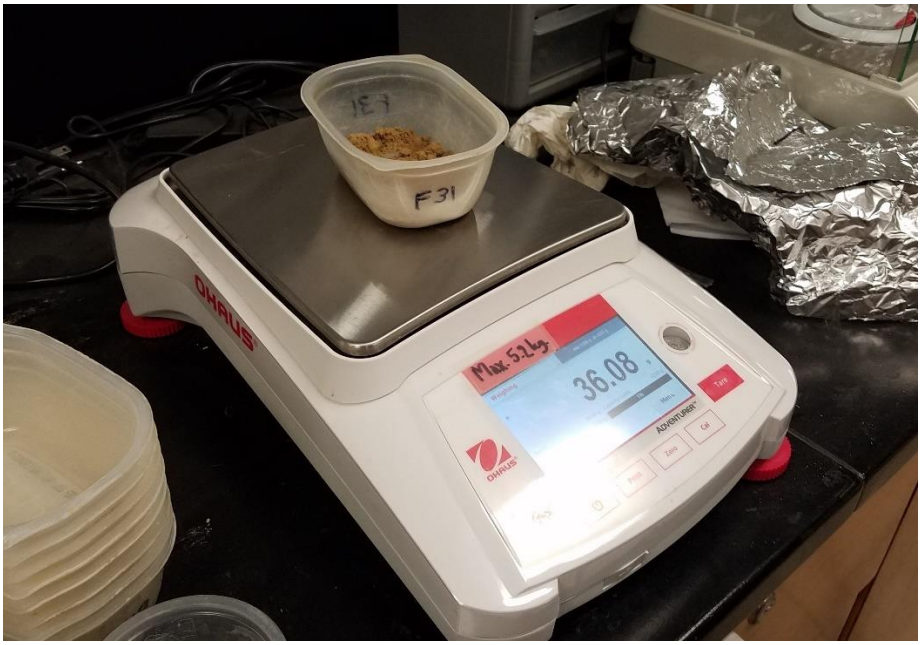

Figure 3.23 – Mass measurement of one lift of soil

Figure 3.24 – Compaction tools

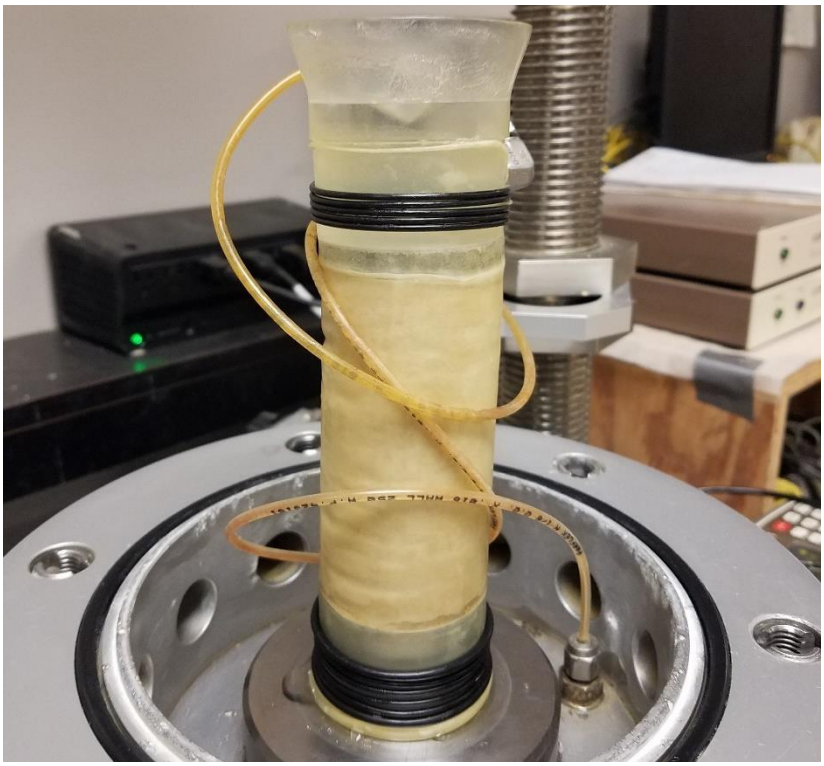

Figure 3.25 – Completed specimen used for Z-series test

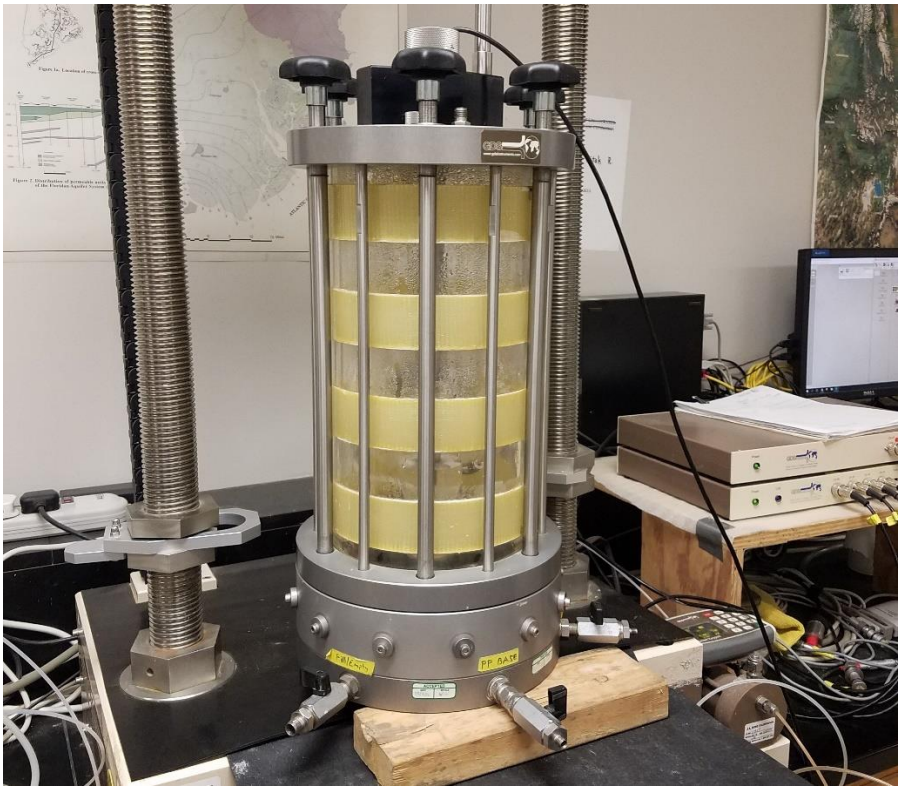

Figure 3.26 – Reassembled triaxial cell with specimen

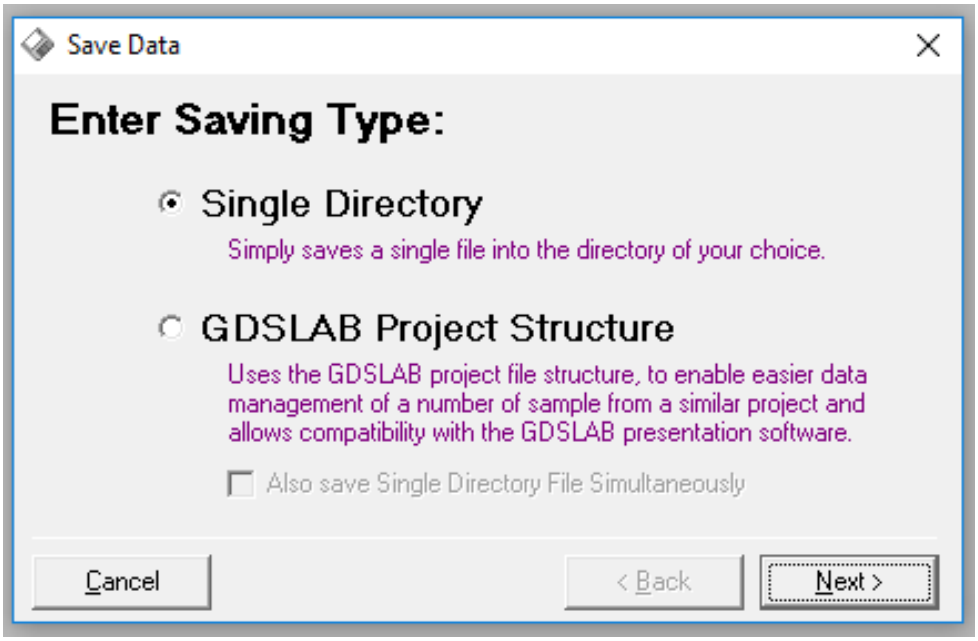

Figure 3.27 – Dialog box for data saving format

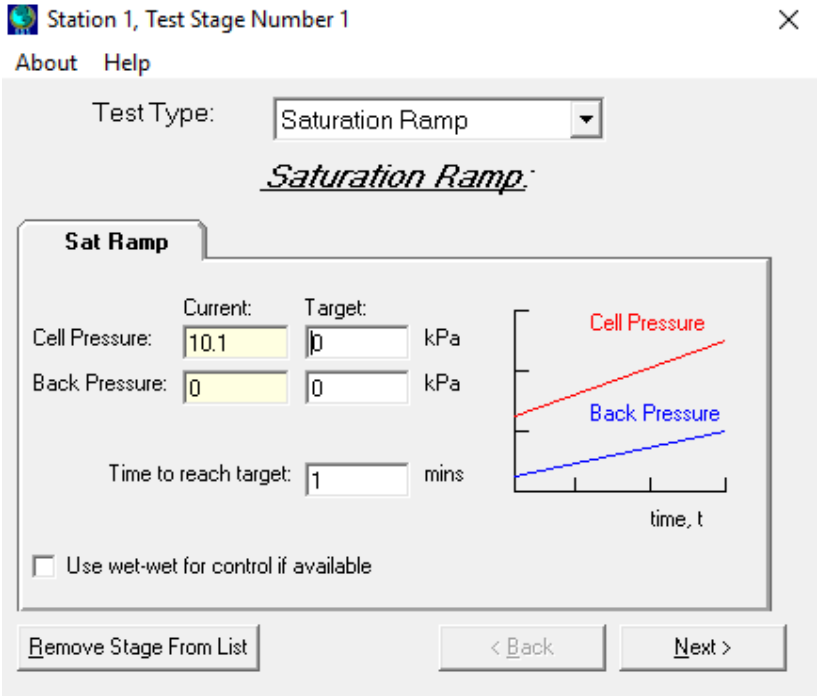

Figure 3.28 – Saturation test dialog box

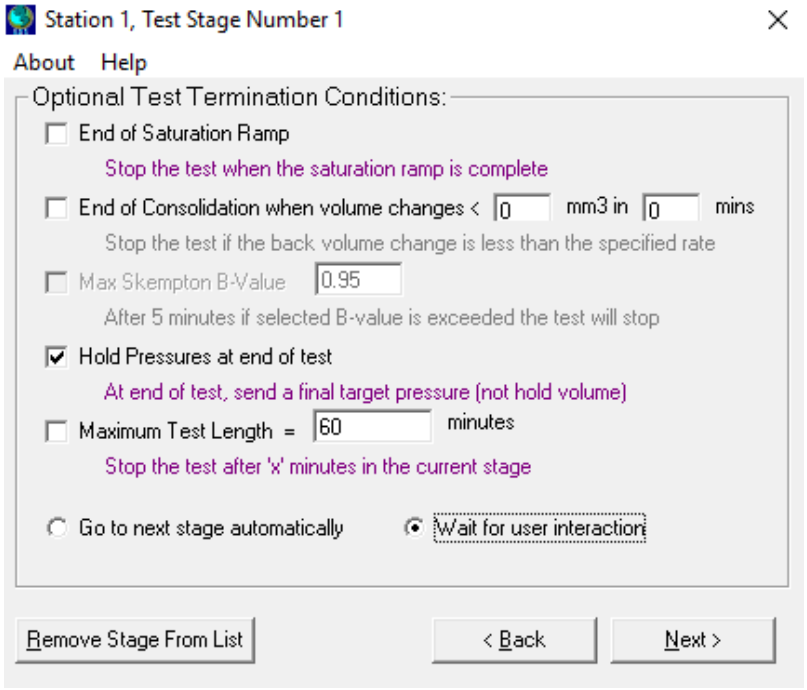

Figure 3.29 – Test termination criteria for saturation ramp

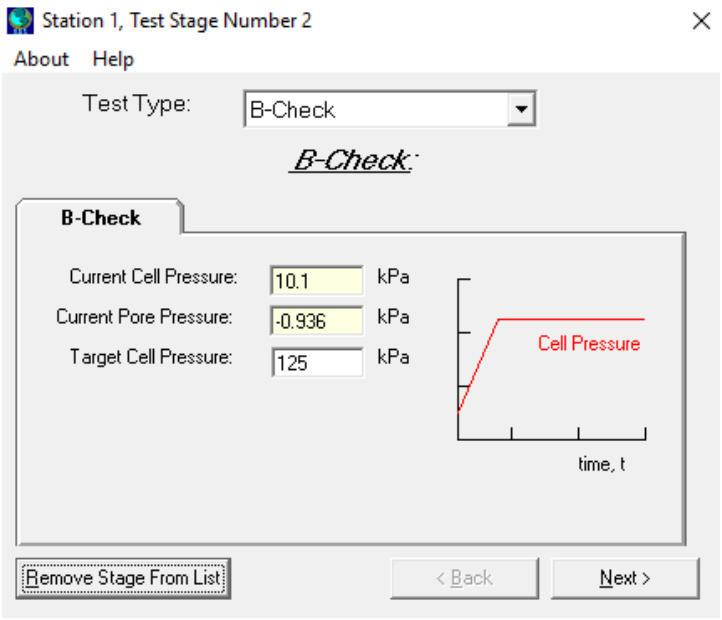

Figure 3.30 – B-check dialog box

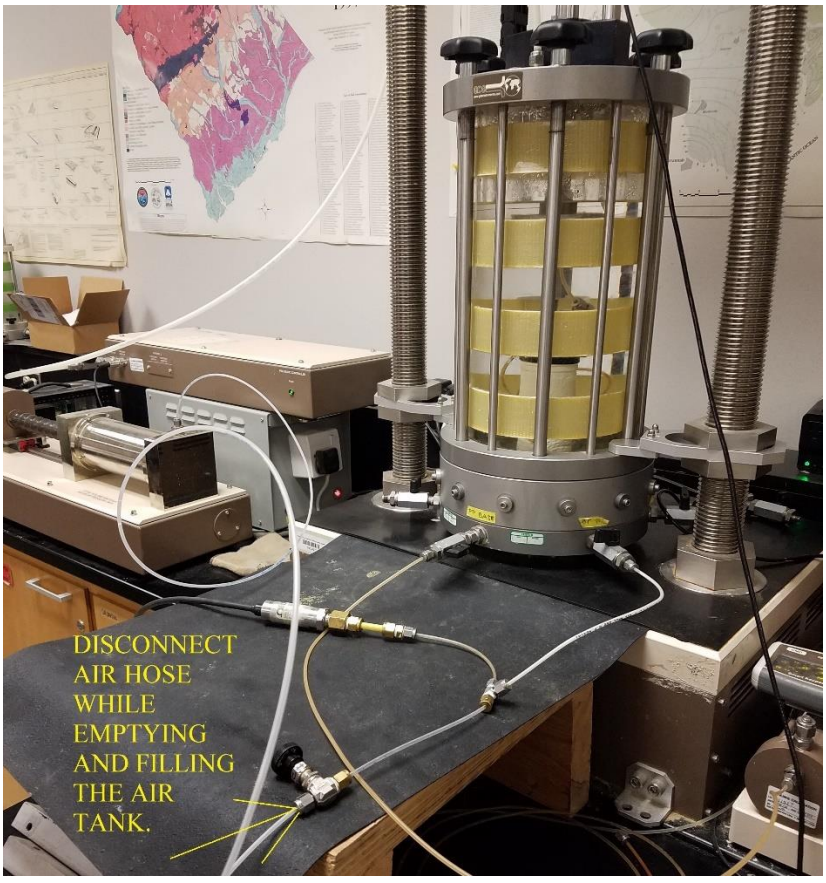

Figure 3.31 – Consolidation stage hose assembly

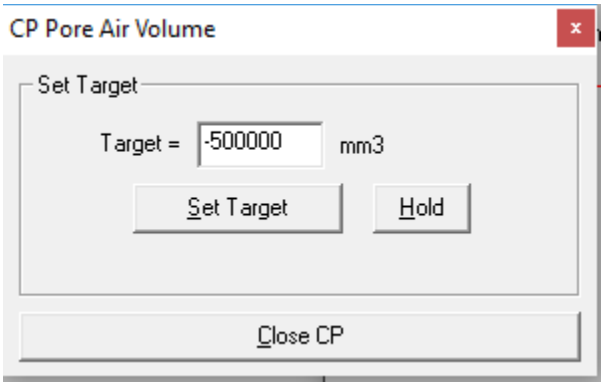

Figure 3.32 – Air tank volume dialog box

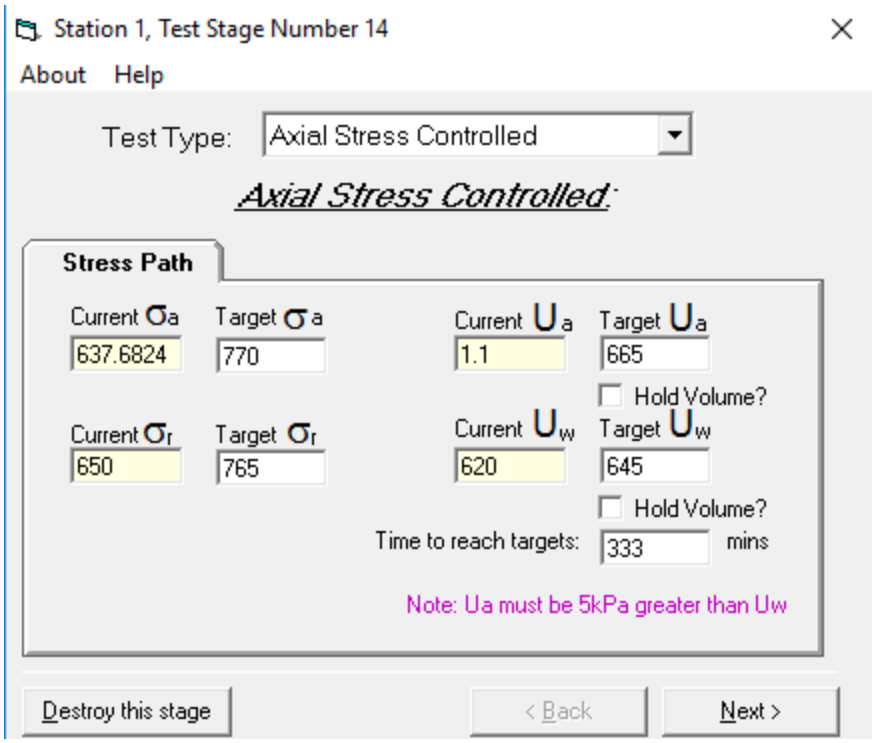

Figure 3.33 – Input stage for consolidation pressures

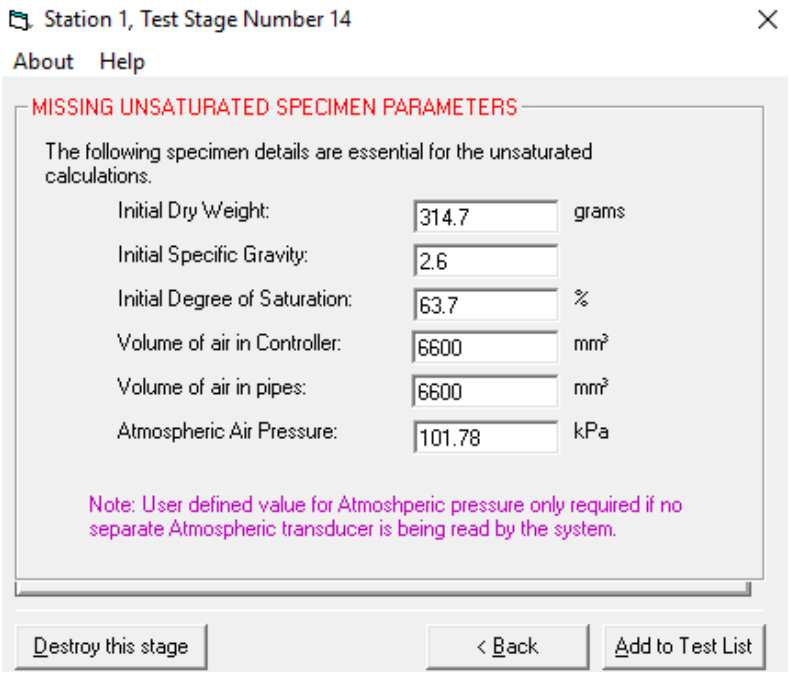

Figure 3.34 – Input for volume of air in the hoses

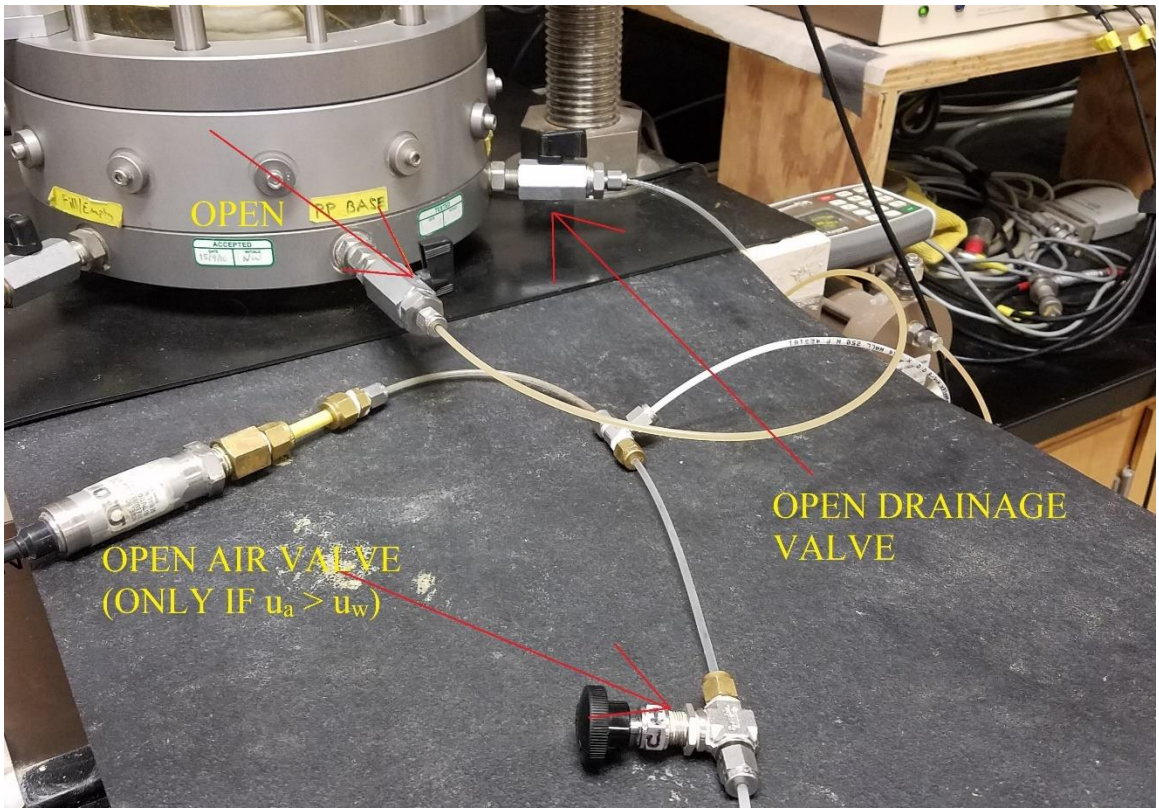

Figure 3.35 – Valve arrangement used in the consolidation stage

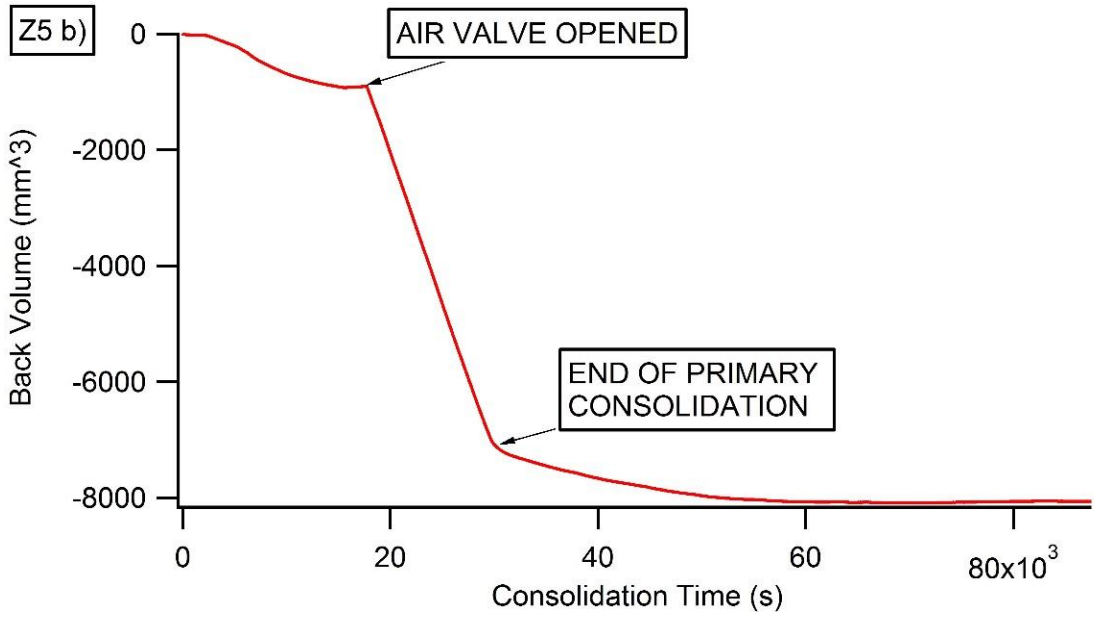

Figure 3.36 – Time versus back volume plot used for determining end of consolidation

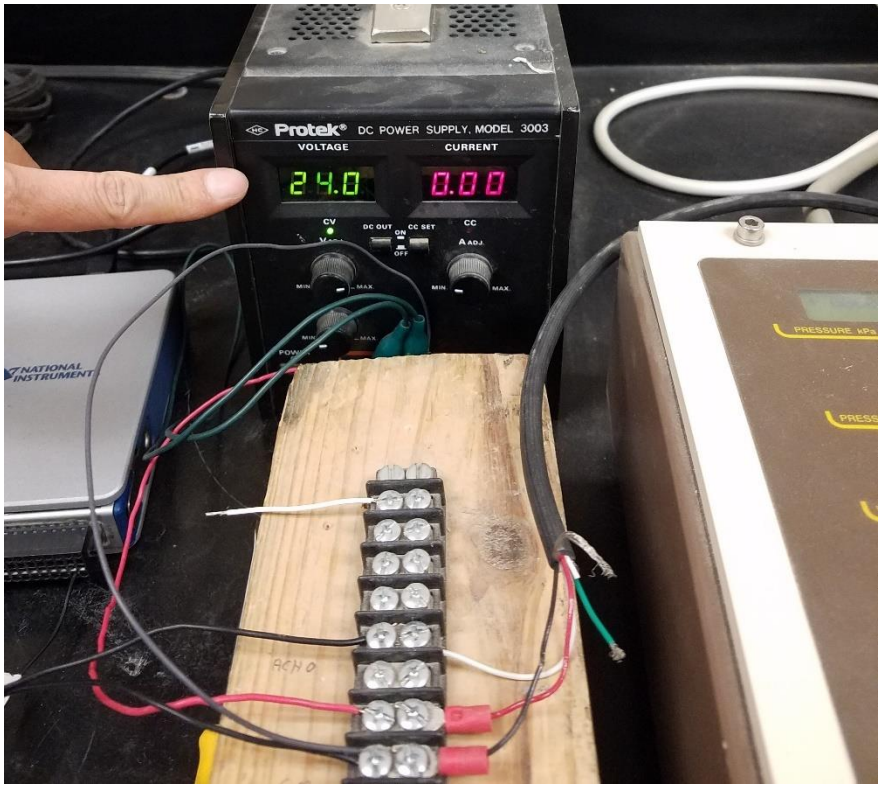

Figure 3.37 – Power source for air pressure sensor

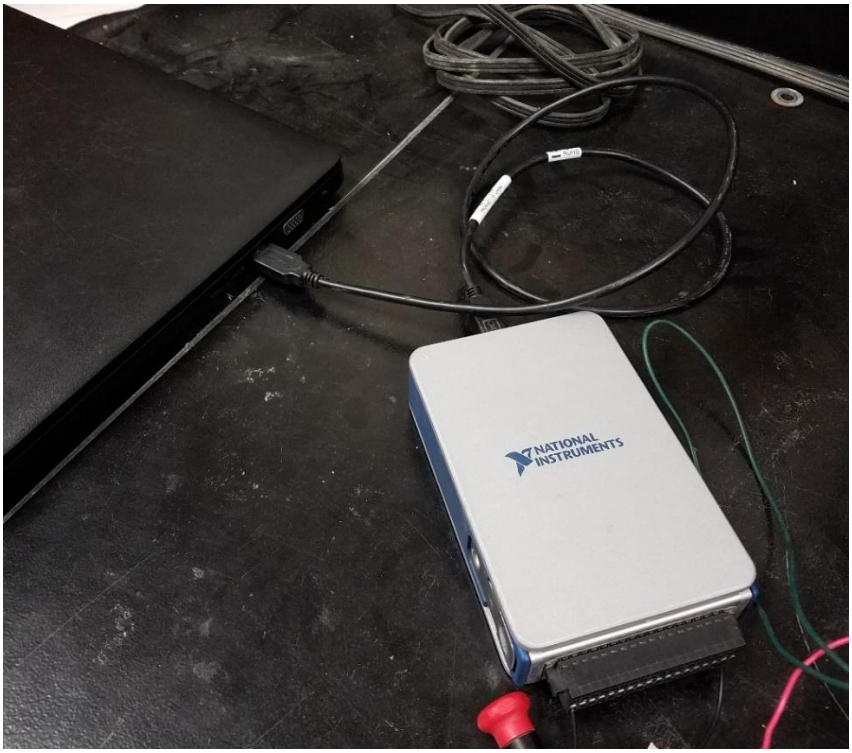

Figure 3.38 – Chassis used for air pressure recording

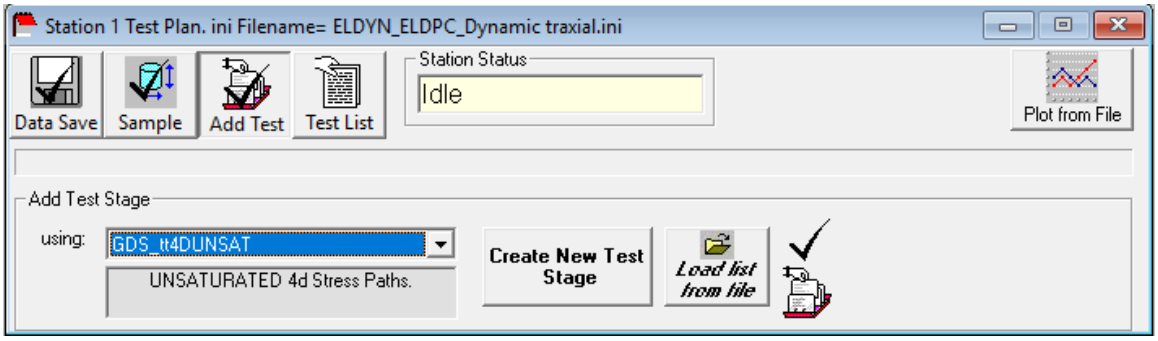

Figure 3.39 – Selection of unsaturated cyclic triaxial test type

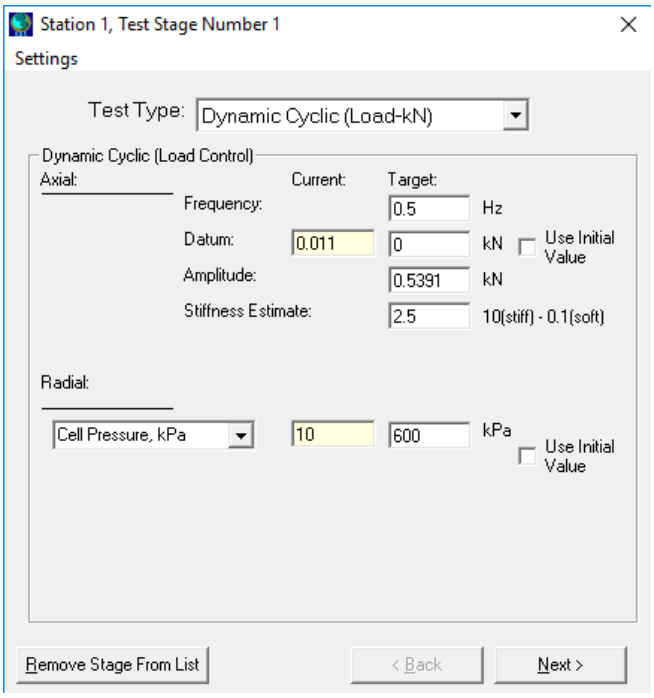

Figure 3.40 – Dynamic parameter input

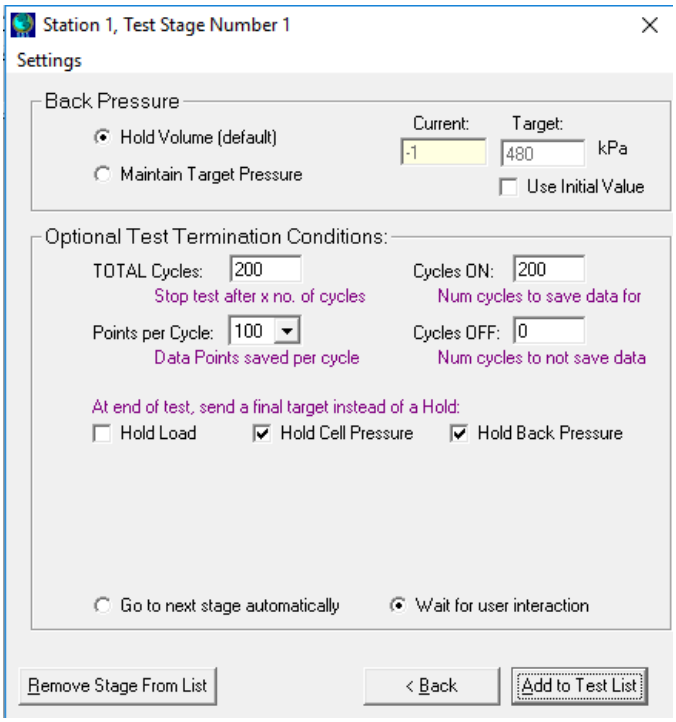

Figure 3.41 – Number of cycles input

CHAPTER 4

RESULTS AND DATA ANALYSIS

4.1 – Introduction

This chapter presents results collected from two series of unsaturated cyclic triaxial tests on silty sand (SM). Thirteen tests were conducted in two series named the "M-series" and "Z-series," respectively. Section 4.2 describes the testing program followed, while section 4.3 provides a detailed summary of the general specimen behavior observed during the study. Section 4.4 discusses the differences in specimen cyclic resistance between the wetting and drying paths. Section 4.5 describes the effects of net normal stress on the specimen cyclic resistance. Section 4.6 discusses the positive trend between increased matric suction and increased specimen cyclic resistance.

Variables considered in this study include matric suction, net normal stress, cyclic stress ratio, specimen density as well as wetting and drying specimen preparation techniques. The effect of matric suction is important because increased specimen stiffness can occur when matric suction is applied to the test specimen, as shown by Ghayoomi et al. (2017). The net normal stress, the difference between the triaxial cell pressure and pore air pressure, is representative of the effective stress of unsaturated soil. As with increased effective stress in saturated soils, unsaturated soils with increased net normal stress experience higher stiffness and strength. Specimen density has a significant impact on the cyclic resistance of both saturated and unsaturated soils. Also, the density of unsaturated

soil specimens greatly affect the degree of saturation of the specimens at a given matric suction as looser specimens will have a lower degree of saturation than denser soils (Fredlund & Xing, 1994). The effect of the wetting and drying path is important because specimens prepared using the wetting path tend to have higher specimen stiffness than those prepared using the drying path, as found by Khosravi et al. (2016).

The current understanding of the effects of matric suction, net normal stress, cyclic stress ratio, density, and drying or wetting path on cyclic resistance is currently limited. Furthermore, unsaturated mine tailings materials have not received extensive study focused on cyclic resistance. This study was performed to improve the understanding of unsaturated silty sand with a significant fine content which can be used to represent common mine tailings materials. The findings of this study can also be used in the analysis of unsaturated soils located above the groundwater table in natural soil deposits.

Many differences exist between the M-series and the Z-series. The cyclic stress ratio (CSR) was varied throughout the M-series tests, while a CSR of 0.20 was used for all Z-series tests except test Z1. The M-series focused on the effect of the wetting and drying paths on specimen behavior. The Z-series focused on the variation of matric suction while also utilizing a lower dry density than that used in the M-series, keeping all other input variables the same for each test.

4.2 – Soil Properties & Testing Program

The soil utilized during the study was a non-plastic silty sand (SM) which was representative of a mine tailings material. The fines content of the soil was particularly high at 39.3% while also possessing a plasticity index (PI) of only 1.0. Soil properties

including liquid limit (LL), plastic limit (PL), specific gravity (G_s), optimum moisture content (w_{opt}), soil classification, coefficient of uniformity (c_u), and coefficient of curvature (c_c), are shown in Table 4.1. The grain size distribution was plotted as shown in Figure 4.1. Due to the lack of cohesion in the soil, all soil specimens had to be compacted within a rigid mold within the triaxial cell. The M-series was conducted between October 2019 & January 2020, while the Z-series was conducted between January 2021 & April 2021. The M-series encompassed the variation in net normal stress, matric suction, pore air and pore water pressure, and cyclic stress ratio. For greater comparability between specimens with different matric suctions, the Z-series tests only varied initial matric suction. While the dry density of the specimens used in the Z-series is lower than those used in the M-series, the dry densities used in the Z-series were kept relatively constant.

Table 4.2 gives the initial, as-compacted conditions of the soil specimens for each test. Table 4.3 shows the specimen properties at the end of primary consolidation (EOC) as well as the test results. Soil specimen density classification was based on US Army Corps of Engineers Table 3-1, EM 1110-1-1905 (1992). At the EOC, the relative density (D_r) of the M-series specimens ranged from 81.6 to 98.0% and were considered very dense. The range of values of D_r for the Z-series tests was lower than for the M-series tests, ranging from 59.2 to 81.6%, and was classified as dense. All M-series tests except M6 achieved a higher D_r during consolidation. Conversely, all Z-series specimens except Z5 developed a lower D_r than the as-compacted D_r. It was found that specimens consolidated with an initial net normal stress (σ_{no}) of 500 kPa developed a higher relative density than those consolidated at 100 kPa. For instance, specimen M1, consolidated at σ_{no} of 500 kPa, experienced a D_r of 95.9% while specimen M5, consolidated at σ_{no} of 100 kPa, developed

a D_r of 91.8%. Also, specimens prepared using the wetting path procedure developed higher Dr values than those prepared using the drying path procedure. Wetting path specimen M1 experienced a D_r of 95.9%, while drying specimen M6 developed a D_r of 81.6%. This is a key factor contributing to the higher cyclic resistance of the wetting path specimens compared to the drying path specimens.

For both the M-series and Z-series, the failure criteria used for each specimen was considered a double-amplitude axial strain (DA_ε) of 5%. All tests were tested at a frequency of 0.05 Hz. This frequency was slow enough to allow even pore water pressure distribution throughout the specimen while also being fast enough to realistically represent an earthquake seismic load. The failure criterion, as well as cyclic frequency, are taken from Tsukamoto et al., 2014.

The Poisson's ratio (ν) of the unsaturated soil specimen was unknown and could not be directly measured given the testing apparatus. In order to calculate the change in volume of the specimen during consolidation as well as the change in the void ratio (e), a value of ν must be estimated. For initial calculations, a value of ν of 0.5, the Poisson's ratio of an incompressible fluid, was used to find the value of e and degree of saturation (S). However, the pore air within the specimen is compressible, and a lower value of ν should be used to accurately measure the volume change. A sensitivity analysis was conducted to assess the effect of ν on e, and S. Four trials were conducted using values of ν of 0.50, 0.45, 0.40, and 0.35, respectively. It was found as ν decreases, e generally increases while S generally decreases. The magnitude in a change of e and S was less than 5% for all four trial ν values. Changes in e and S between values of ν of 0.40 and 0.35 were very small, and it was determined smaller values of ν would yield similar values of e and S. A Poisson's

ratio of 0.40 was selected for use in the study for all specimens. This value accounts for the incompressibility of the pore water while also accounting for the compressibility of pore air.

4.3 – General Behavior

4.3.1 – Cyclic Parameters Discussion

This section describes the general cyclic behavior of the soil specimens tested during the study, and all figures are arranged in a fashion typical for analysis of liquefied, saturated soil specimens. The parameters needed for the analysis include the cyclic stress ratio (CSR), the net normal stress (σ_n), the initial net normal stress (σ_{no}), axial strain (ε_a), double amplitude axial strain (DA_ε), matric suction (ψ), pore water pressure (u_w), and pore air pressure (u_a). The CSR is calculated using Equation 4-1 and is the normalized driving shear stress in proportion to the σ_{no} that causes failure of the specimen (Idriss & Boulanger, 2008). The σ_{no} must be used when calculating the CSR because if σ_n is used, the calculated CSR will be larger than the CSR applied during the cyclic test because the σ_n reduces throughout the test. In saturated soil, the CSR is defined as the cyclic shear stress divided by the vertical effective stress. This definition cannot be used in this study due to the specimens not being fully saturated with water. The net normal stress can be thought of as the net confining pressure for unsaturated soils and is defined as the difference between the triaxial cell pressure and u_a. When this parameter approaches zero, very large axial deformations occur in the specimen as the shear strength greatly reduces, following a behavior similar to soil liquefaction.

$$CSR = \frac{qcyc}{2\sigma no} = \frac{maximum\ cyclic\ shear\ stress}{2 \times initial\ net\ normal\ stress} \quad (4\text{-}1)$$

The double amplitude axial strain is the difference between the largest positive and largest negative axial strain during a single cycle. The failure criteria for the test specimens was a DA_ε of 5%, as suggested by Tsukamoto et al. (2014). In specimens that achieved a DA_ε greater than 5%, the specimen stiffness reduced to nearly zero, indicating liquefaction as shown in Figure 4.2d). The largest difference between saturated and unsaturated specimens is the presence of matric suction, ψ, which is defined as the difference between the u_a and the u_w. A positive matric suction, where the u_a is greater than u_w, will desaturate a fully saturated specimen until the flow rate of water into and out of the specimen ceases.

4.3.2 – Comparison of Failed and Non-failed Specimens

Tests Z4 and M3 represent the general behavior of the test specimens, and these are shown in Figures 4.2 and 4.3, respectively. Test M3 developed a DA_ε of 0.19% at 200 cycles, indicating the stiffness of the specimen was nearly unchanged throughout the test. Test Z4 developed a double-amplitude axial strain of approximately 7% at 76 cycles. Test M3 followed the wetting path while Tests Z4 followed the drying path. This likely led to the difference in behavior during the cyclic triaxial test.

Test Z4 is a sample that developed significant axial strain at failure. The specimen had a reduction in ψ from 26 kPa to 0 kPa at failure due to a build-up of u_w. At approximately the same cycle, the rate of axial strain development increased significantly, leading to a sudden failure. This also corresponds to a reduction in σ_n to approximately 40 kPa, a 60% decrease. The reduction in σ_n is significant because σ_n is essentially the effective stress of the unsaturated soil. As the u_a increases, the effective confinement reduces,

leading to a great reduction in the shear strength of the soil. The net normal stress decrease can be seen in Figure 4.2 c). In general, u_a increases at a significantly slower rate than u_w.

In contrast, test specimen M3 did not have a significant reduction in matric suction or net normal stress due to a lack of u_a and u_w build-up. The resulting axial strain for this specimen is very small in comparison to Test Z4. The initial matric suction (ψ_o) for this specimen was also lower than Test Z4 at 15 kPa. Both specimens were consolidated at the same initial σ_n of 100 kPa. The main difference between these specimens is the consolidation path used during their sample preparation. Test Z4 followed the drying path, while test M3 followed the wetting path. This shows that the way in which the specimen is prepared has a significant impact on the cyclic resistance of soil specimens. Also, unlike test Z4, the stiffness of specimen M3 was essentially constant throughout the test.

Since the objective of the Z-series was to analyze the cyclic resistance of the unsaturated soil with initial matric suction (ψ_o) as the only independent variable, the only difference between Tests Z4 and Z5 is the initial matric suction of specimen Z5 of 21 kPa. Specimen Z5 received 41 cycles before failing, precisely 35 cycles less than specimen Z4. Even with just a 5 kPa difference in ψ_o, the failure mode is significantly more gradual for specimen Z5 than for Test Z4. The cyclic behavior of specimen Z5 is shown in Figure 4.4. In a comparison between Tests Z2, Z4, and Z5, it can be seen that as the matric suction increases, with all other parameters constant, the number of cycles at failure increases.

A difference in the loading and unloading paths exists, creating a “loop” when the axial strain and CSR are plotted against each other. This is exemplified by Test M2, shown in Figure 4.5. The lower half of the loop represents the loading path, while the upper half depicts the unloading path. The loop maintains relatively the same shape throughout the

test, even after many cycles. This is the expected behavior for un-failed specimens. The area inside the loop represents the damping of the specimen or the amount of energy that is dissipated in the soil mass. Since the loop remains relatively constant, the damping of the specimen also remained relatively constant.

Liquefaction is typically identified when the specimen stiffness is reduced to near zero. To identify this phenomenon, the axial strain and CSR for specimen Z4 are plotted against each other, as shown in Figure 4.6a). When a line is drawn in between the origin of the plot and the upper right-hand corner of the "inverted S-shape," the stiffness of the specimen can be calculated as the slope of this line. As the cyclic triaxial test progresses, the slope of this line reduces significantly. As the specimen approaches failure, the constant applied CSR causes ever higher axial strains. The middle portion of the S-shape, the near-horizontal line close to the CSR value of zero, extends farther to the right and left of the origin as failure approaches. This is a sign that liquefaction is occurring. The area contained within each successive S-shape increases, representing an increase in damping.

Test M6 experienced the same general behavior as Test Z4 but achieved a much higher strain before the test was stopped. It can be seen in Figure 4.6b) at high strains, the specimen stiffness continues to reduce while the S-shape takes on a more oval shape which could be an indication that higher damping occurred at high strains. Also, at very high strains, the target CSR is not achieved due to the severe reduction in specimen stiffness. In contrast, Test Z4 achieves a CSR higher than the target value at high strains. The difference in the value of late-stage CSR is an area for further research. It could possibly be an impact of the expansion and contraction of the diameter of the specimen during late-stage, high axial strains. The diameter of the specimen cannot be measured during the test due to

equipment limitations, and the diameter is used in the calculation of the CSR. It is recommended in future studies that a diameter measurement system be installed in the cyclic triaxial device.

4.3.3 – Cyclic Behavior of Non-failed Specimens

Unlike tests M6, Z2, Z4, and Z5 tests M1, M3, and Z3 maintain a near-constant stiffness throughout the test. The stiffness is found by calculating the slope of the line that bisects the loading-unloading stress-strain loop. This slope was found for both the first and last cycles for each of the compared tests. Test M1 has a σ_{no} of 500 kPa and has the lowest void ratio of the three tests. Test M1 also has the largest change in stiffness with an increase of 18%. This increase in stiffness is attributed to the densification of the soil specimen during the test. Test M3 has the highest initial stiffness of the three specimens despite having net normal stress lower than M1. This is surprising since specimens with high confining pressure tend to have stiffnesses higher than specimens with lower confining pressure. Test M3 had the lowest degree of saturation of the three tests, which likely led to its high stiffness. Its reduction in stiffness was relatively small at 2.3%. Test Z3 had the smallest change in stiffness of the three tests with a decrease of 2.1%. Figure 4.7 shows how the slope of the stiffness lines has minimal change throughout the tests. Unlike any of the other tests from the M-series or Z-series, test Z3 was conducted as a drained test. This prevented the development of u_w and u_a, allowing for a near-constant σ_n throughout the test, as seen in Figure 4.8e. The corresponding ε_a of test Z3 was 0.36% which is comparable to the ε_a for test M1 at 0.53%. It can be seen that the Z3 drained test with a σ_{no} of 100 kPa behaved similarly to the M1 undrained test, which possessed a σ_{no} of 500 kPa. Test Z3 also

had a significantly higher void ratio of 0.81 compared with test M1 which had a void ratio of 0.62.

4.3.4 – Drained versus Undrained Specimen Comparison

A comparison can be made between tests Z3 and Z4, as the only difference between the two specimens is Z3 was conducted as a drained cyclic test. The first 10 cycles of each test were analyzed and compared, yielding surprising results. The stiffness of the specimens increased drastically between the first and tenth cycles as the specimens densified. The stiffness of specimens Z3 and Z4 increased by 55% and 103%, respectively. A visualization of the stiffness increase can be seen in Figure 4.9, while the variation of matric suction can be seen in Figure 4.10. While the stiffness of specimen Z3 remained returned to nearly its original stiffness by the end of the test, the stiffness of specimen Z4 reduced to nearly zero as the soil liquefied. Due to the ability of the pore water in specimen Z3 to drain during the test, the matric suction remained near-constant throughout the test. On the other hand, the matric suction of specimen Z4 reached zero at approximately 60 cycles.

4.4 – Path Effects

4.4.1 – Specimen Preparation Procedures

The specimen preparation procedures for the wetting and drying paths are similar except for two additional stages in the drying path procedure. Both procedures begin the same with soil and water mixing in a pan. The specimens are prepared in a rigid mold inside the triaxial device. The procedures deviate when de-aired water is flushed through the specimen for the drying path. After the target de-aired water volume is flushed, the specimen is saturated by applying several stages of high cell pressure and back pressure.

The degree of saturation is approximated using the "B-check" test at the end of each saturation stage in which the B-value developed by Skempton (1954) is measured.

Once a B-value of 0.90 is achieved, the specimen is considered sufficiently saturated, and the specimen is ready for consolidation. For the drying path, the specimen is "dried out" as the pore air pressure is developed within the specimen and pore water is forced out. The wetting path does not incorporate a flushing or saturation stage, instead of moving directly to the consolidation stage. Unlike the drying path, the specimen is "wetted" during consolidation for the wetting path procedure. The two procedures reconverge at the end of consolidation when it is determined that the primary consolidation has been reached.

Back volume, or the volume of the back pressure tank, is used in the consolidation stage of the specimen preparation process to observe the change in pore water volume in the specimen. A positive back volume change is where water flows into the specimen from the back pressure tank. A negative back pressure change is when pore water flows out of the specimen. Drying path consolidation causes a negative back volume change as water flows out of the specimen. Wetting path consolidation causes a positive back volume change as water flows into the specimen. The change in back volume is not considered the same as the specimen volume change. The change in back volume is considered only a change in the amount of pore water in the specimen, not a change in the total specimen volume.

In general, as the matric suction increases, the amount of negative back volume change increases for the drying path specimens. As the matric suction increases, the amount of positive back volume change decreases for wetting path specimens. A drying path example, test Z4 had a higher matric suction than test Z5 and also had a larger negative

back volume change, approximately 4 mL. A wetting path example, test M1 had a higher matric suction and had a smaller positive back volume change than test M5. This can be seen in Figure 4.11.

A delay exists between the end of primary consolidation (EOC) and the stabilization of axial strain during consolidation. For example, specimen Z5 experienced a delay of approximately 2 hours between the stabilization of axial strain and the EOC, as can be seen in a comparison of Figures 4.11 and 4.12. For the wetting tests M1 and M5, water entered the specimens during consolidation even though the specimen volume decreased due to consolidation. Test M5, which experienced the smallest strain during the consolidation of approximately 1.3%, experienced the most water infiltration out of tests Z4, Z5, M1, and M5. This is due to the small matric suction value of 5 kPa for test M5, which is smaller than the other three tests.

All specimens tested in the M-series and Z-series experienced positive axial strain during consolidation, as the specimen height of all specimens decreased. Drying path specimens Z4 and Z5 experienced consolidation axial strains of approximately 1.5 and 5.0%, respectively. However, specimen Z4 experienced a higher negative back volume change at approximately 12.0 mL than specimen Z5, which experienced a negative back volume change of 8.0%. This shows that back volume change did not correspond with higher axial strain during consolidation for drying path specimens. The same is true for wetting path specimens, as specimen M1 experienced a higher axial strain at 2.5% than specimen M5, which experienced an axial strain of 1.3%. Even though specimen M1 had a higher axial strain than M5, M1 experienced a positive back volume change of 4.5 mL while M5 experienced a positive back volume change of approximately 17%. Back volume

change is independent of axial strain during consolidation for both wetting and drying path specimens.

Due to equipment limitations, the degree of saturation (S) at the end of consolidation had to be calculated after the test. This was done by creating a phase diagram in a spreadsheet form that accounted for the change in specimen volume from the as-compacted condition through the consolidation process. To solve for the volume change, an assumption had to be made for Poisson's ratio, and a value of 0.4 was selected as previously explained. This value was justified as the soil particles, and pore water was considered incompressible while the pore air was considered compressible. The spreadsheet calculation table used for test Z5 is shown in Table 4.5. Identical spreadsheets to the one shown in Table 4.5 were used to determine the S, void ratio (e), and dry unit weight (γ_{dry}) for all specimens shown in Table 4.3.

4.4.2 – Comparison of Results to the SWCC

The soil-water characteristic curve (SWCC) is the relation between matric suction (ψ) and degree of saturation (S). As ψ increases, S will decrease in a non-linear fashion. Studies have shown that the permeability of a given soil also differs by several orders of magnitude based on the degree of saturation (Genuchten, 1980; Fredlund & Xing, 1994). Similar to loading-unloading paths, SWCCs experience a hysteresis between the wetting and drying paths. Depending on the path chosen for specimen preparation, the test specimen will fall along with the drying or wetting SWCC. The SWCC is also significantly affected by specimen density as denser specimens will experience higher degrees of saturation at equal matric suction values to looser specimens (Fredlund & Xing, 1994). Essentially, a denser specimen SWCC will appear above a loose specimen SWCC when

plotted on the same graph. In Figure 4.13, the drying SWCC for the M-series specimens plots above the estimated wetting SWCC for the M-series, showing that specimens along the drying path will experience higher degrees of saturation than those along the wetting path. Also, in Figure 4.13, since the Z-series specimens were slightly less dense than the M-series specimens, the estimated drying path SWCC is plotted below the M-series drying path SWCC. The wetting path SWCC for the M-series and the drying path SWCC for the Z-series were estimated because these curves were not measured during the study.

When analyzing the M-series tests, M6 and M7 appear close to the drying SWCC while the rest of the tests plot close to the wetting SWCC. This is expected because M6 and M7 were prepared using the drying path consolidation method while the rest of the tests were produced using the wetting path. However, the Z-series tests, which were created using the drying path, plot close to the wetting SWCC. This is likely due to the Z-series specimens possessing lower dry unit weights (γ_{dry}). The wetting SWCC was not measured for this study, and therefore it was estimated. Tests involving matric suction above 30 kPa were not considered in this study. This is an area where further research can be conducted.

The best two tests to compare to see the path effects are tests M3 and M6. These specimens were consolidated at the same σ_{no} of 100 kPa as well as equal ψ_o of 15 kPa. Test M3 had a void ratio (e) of 0.68 and S = 69.5% while M6 had an e of 0.73 and S = 94.4%. Specimen M3 was prepared using the wetting method, while M6 was prepared via the drying method. Both specimens were loaded with a CSR of 0.25.

The cyclic behavior of the two specimens was drastically different as test M3 received 200 cycles without failure while test M6 failed catastrophically at 32 cycles. The increase in u_w for test M3 was 4.5%, whereas the u_w increase in test M6 was 15%. The σ_{no}

for test M3 was relatively constant throughout the test, decreasing by 3.4%. In contrast, test M6 had a reduction in σ_{no} of 100%, reaching zero by the end of the test. Figures 4.3, 4.14, and 4.15 provide visualizations of the stark contrast between the behavior of the two specimens.

The main reason that Test M3 was more resilient is that the degree of saturation for this specimen is 69.5% compared to 94.4% for Test M6. Pore water in Test M3 would redistribute throughout the specimen during shearing, filling voids that previously only contained pore air, preventing localized u_w buildups that would lead to failure. The capacity for pore water redistribution throughout specimen M6 would be lower since the S is much higher in this specimen. The difference in the degree of saturation, or hysteresis, for these two specimens is due to the "ink-bottle effect" as proposed by Hillel (1980). Water infiltrating into dry soil will experience much more resistance to flow due to the ink-bottle effect than water flowing out of the same soil at the same matric suction. This will cause the degree of saturation for the wetting specimen to be lower than for the drying specimen.

Another possible reason for the wetting path test specimen having a higher strength is a nonuniform distribution of pore water pressure throughout the specimen during the cyclic triaxial test. The non-compressible pore water could have compressed the pore air, allowing for the phreatic surface to rise within the specimen. The movement of water upward through the specimen during cyclic loading would lower the S in the bottom of the specimen since the back pressure valve is closed during the cyclic test, redistributing the water throughout the specimen. The difference in the degree of saturation between wetting and drying specimens is the main contributing factor to increased cyclic resistance in wetting specimens. However, the lack of localized u_w buildup would prevent localized

failure of the specimen that would lead to total failure. It is recommended that future research studies focus on an evaluation of uniformity of pore air and pore water distribution throughout unsaturated specimens in triaxial conditions for both the wetting and drying paths. It may be possible to measure the u_w and ua distribution through the use of pressure sensors placed within the specimen during the sample preparation stage.

It is noted that the time required to prepare the test specimens for the drying and wetting paths are significantly different, with the drying path being the longer of the two. The drying path can be completed in 19 to 23 days, depending on the permeability of the specimen. The drying path requires more time to complete due to the presence of the flushing and saturation stages. These are the most time-consuming phases of the drying path specimen preparation and can take up to 14 days total to complete. The wetting path requires approximately 5 days to complete. The wetting path does not involve flushing and saturation stages and instead moves from specimen compaction to consolidation. However, the absence of the flushing and saturation stages increases the time required for the consolidation stage to approximately 2 days. A process chart representing the steps required for each path is shown in Figure 4.16.

The time required for consolidation varied with each test. Engineering judgment was used to determine the end of primary consolidation. This was done by observing the "time versus back volume" plot as shown in Figure 4.11 and noting the change in curve slope as the end of primary consolidation. The slope of the curve represents the flow rate of pore water out of the specimen during consolidation. No threshold value was selected for the required slope.

Due to the higher ψ for the Z-series tests, the degree of saturation at the end of consolidation tends to be lower than for the M-series tests. For instance, in a comparison of Test M3 and Test Z4, Z4 has a lower degree of saturation than M3. This is expected because Z4 is consolidated with a ψ_o of 26 kPa while M3 experienced a ψ_o of 15 kPa. However, the degree of saturation for the Z-series tests is significantly lower than for the drying tests M6 and M7. This is due to specimens from the Z-series being generally less dense than specimens M6 and M7. This would cause M-series specimens to have smaller void volumes leading to a higher degree of saturation.

4.5 – Net Normal Stress Effects

4.5.1 – Net Normal Stress Behavior of Non-failed Specimens

The magnitude of net normal stress (σ_n) during consolidation leads to varying degrees of axial strain (ε_a) and back volume change. For the triaxial test, a positive axial strain is compressive while a negative axial strain is tensile. Back volume is the amount of pore water that flows in or out of the specimen during consolidation but is not the same as total volume change. A positive back volume change is the infiltration of water into the specimen and was observed in all wetting path specimens. A negative back volume is when water flows out of the specimen and is typical for drying path specimens.

Specimen M1 was consolidated with a σ_n of 500 kPa while specimen M3 was exposed to 100 kPa of σ_n. These two specimens utilized the same initial matric suction (ψ_o), initial dry density (γ_{do}), dimensions, as well as following the wetting path. The axial strains at the end of consolidation were approximately 2.5% and 0.9% for specimens M1 and M3, respectively. Specimen M1 experienced approximately 3 times as much ε_a as specimen M3 due to M1 having a greater σ_n than M3. Despite having significantly different axial strains,

the back volume change of the two specimens is approximately equal at 4,000 mm^3. Figure 4.17 shows the change in ε_a and back volume during consolidation for both M1 and M3, which were each prepared using the wetting path. Each of the specimens densified during consolidation, with e_o decreasing by 16.2% and 5.6% for specimens M1 and M3, respectively. The greater densification of specimen M1 compared to M3 was expected due to M1 having a significantly higher σ_n. For specimens M1 and M3, the S_o also increased by 16.1% and 9.50%, respectively.

The time required for specimens M1 and M3 to reach equilibrium during consolidation varied, while the total back volume change for each sample was approximately the same. The time versus back volume plots shown in Figure 4.17 c) and d) were monitored during the consolidation phase of each test. When the back volume change was minimal, indicating that the specimen reached equilibrium, the cyclic triaxial test was conducted. Specimen M3 experienced drainage behavior that was different than any of the other tests in the M-series or Z-series as the back volume fluctuated differently. Despite the difference in drainage behavior, cyclic triaxial test M3 was conducted after the back volume in the specimen stabilized.

4.5.2 – Net Normal Stress Reduction Effects

While the reduction of σ_n for tests M1 and M3 is minimal, the σ_n variation in tests Z4 and Z5 led to the failure of the specimens. Tsukamoto et al. (2014) also conducted a series of unsaturated cyclic triaxial tests on silty sands and found that the net normal stress (σ_n) decreases throughout the test. The Tsukamoto et al. (2014) study quantified the reduction in σ_n through the use of a net normal stress reduction ratio (r_n) which is the σ_n at failure divided by the initial net normal stress (σ_{no}). They found that for denser specimens

(Dr ~100%) the r_n reduced from 0.9 to 0.3 for initial degrees of saturation of 46% and 70%, respectively. However, the r_n for looser specimens (Dr ~80%), the r_n remained near 0.8 for the same range of initial degree of saturation. This means the denser specimens tested had a much higher reduction in σ_n throughout the test than looser specimens. The r_n for tests Z4 and Z5 were approximately 0.4 and 0.36, respectively. The larger reduction in σ_n for test Z5 is due to the specimen having a lower initial matric suction (ψ_o) and a higher dry density. The higher dry density led to a higher S_o, which led to the subsequent higher reduction in σ_n. This observation agrees with the finding of the Tsukamoto et al. (2014) study that specimens with a higher relative density will have a higher reduction in σ_n compared to looser specimens. Figure 4.18 a) and b) give a visualization of the near-constant σ_n values throughout the tests M1 and M3. In stark contrast, Figure 4.18 c) and d) depict the severe reduction in σ_n throughout tests Z4 and Z5.

A significant difference in stiffness existed between specimens M1 and M3. Specimen M1 was much softer than specimen M3 despite M3 having a much higher σ_{no} and a slightly higher dry density, as shown in Table 4.2. Specimen M3 had a stiffness approximately 3.3 times greater than specimen M1. The stiffness for specimen M1 increased by 17.6%, while the stiffness decreased by 2.3% for test M3.

4.5.3 – Threshold r_n Values

The reduction in net normal stress is the factor that contributes the most to the failure of specimens Z4 and Z5. There is a direct relation between the decrease in σ_n and the increase in double amplitude axial strain (DA_ε). This is best seen during a comparison between Figure 4.3 e) and f) for test Z5. At approximately 33 cycles, the rate of DA_ε development increases significantly, corresponding to an increase in the amplitude of the

σ_n wave. Specimen Z5 fails soon after this σ_n amplitude increase at 41 cycles. The r_n of specimen Z5 at 33 cycles was approximately 0.5 and decreased to 0.36 by cycle 41. Specimen Z4 exhibited similar behavior, experiencing a rapid increase in DA_ε after r_n was reduced to 0.5. For specimens Z4 and Z5, it appears that a r_n value of 0.5 is the threshold value controlling the development of DA_ε. However, the threshold r_n values for specimens M6, M7, and Z2 were approximately 0.3, 0.7, and 0.6, respectively. From these observations, the threshold r_n value cannot be predicted before the cyclic triaxial test is conducted.

4.6 – Matric Suction Effects

4.6.1 – Effects of Matric Suction on Cyclic Resistance

One of the main objectives of the Z-series was to assess the effects of variation in matric suction on the cyclic resistance of the soil. Tests Z2, Z4, and Z5, were prepared using initial matric suctions (ψ_o) of 20, 26, and 21 kPa, respectively. During consolidation, each of these tests was exposed to the same initial net normal stress (σ_{no}), and all specimens were prepared using the drying path. Each specimen developed a slightly different initial void ratio (e_o) and initial degree of saturation (S_o), with test Z5 having the highest dry density (γ_{dry}) of 1.58 g/cm^3.

The identification of specimen failure, the point at which the double amplitude axial strain (DA_ε) equaled 5%, was conducted by measuring the absolute value of the negative and positive axial strains in each cycle. The values of the peak negative and positive axial strains for each cycle were identified by observing the axial strains for each cycle in the data collection spreadsheet generated by the GDS computer software. For example, the point of failure for specimen Z5 was identified by calculating the absolute value of the

axial strains in the cycles leading to cycle 41. Cycle 41 was the first cycle in which DA_ε exceeded 5%. The measured peak positive and negative strains from this cycle are shown in Table 4.5 as well as the calculated DA_ε. The same failure identification procedure was used for all tests conducted in the study.

For ease of comparison, tests Z2 through Z5 were conducted using an equal CSR of 0.20. Tests Z2, Z4, and Z5, show a trend as ψ_o increases, the number of cycles the specimens received before reaching 5% double amplitude axial strain (DA_ε) also increased. As can be seen in Figure 4.19, a trend exists between decreased S_o and an increase in the number of cycles at failure. This finding is supported by a study conducted by Tsukamoto et al. (2014), in which the cyclic resistance was found to increase with a decrease in the initial degree of saturation. The study defined cyclic resistance using the cyclic resistance ratio (CRR), which is the CSR required to cause failure at N = 20 cycles. The Tsukamoto et al. (2014) study found the CRR ranged from 0.5 to 0.19 for initial degrees of saturation of 46% and 99%, respectively. Tests Z4 and Z5 agree with the Tsukamoto et al. (2014) finding, while error in calculating the S_o for test Z2 is likely due to the assumption of a Poisson's ratio of 0.4. The same behavior is seen in Figure 4.14 as the degree of saturation decreases from 94.4% in test M6 to 69.6% in test Z4, and their corresponding number of cycles at failure increases from 32 to 76.

In a comparison of Figure 4.2 f) and Figure 4.4 f), it can be seen that the rate in which DA_ε develops for specimens Z4 and Z5 varies. Specimen Z4 reaches the failure criterion of DA_ε = 5% after a higher number of cycles than Z5 but has a higher rate of strain development in the 5 cycles leading to failure.

As can be seen in Figure 4.20, the average matric suction decreases throughout tests M6, Z4, and Z5 and begins to have larger amplitudes just before failure occurs. The increase in matric suction amplitude corresponds with the increase in axial strain amplitude. The large contractions and dilations the specimens experienced due to the large changes in axial strain caused large variations in u_w and u_a. During positive axial strain, the specimens contracted, causing an increase in u_w and a reduction in matric suction. However, during negative axial strain, the u_w decreased, causing an increase in matric suction. All failed specimens experienced this phenomenon. Any additional stiffness added from suction hardening dissipated when the matric suction reached zero.

Tests M6, Z2, Z4, and Z5, show evidence of liquefaction at failure due to the reduction of the stiffness to nearly zero in the last few cycles of the test. The stiffness of the sample is represented by the slope of the line in between the origin and the corner of the S-curve that is the farthest from the origin. It can be seen in Figure 4.20 that the slope of this line reduced throughout each of the tests to nearly zero.

4.6.2 – Stiffness Increase at Low Matric Suction Values

While the stiffness of the specimens in Figure 4.21 reduced to near zero at the end of the test, the initial stiffness of the first cycle of the specimens varied based on matric suction. As the initial matric suction increased, the initial stiffness increased dramatically. To compare the initial stiffness of the specimens in Figure 4.21, the stiffness of specimens Z2, Z4, and Z5 will be expressed as a percentage of the stiffness of M6. The stiffness of the first cycle was measured by calculating the slope of the line connecting the origin and the top right corner of the first cycle loop in a plot of axial strain versus CSR, as shown in Figure 4.24. Specimens Z2, Z4, and Z5 had stiffnesses of 132%M6, 2152%M6, and

209%M6, respectively. As shown in Table 4.2, the initial matric suction of specimens M6, Z2, Z4, and Z5 are 15, 20, 26, and 21 kPa, respectively. With just a few kPa increase in initial matric suction, the initial stiffness of the specimens increased immensely. It must be noted that the dry densities (ρ_{dry}) and void ratios of these specimens varied, with M6 possessing the highest dry density at 1.58 g/cm^3 and Z4 having the lowest at 1.49 g/cm^3. As can be seen in Table 4.3, the degree of saturation (S_o) for specimens M6 and Z4 is 94.4% and 69.6%, respectively. These two observations show that S_o has a larger contribution to the initial stiffness of the unsaturated specimens than e or ρ_{dry}. Also, specimen M6 was tested with a CSR of 0.25, while specimens Z2, Z4, and Z5 were tested with a CSR of 0.20. Due to the limited number of comparable tests conducted in this study, it is highly recommended that further research be conducted on the initial stiffness of unsaturated silty sand specimens. It is recommended that a study be conducted to measure the maximum shear modulus (G_{max}) of unsaturated silty sand specimens through the use of resonant column tests.

Table 4.1 – Soil grain size and water retaining parameters

Type	w_{opt}	LL	PL	PI	G_s	C_u	C_c	% Fines	D_{50}	D_{30}	D_{10}	e min	e max
-	%	%	%	%	-	-	-	%	mm	mm	mm	-	-
SM or A-4	16	20	19	1.0	2.73	15	3	39	0.08	0.04	0.01	0.64	1.13

Table 4.2 – As compacted weight/volume relationships

	σ_{no}	ψ_o	u_{ao}	S_o	ρ_{dry}	D_r	e_o	Outcome
Test Number	[kPa]	[kPa]	[kPa]	[%]	[g/cm^3]	[%]	[dec.]	-
M1	500	15	100	59	1.56	79.6	0.74	Not failed
M2	500	15	100	60	1.58	81.6	0.73	Not failed
M3	100	15	100	60	1.59	83.7	0.72	Not failed
M4	500	5	100	60	1.58	81.6	0.73	Not failed
M5	500	5	100	60	1.58	81.6	0.73	Not failed
M6	100	15	665	59	1.57	81.6	0.73	Failed
M7	100	25	665	59	1.57	81.6	0.73	Failed
M8	500	10	100	59	1.57	81.6	0.73	Not failed
Z1	100	17	665	77	1.53	75.5	0.76	Failed
Z2	100	20	665	70	1.53	75.5	0.76	Failed
Z3	100	27	665	74	1.53	75.5	0.76	Not failed
Z4	100	26	665	70	1.53	75.5	0.76	Failed
Z5	100	21	665	76	1.53	75.5	0.76	Failed

Table 4.3 – End of consolidation specimen parameters

			End of Consolidation					
Test Number	Poisson Ratio	Path	S_o	e	Dr	ρ_{dry}	ψ_o	σ_{no}
		-	[%]	[dec.]	[%]	[g/cm^3]	[kPa]	[kPa]
M1	0.4	Wetting	75.1	0.66	95.9	1.66	15.0	500
M2	0.4	Wetting	77.9	0.65	97.9	1.67	15.0	500
M3	0.4	Wetting	69.5	0.68	91.8	1.62	15.0	100
M4	0.4	Wetting	89.3	0.67	93.9	1.64	5.0	500
M5	0.4	Wetting	86.4	0.68	91.8	1.62	5.0	500
M6	0.4	Drying	94.4	0.73	81.6	1.58	15.0	100
M7	0.4	Drying	87.8	0.72	83.7	1.59	25.0	100
M8	0.4	Drying	81.8	0.65	98.0	1.65	10.0	500
Z1	0.4	Drying	72.2	0.79	69.4	1.53	17.0	100
Z2	0.4	Drying	69.3	0.84	59.2	1.48	20.0	100
Z3	0.4	Drying	70.8	0.81	65.3	1.51	27.0	100
Z4	0.4	Drying	69.6	0.84	59.2	1.49	26.0	100
Z5	0.4	Drying	73.5	0.73	81.6	1.58	21.0	100

Table 4.4 – Summary of test results

	Test Results					
Specimen	Drainage Condition	CSR	N	ε_a	σ_n	Outcome
		[dec.]	[cycles]	[%]	[kPa]	-
M1	Undrained	0.25	200	0.53	474	Not failed
M2	Undrained	0.35	200	2.46	431	Not failed
M3	Undrained	0.25	200	0.19	97	Not failed
M4	Undrained	0.35	20	5.01	429	Failed
M5	Undrained	0.28	121	2.08	443	Not failed
M6	Undrained	0.25	32	41.0	0	Failed
M7	Undrained	0.30	34	13.3	54	Failed
M8	Undrained	0.35	1	5.10	466	Failed
Z1	Undrained	0.25	1	9.49	100	Failed
Z2	Undrained	0.20	24	7.35	35	Failed
Z3	Drained	0.20	200	0.36	100	Not failed
Z4	Undrained	0.20	76	5.32	43	Failed
Z5	Undrained	0.20	41	5.24	30	Failed

Table 4.5 – Example calculation spreadsheet for degree of saturation at the end of primary consolidation (EOC).

	As-Compacted Condition	After Consolidation Condition	Units
Total density	1.82	1.86	g/cm^3
Dry density	1.53	1.55	g/cm^3
e	0.76	0.74	dec.
S	67.5	**71.6**	%
Wet soil weight	363.95	365.89	g
Axial displacement	-	0.46	cm
Lateral displacement	-	0.23	cm
Poisson's ratio	-	0.50	dec.
Height	9.50	9.04	cm
Diameter	5.04	5.27	cm
Water content	0.16	0.20	dec.
Section area	19.95	21.83	cm^2

Table 4.6 – Peak Positive and Negative Axial Strains for Cycle 41 of Test Z5

	Peak Negative ε_a	Peak Positive ε_a	DA_ε
Cycle	[%]	[%]	[%]
41	-3.700	1.537	5.237

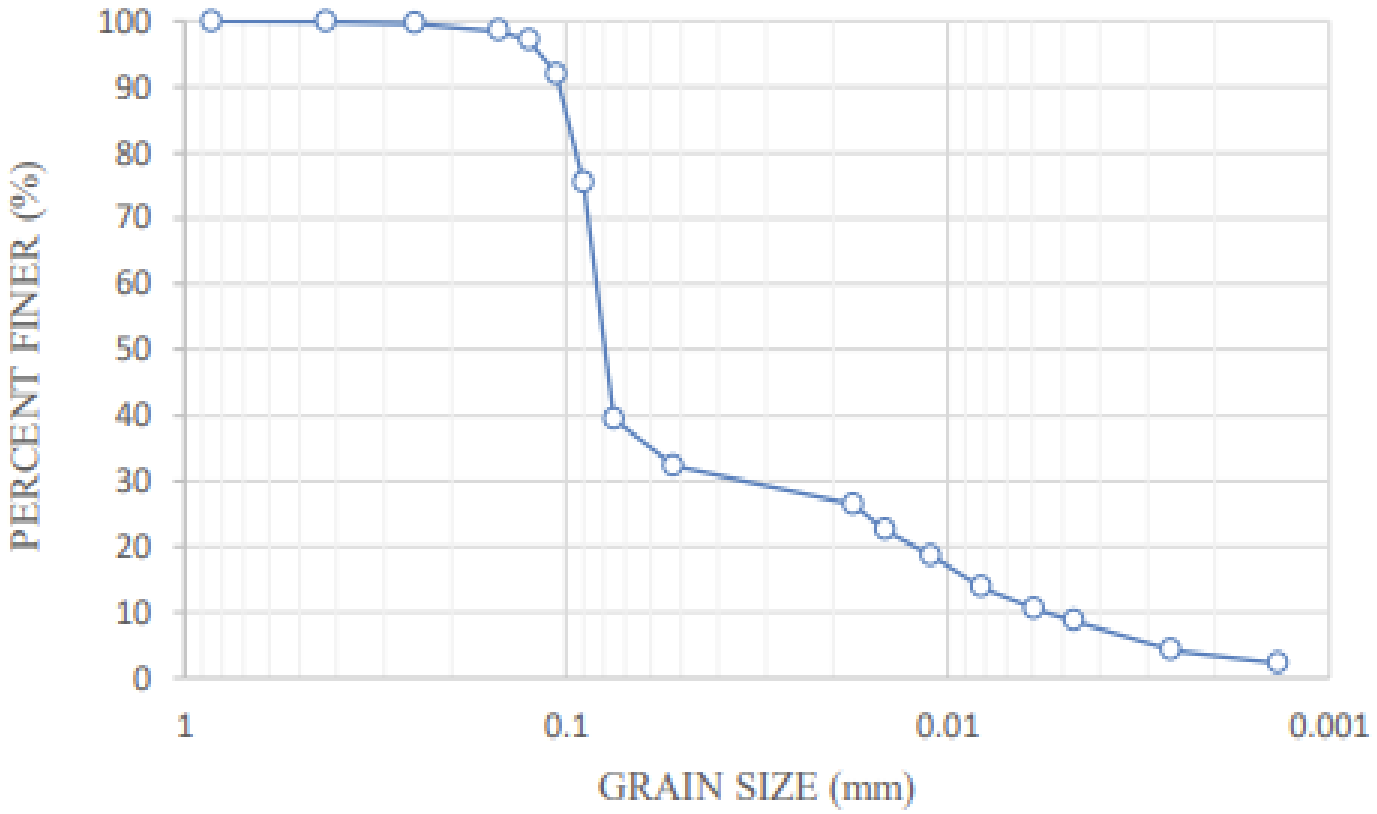

Figure 4.1 – Grain size distribution of the soil

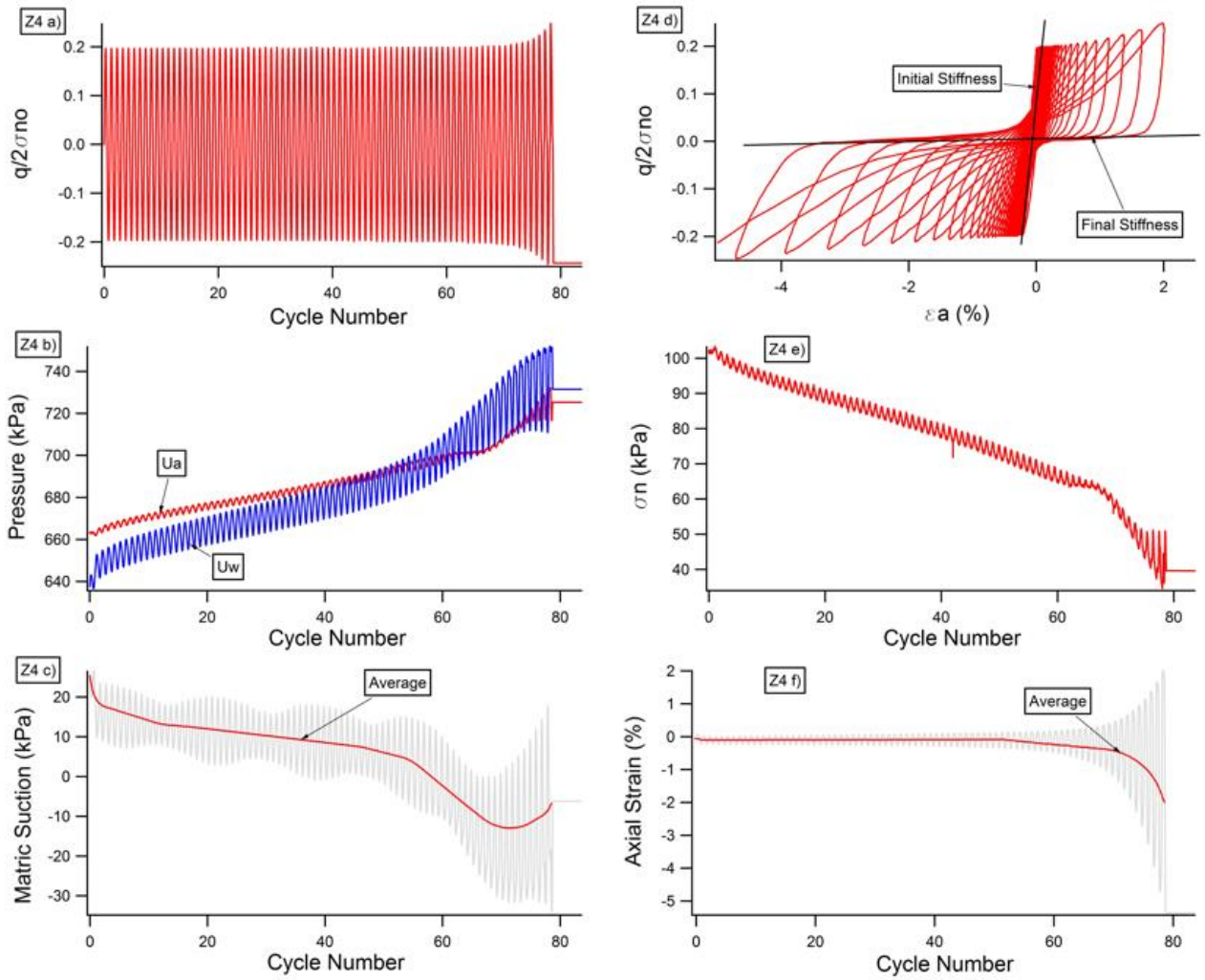

Figure 4.2 – The stress-strain & pore pressure behavior of Z4.

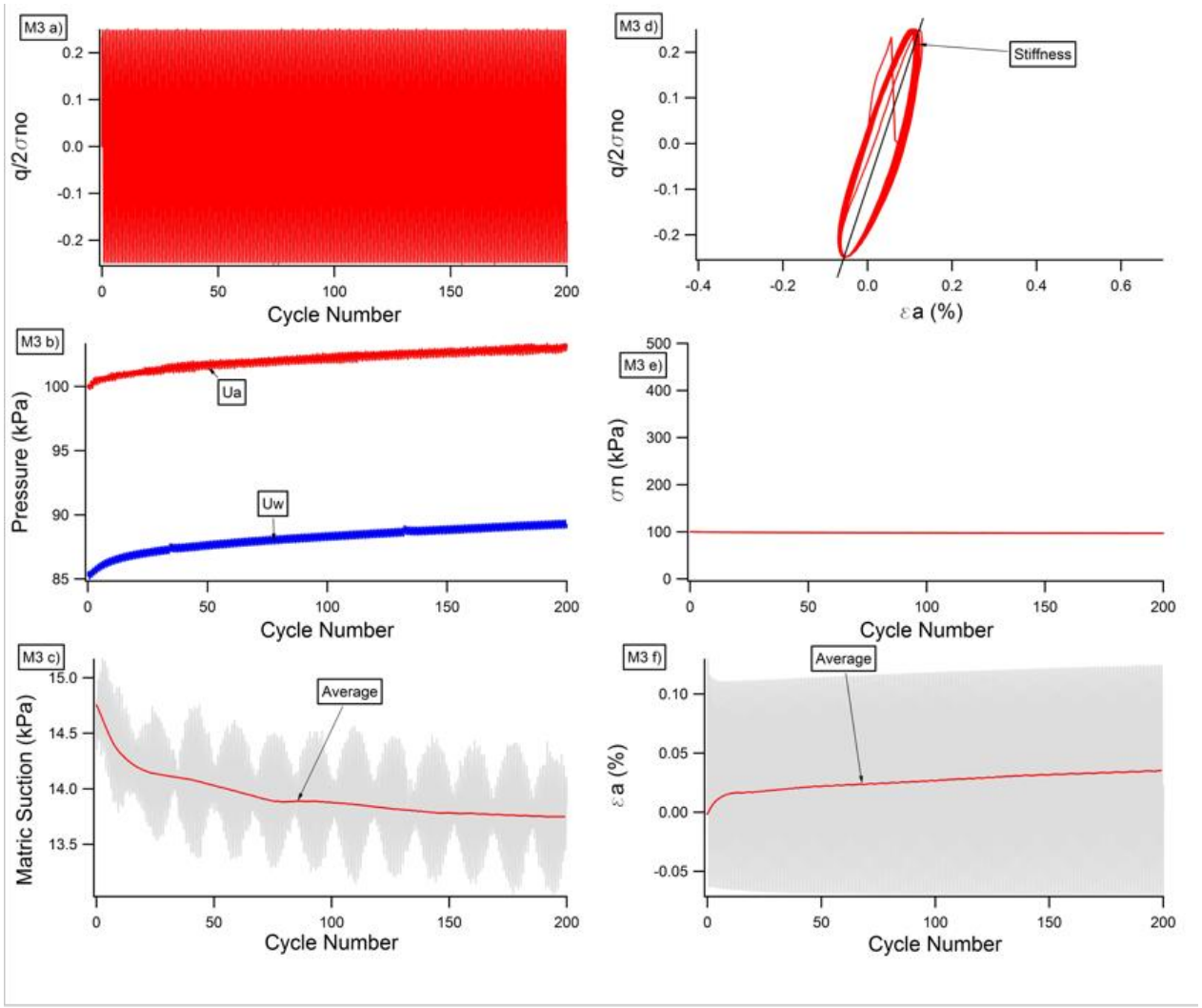

Figure 4.3 - The stress-strain & pore pressure behavior of M3.

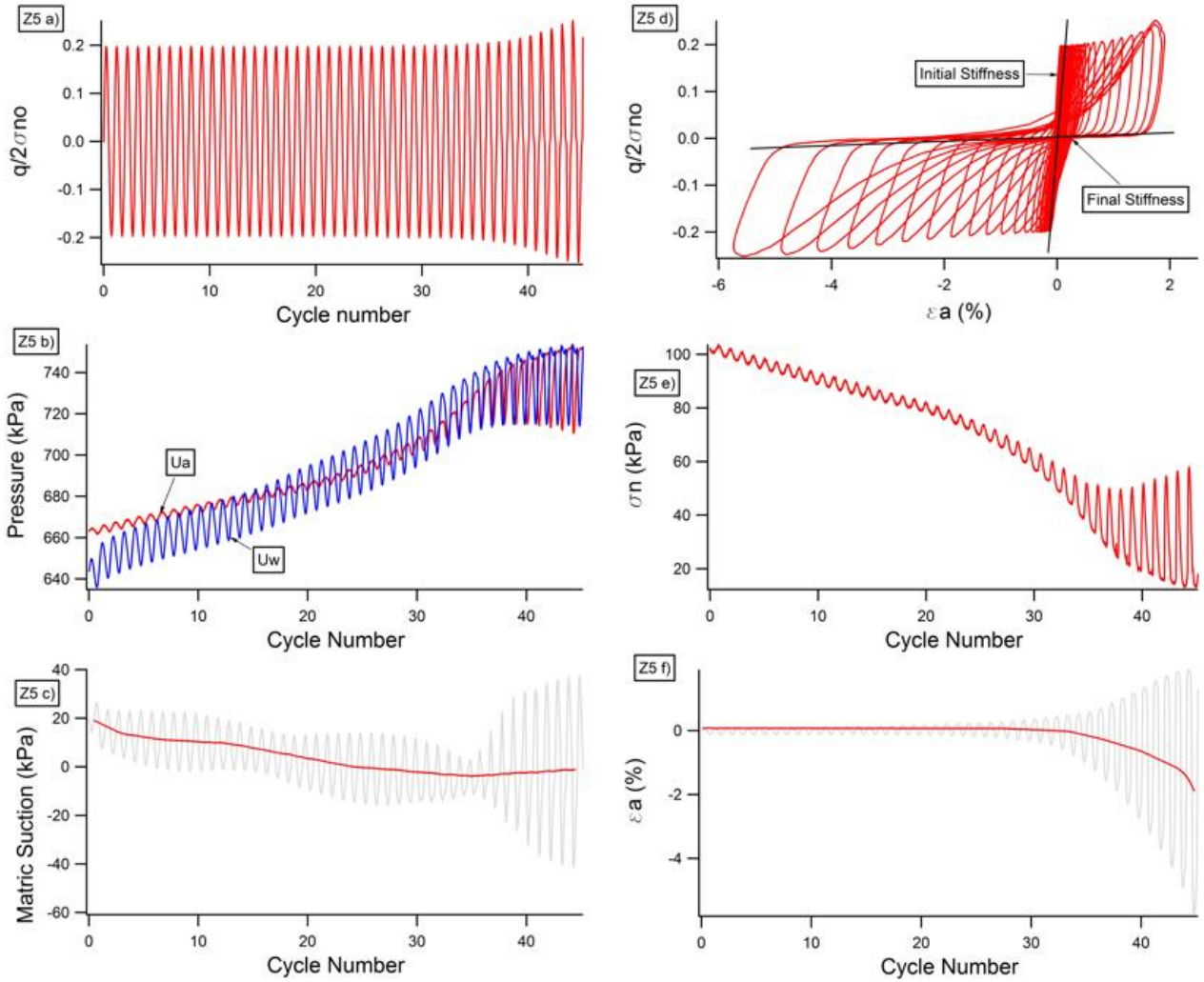

Figure 4.4 - The stress-strain & pore pressure behavior of Z5.

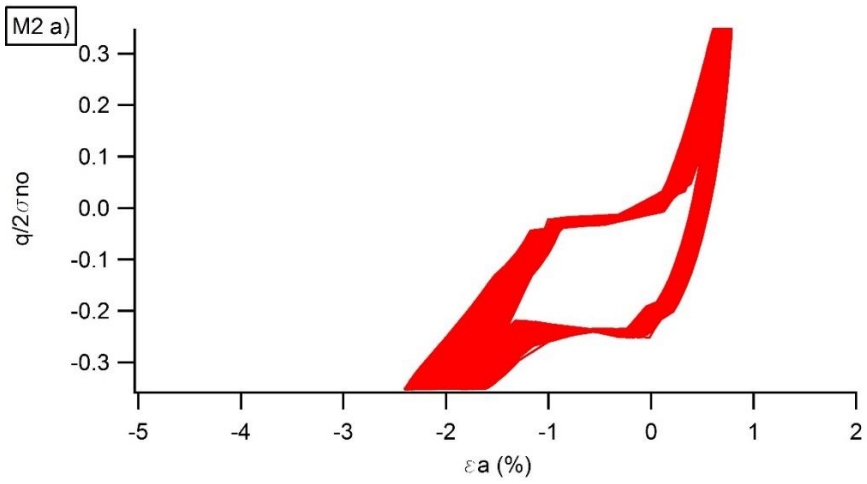

Figure 4.5 – The load-unload loop for un-failed specimen M2.

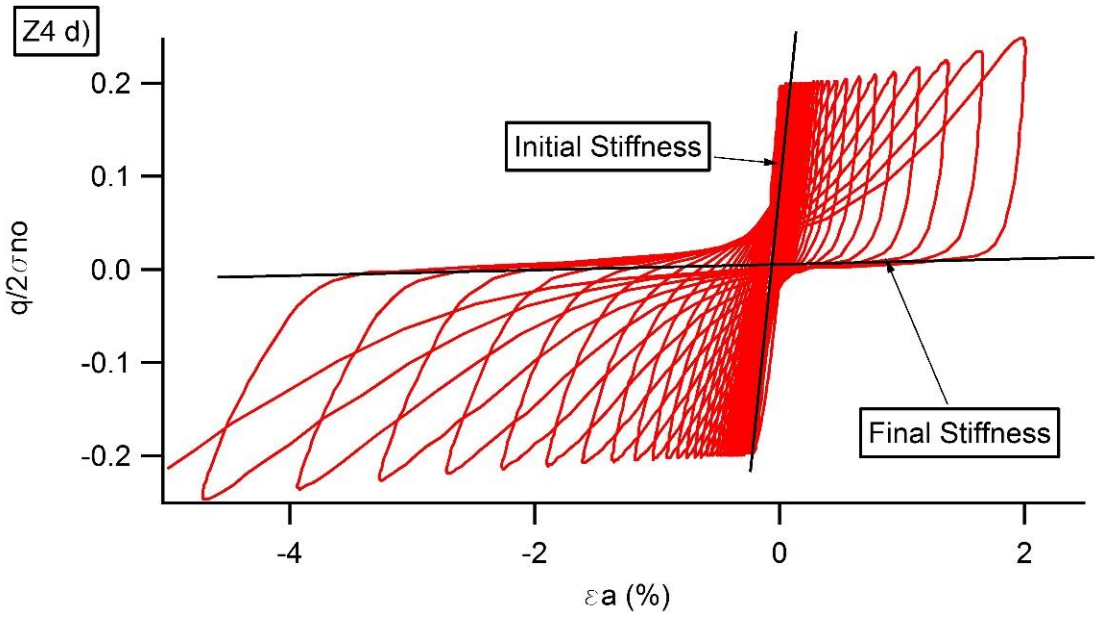

Figure 4.6a – Stiffness change visualization for liquefied specimen Z4.

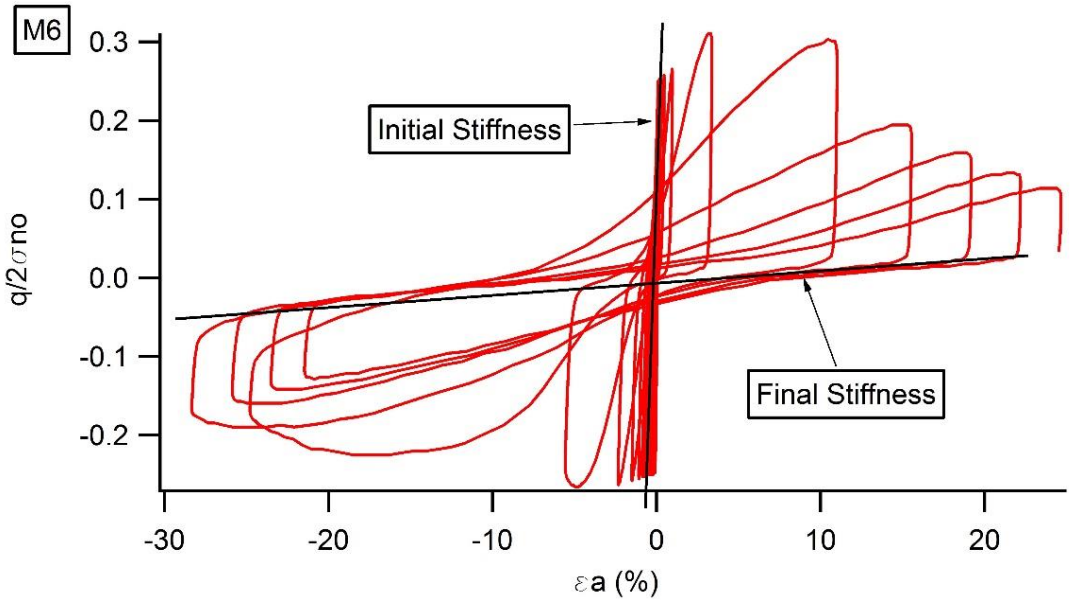

Figure 4.6b – Stiffness change visualization for liquefied specimen M6

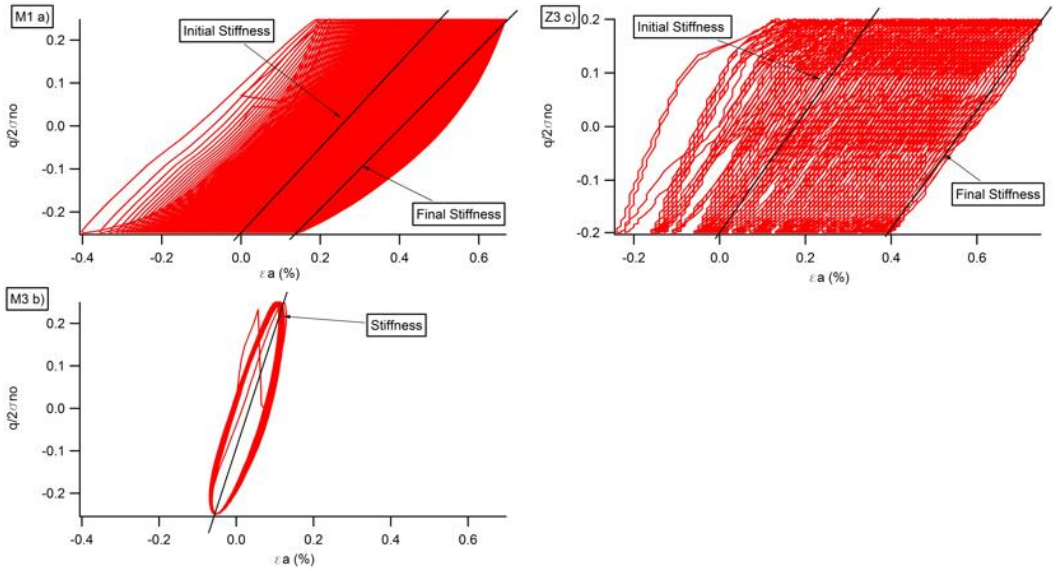

Figure 4.7 – Examples of specimens with small stiffness change

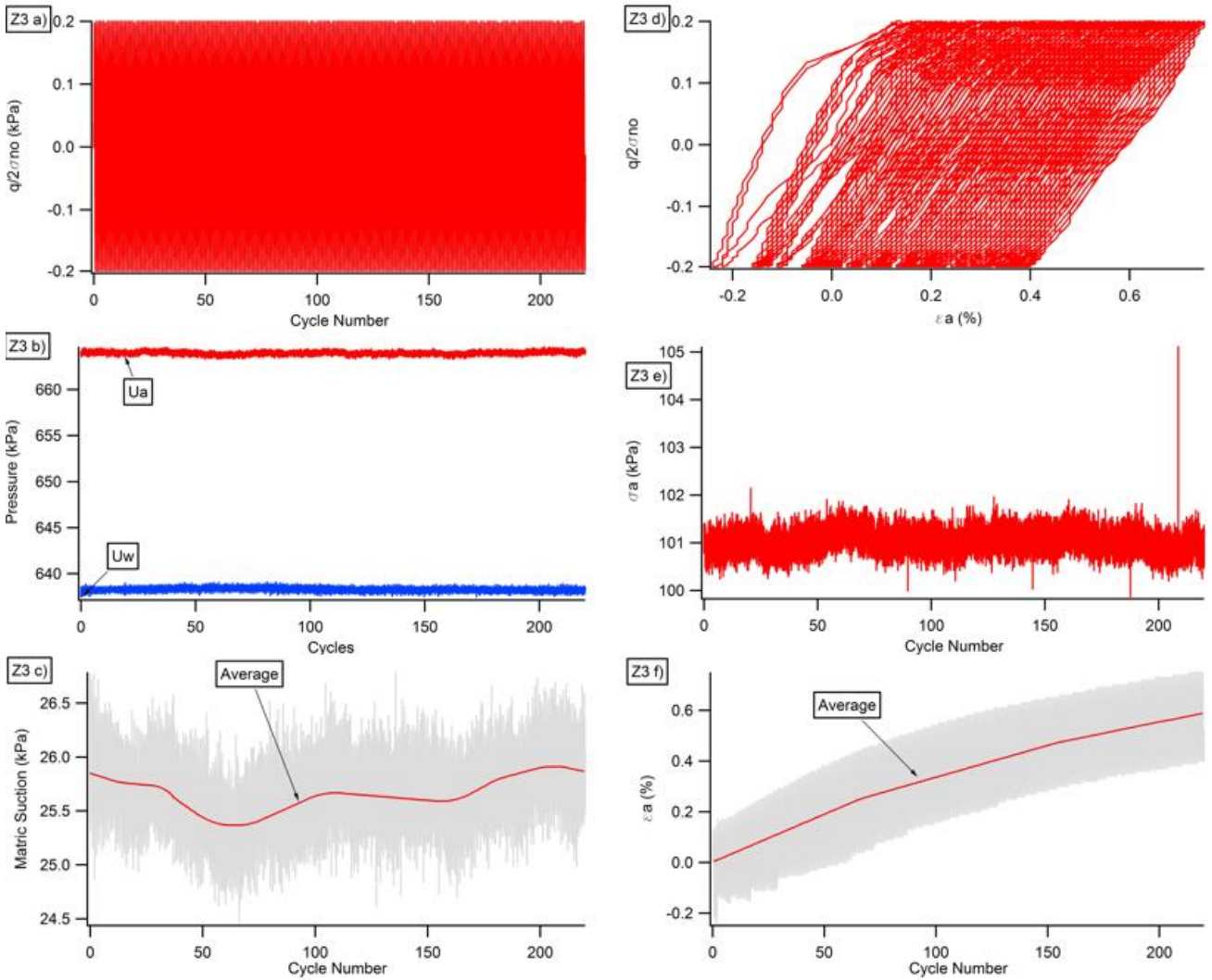

Figure 4.8 – The stress-strain & pore pressure behavior of Z3

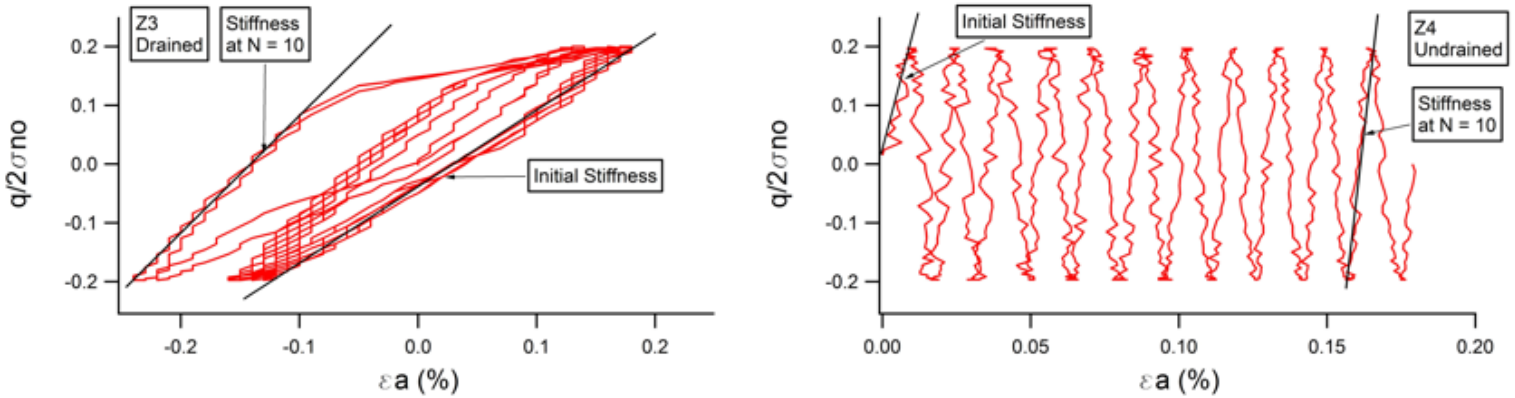

Figure 4.9 – The stress-strain behavior for the first 10 cycles of tests Z3 and Z4

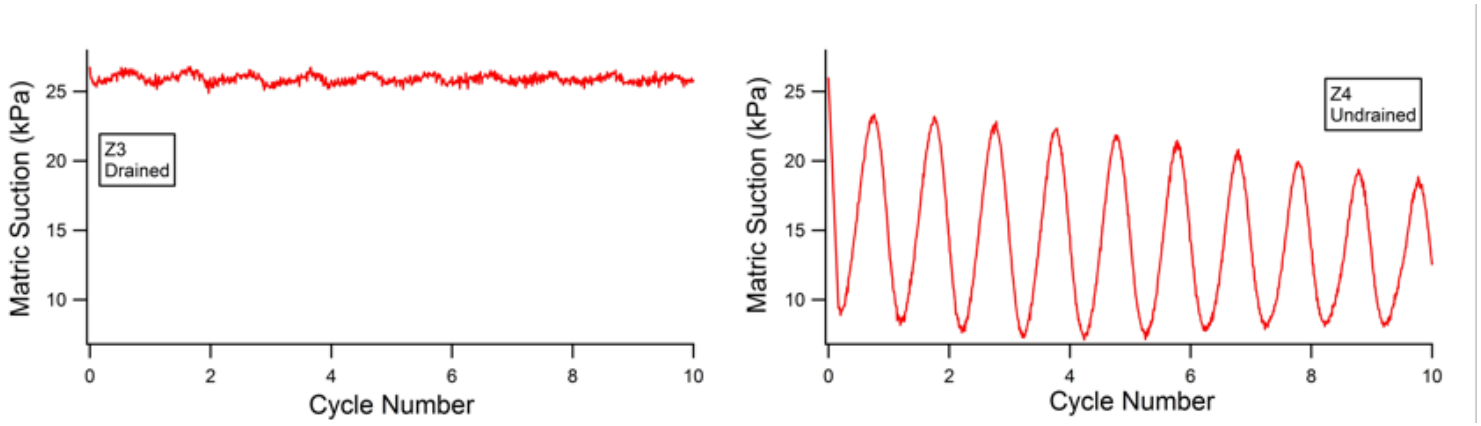

Figure 4.10 – The variation of matric suction in the first 10 cycles of tests Z3 and Z4

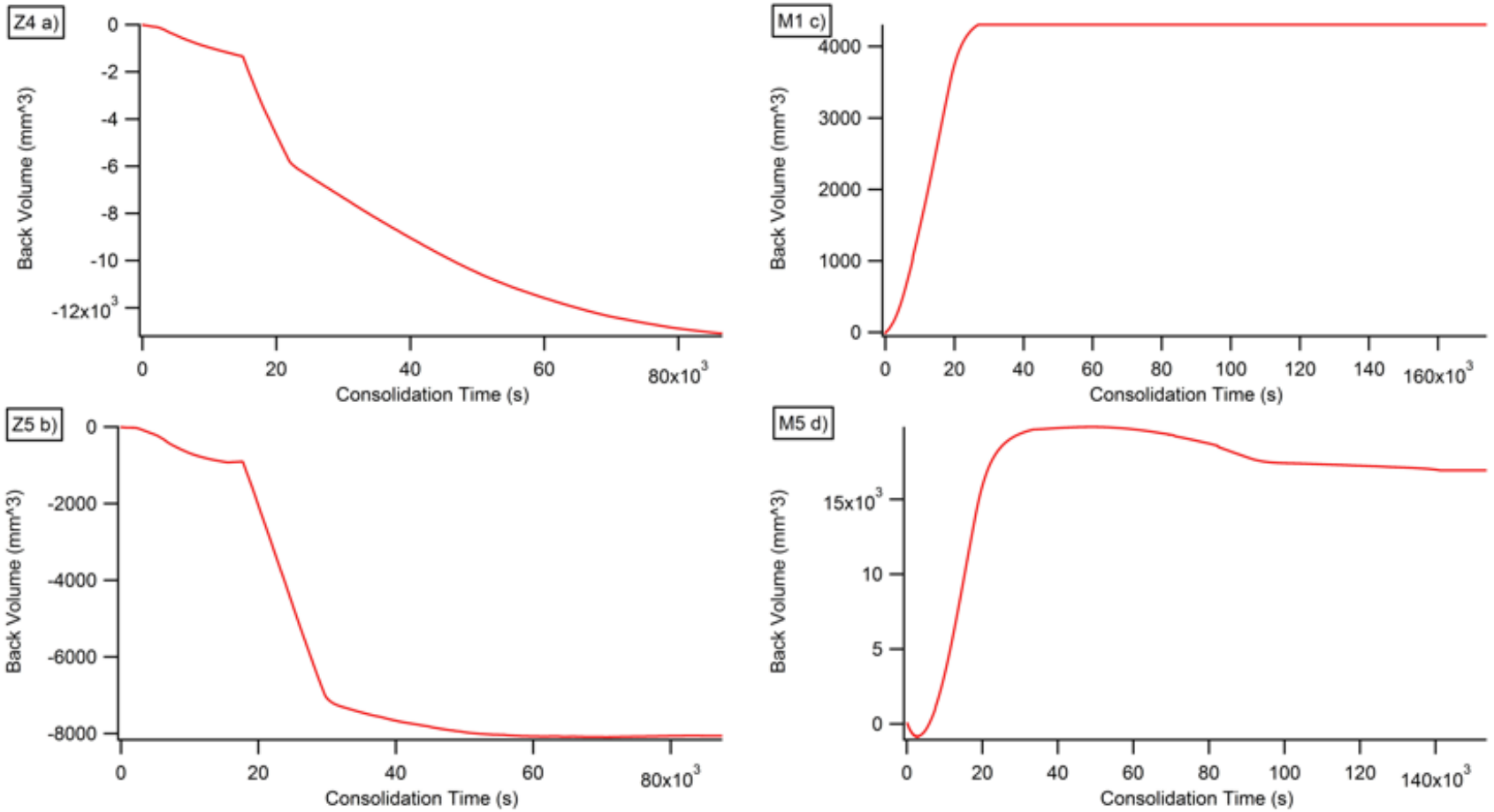

Figure 4.11 – Comparison of back volume change during consolidation for wetting and drying specimens. a) Drying path, b) Drying path, c) Wetting path, d) Wetting path.

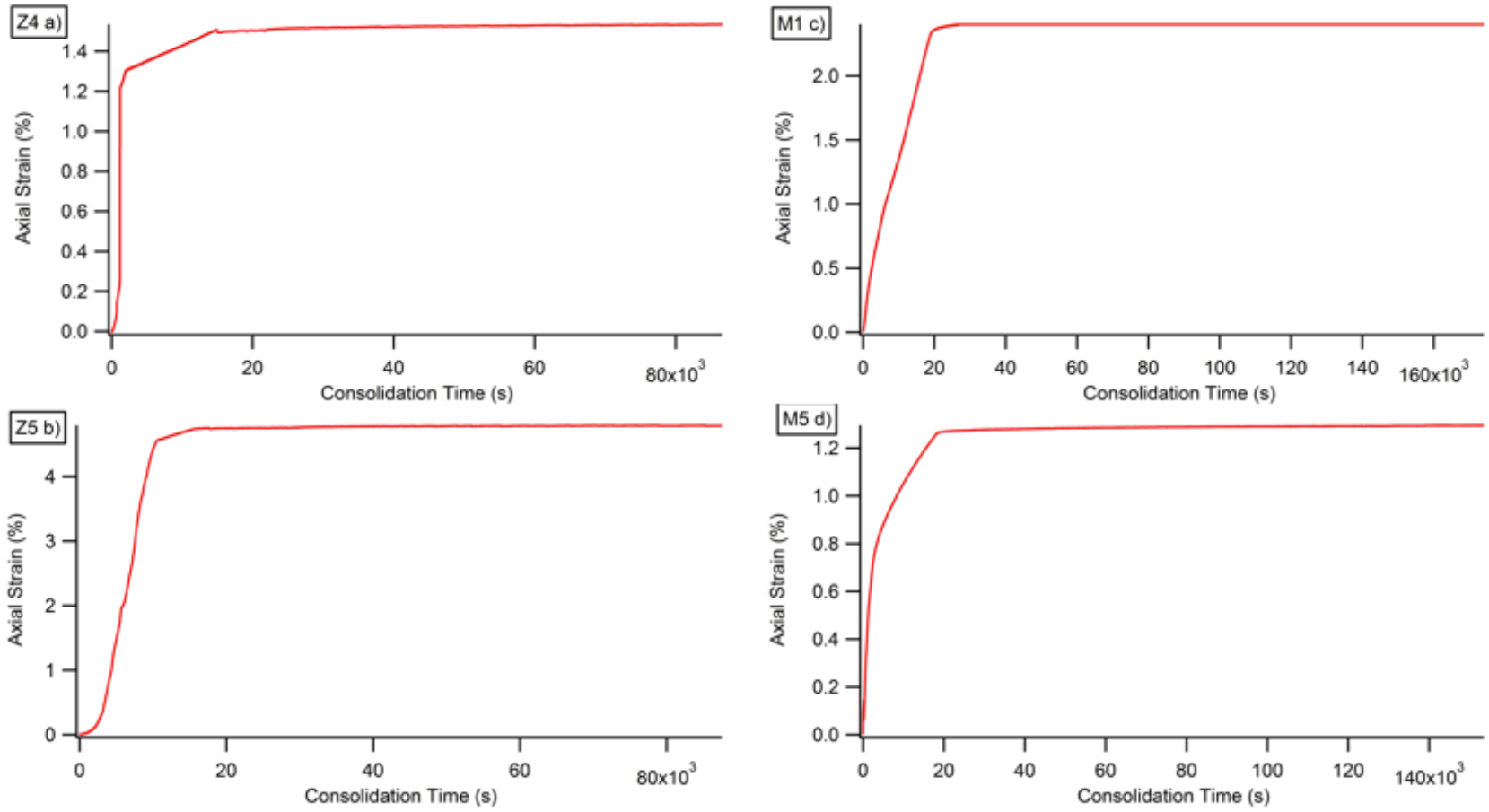

Figure 4.12 – Comparison of axial strain during consolidation for wetting and drying specimens

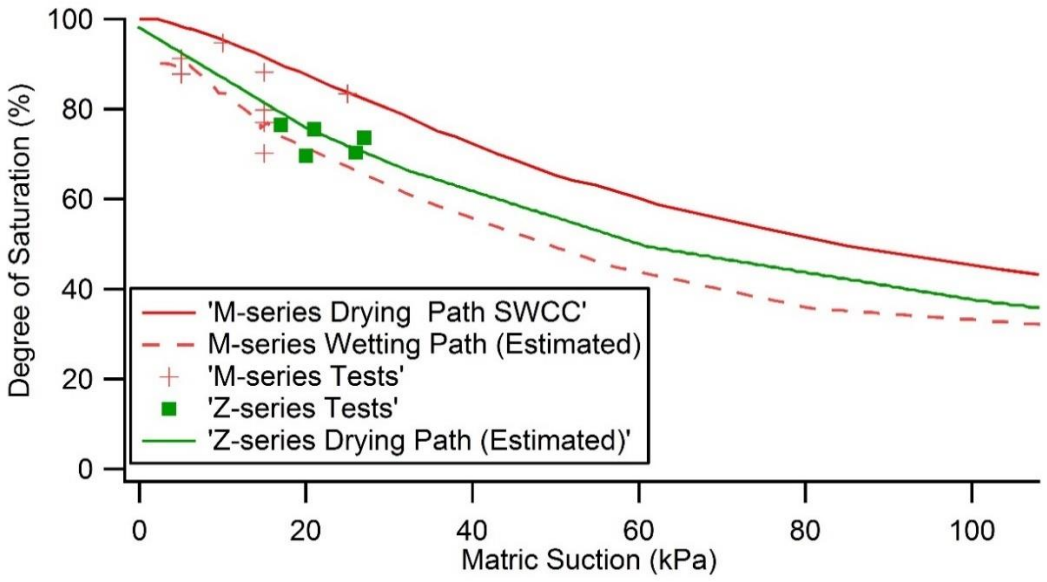

Figure 4.13 – Plot of specimen degree of saturation in relation to the soil wetting and drying SWCCs.

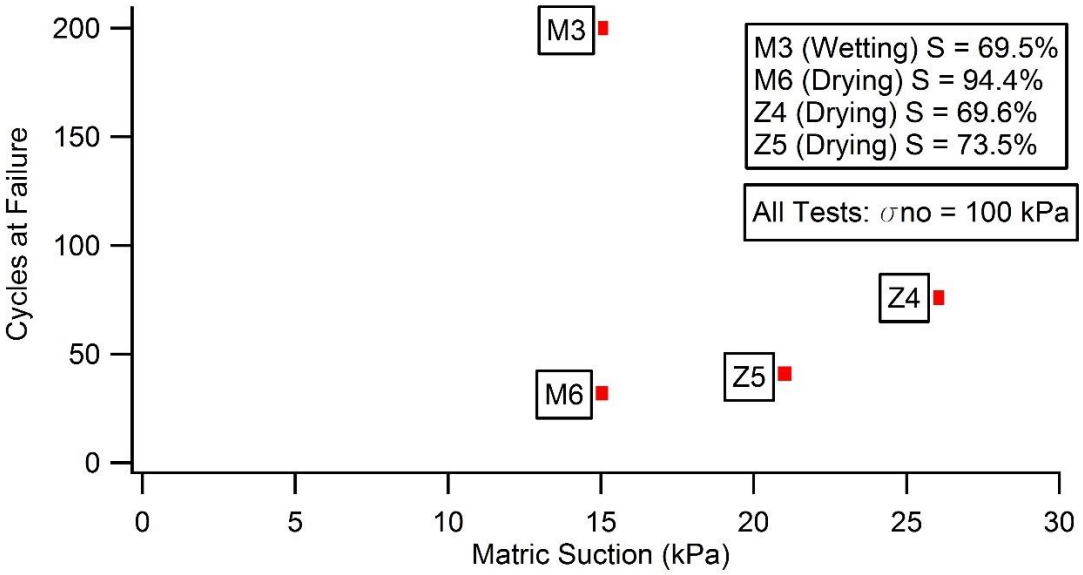

Figure 4.14 – Comparison of applied matric suction and cycles at failure for wetting and drying specimens.

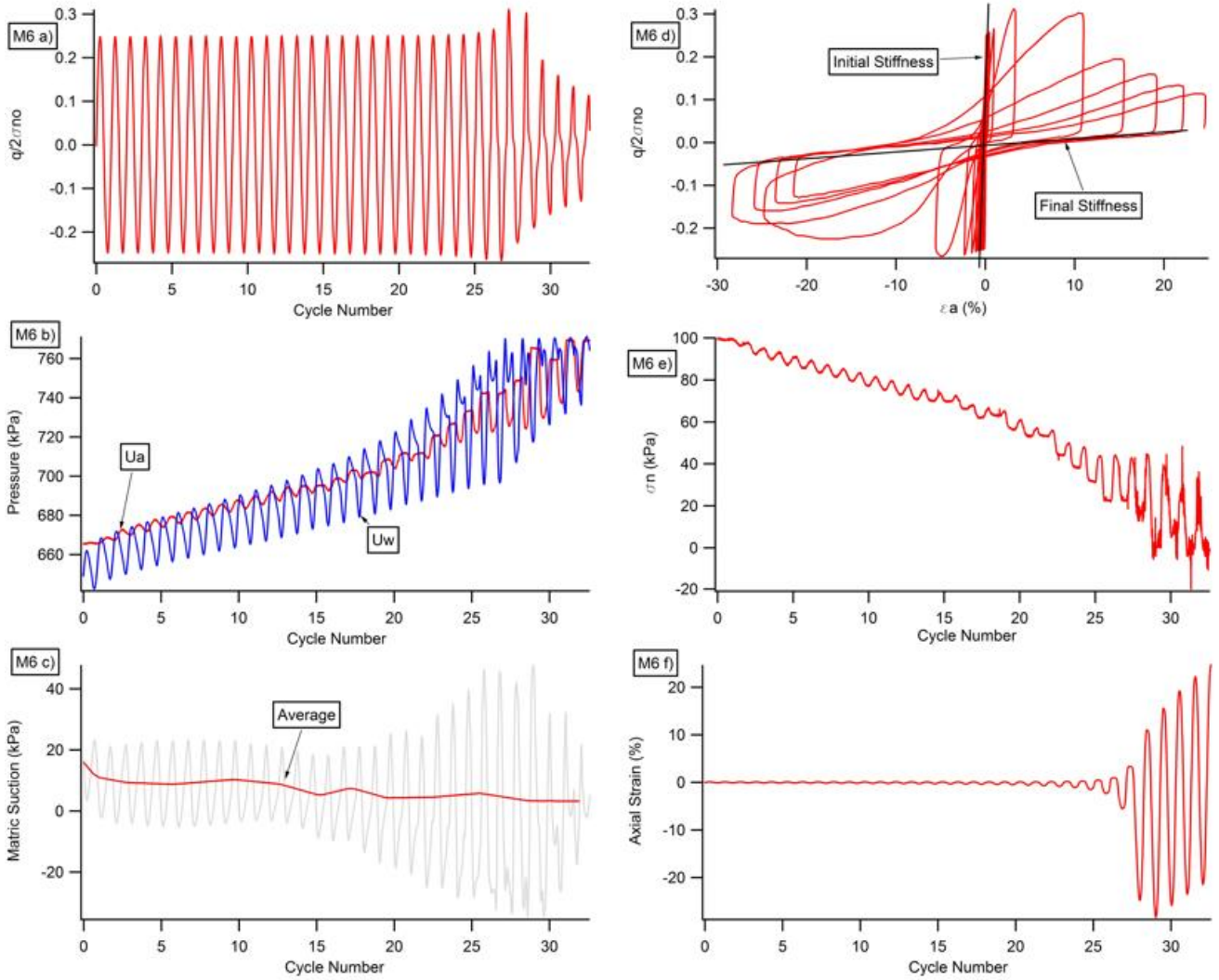

Figure 4.15 – The stress-strain & pore pressure behavior of M6

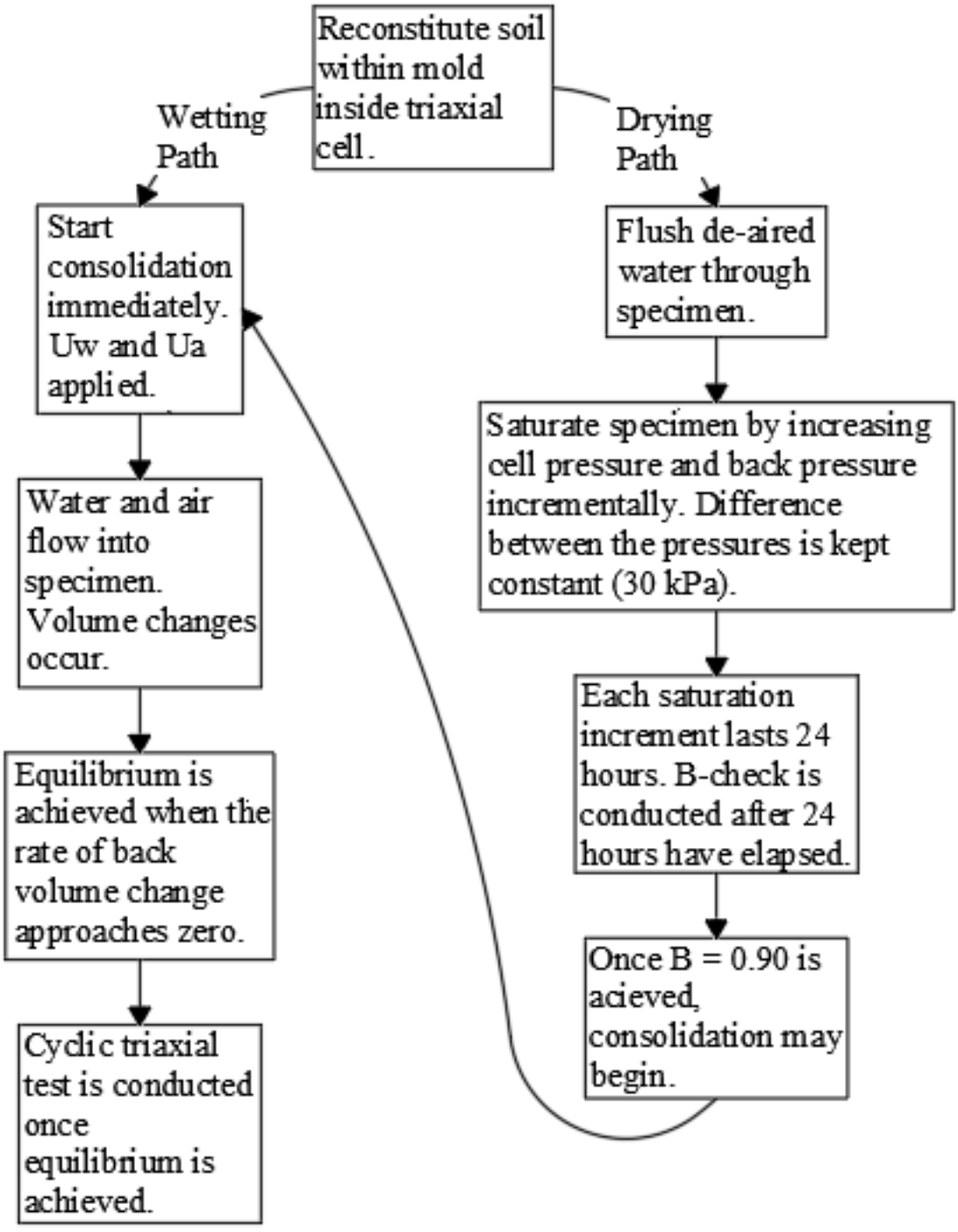

Figure 4.16 – Wetting and drying steps

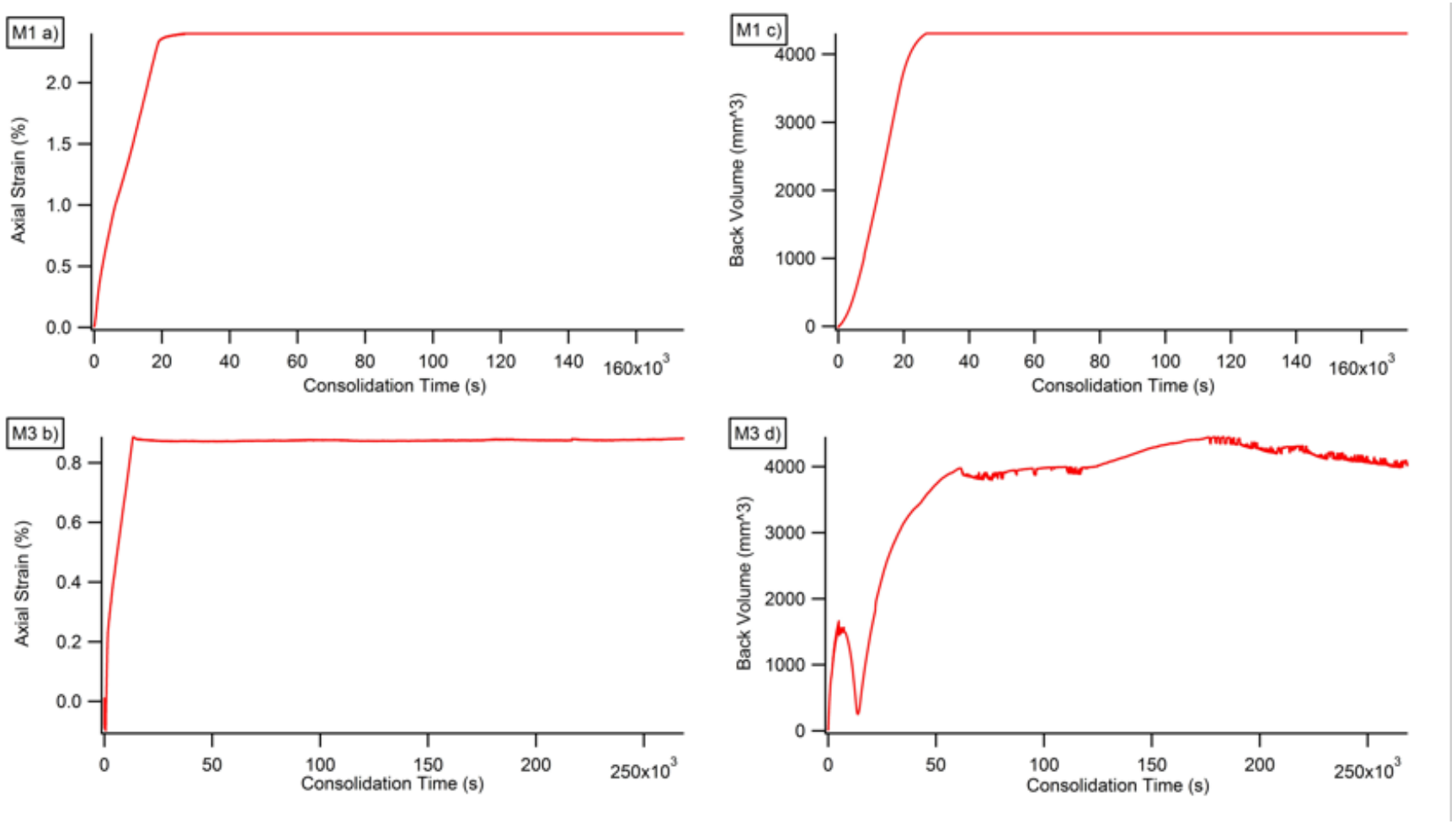

Figure 4.17 – Comparison of axial strain and back volume change during consolidation for specimens M1 and M3.

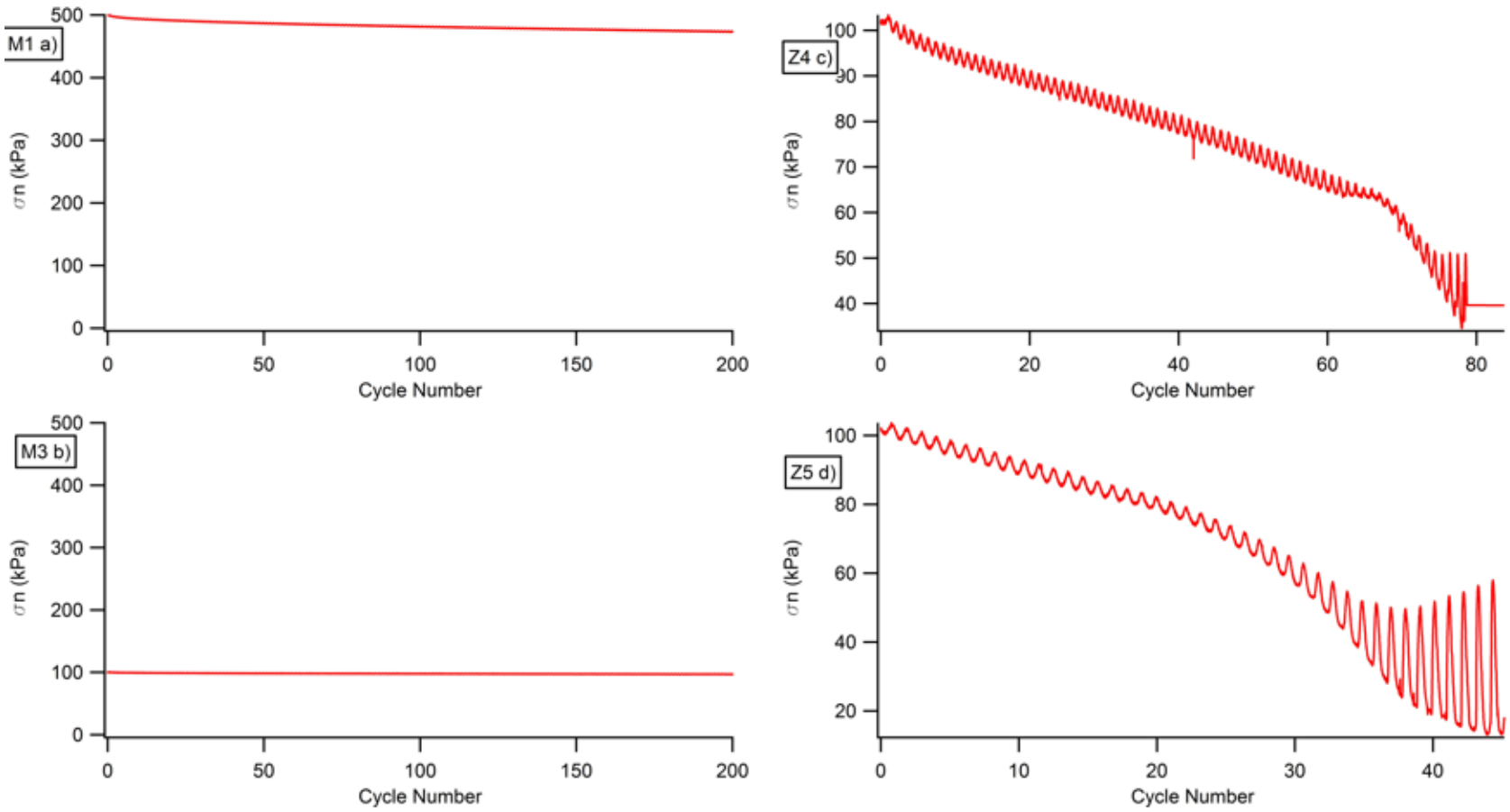

Figure 4.18 – Examples of variation in net normal stress during cyclic triaxial tests.

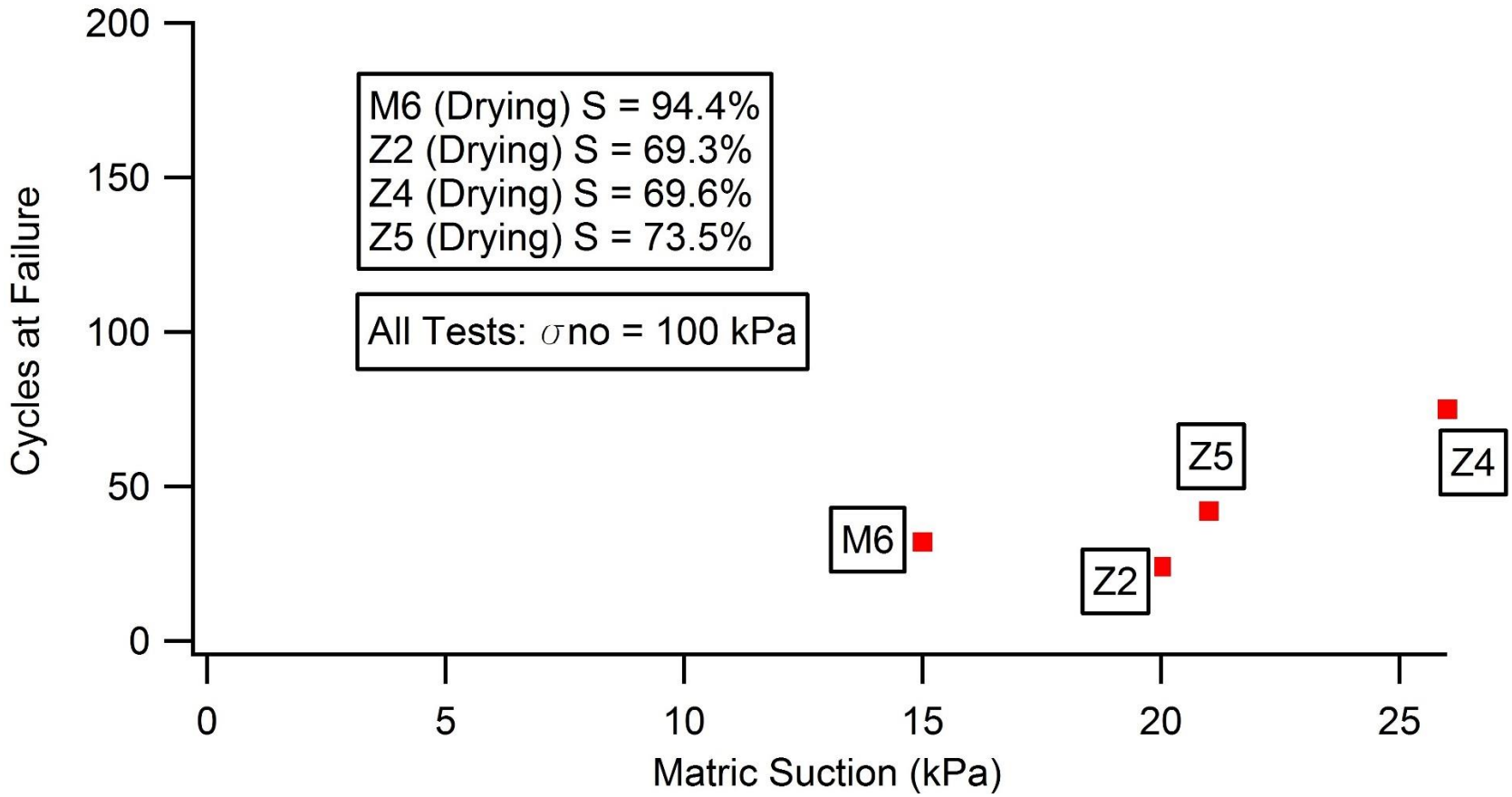

Figure 4.19 – The increase in the number of cycles to cause failure for an increase in matric suction for drying path specimens.

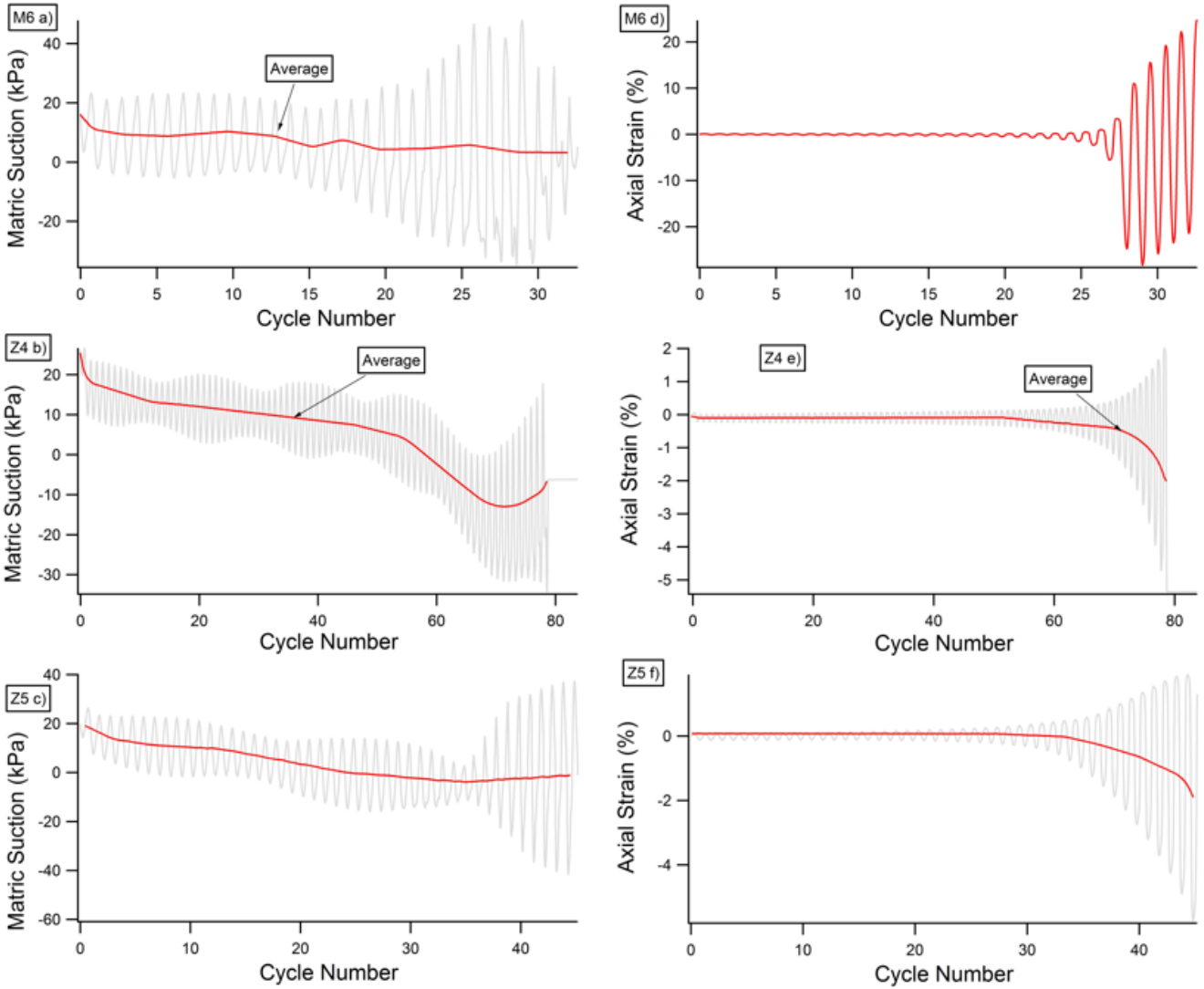

Figure 4.20 – Comparison of axial strain and matric suction for drying path specimens

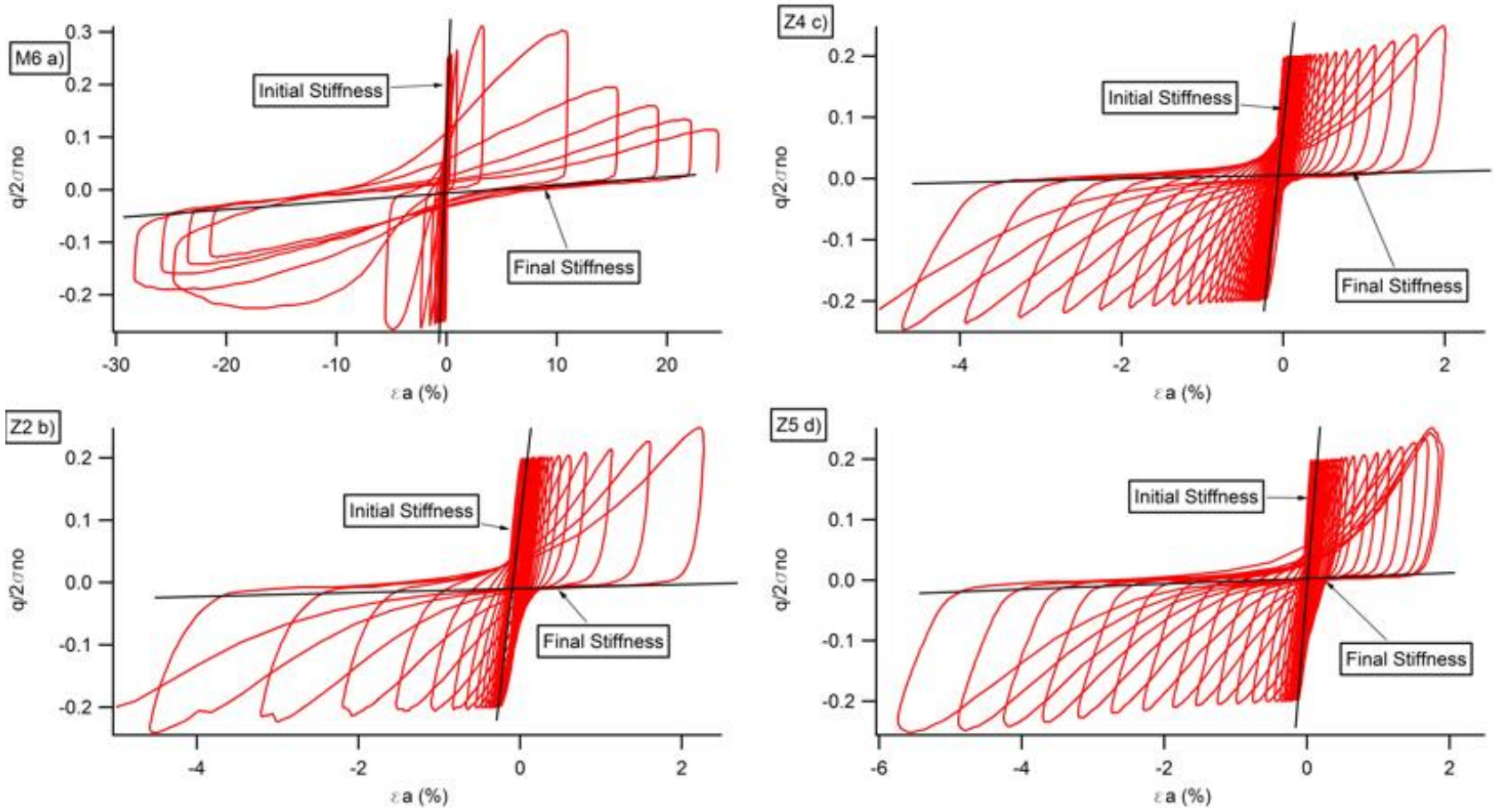

Figure 4.21 – Comparison of stiffness reduction in liquefied specimens.

CHAPTER 5

CONCLUSIONS

5.1 – Introduction

This chapter is a statement of the conclusions drawn from two series of undrained unsaturated cyclic triaxial tests that were performed on silty sand (SM) that is representative of a mine tailings material. The two series studied the parameters that trigger seismic liquefaction in the test soil specimens. The first and second series were designated the "M-series" and the "Z-series," respectively. The M-series consisted of eight tests that focused on the effects of the wetting and drying path specimen preparation techniques. This test series also varied initial net normal stress (σ_{no}), initial matric suction (ψ_o), and cyclic stress ratio (CSR). The Z-series consisted of five tests that focused on the variation of ψ_o while keeping all other parameters constant. The dry density at the end of consolidation (ρ_{dry}) for each test specimen varied slightly.

5.2 - Findings

5.2.1 – General Behavior

All specimens that experienced liquefaction had a significant reduction in net normal stress (σ_n) and matric suction (ψ) throughout their respective tests. All specimens in the Z-series liquefied with the exception of Z3 which was conducted as a drained test. As specimens approached the failure criterion of double amplitude axial strain (DA_ε) of

5%, the stiffness of the specimens decreased to near zero. This reduction in stiffness was interpreted as the onset of liquefaction. In specimens that did not fail, it was found that the initial net normal stress (σ_{no}) and initial degree of saturation (S_o) had more effect on the specimen resilience than initial matric suction (ψ_o). The non-failed specimens followed a clear load-unload loop and a near-constant stiffness. Specimens prepared using the wetting path were found to be more resilient than specimens prepared using the drying path method, and reasons for this behavior are described in section 5.2.2.

5.2.2 – Path Effects

Differences in specimen preparation procedures for the wetting and drying paths are described in detail. The S_o needs to be accounted for in a comparison between wetting and drying tests as specimens prepared using the drying path tend to have a higher degree of saturation than those prepared using the wetting path. The difference in S_o between wetting and drying specimens is due to the "ink-bottle effect," as proposed by Hillel (1980). Specimens prepared using the wetting path method experienced higher stiffness and cyclic resistance compared to specimens prepared using the drying path method. This behavior is likely due to an increase in preconsolidation pressure (σ_p') as found by Khosravi et al. (2016); however, the specimens tested in that study were dried out and then rewetted to measure the specimen stiffness. In this study, the wetting tests were conducted during the initial wetting phase. Further research needs to be completed to compare the specimen stiffness during the initial and subsequent wetting cycles.

A direct comparison between a wetting test (M3) and a drying test (M6) exemplifies these phenomena as these two tests were identical other than the difference in consolidation path. Specimen M3 maintained its initial stiffness and a relatively constant $\sigma_{n,}$ while

specimen M6 experienced a reduction in stiffness to near zero and a complete loss of σ_n. Specimen M3 withstood 200 cycles without failing, while specimen M6 failed suddenly as 32 cycles. The difference in cyclic behavior of the two specimens is attributed to specimen M6 possessing a much higher S_o than specimen M3.

The drying path soil-water characteristic curve (SWCC) was measured, while the wetting path SWCC was estimated for the M-series tests. As expected, a hysteresis exists between the drying and wetting SWCCs as the drying SWCC plots above the wetting SWCC on a plot of matric suction versus degree of saturation (S). Due to different dry unit weights (γ_{dry}) between the M-series and Z-series specimens, the Z-series specimens followed a different estimated drying SWCC, plotting below the drying path of the M-series as shown in Figure 4.12.

5.2.3 – Net Normal Stress Effects

The reduction in net normal stress (σ_n) proved to be the most important factor leading to the liquefaction of the failed specimens. The σ_n is essentially the effective stress of unsaturated soils as it is the effective confinement pressure. A severe reduction in the confining pressure of a non-cohesive soil specimen, such as the one used in this study, would reduce the strength and stiffness of the specimen significantly. Of the specimens with a σ_{no} of 500 kPa, only one specimen failed, while for the undrained specimens with a σ_{no} of 100 kPa, all but one specimen failed. As this confinement is reduced, the strength and stiffness of the soil specimen decrease to near zero in liquefied specimens.

A comparison is made between wetting path specimens M1 and M3, which experienced σ_{no} of 500 kPa and 100 kPa, respectively. Due to the higher σ_{no}, specimen M1 experienced a larger axial strain (ε_a) and change in the void ratio (e) than specimen M3.

Specimen M1 also developed a higher S_o than specimen M3. Even though the specimens experienced different σ_{no} values, the change in back volume, the amount of pore water that entered the specimens during consolidation, was approximately the same for both specimens.

There is a direct relation between the decrease in σ_n and the increase in DA_ε for failed specimens. For specimen Z5, the rate of DA_ε development increased significantly after 33 cycles, corresponding to an increase in the amplitude of the σ_n wave. The net normal stress reduction ratio (r_n), as utilized by the Tsukamoto et al. (2014) study, is a way to quantify the reduction in σ_n for cyclic triaxial tests. The findings of this study align with the findings of Tsukamoto et al. (2014), as specimens with higher relative densities experience a higher reduction in σ_n compared to those with lower relative densities. In a comparison of specimens Z4 and Z5, the denser specimen Z5 experienced a higher reduction in σ_n than specimen Z4, which possessed a lower density. A threshold r_n of 0.5 signaled the rapid increase in the rate of DA_ε development for specimens Z4 and Z5. However, the threshold r_n for specimens M6, M7, and Z2 varied, demonstrating the threshold r_n cannot be predicted before the cyclic triaxial test is conducted.

5.2.4 – Matric Suction Effects

In a comparison of three specimens with the same σ_{no}, prepared using the drying path, and exposed to a CSR of 0.20, a trend was found that showed as the initial matric suction (ψ_o) increased, the number of cycles at failure also increased as supported by Tsukamoto et al. (2014). Even though the matric suction values utilized in this study are relatively small compared to the study conducted by Alonso et al. (1990), suction hardening is present in the specimens, as seen in a comparison between Z4 and Z5. Specimen Z4

experiences a more rapid change in axial strain before failure, while the development of axial strain in specimen Z5 is more gradual. Essentially, a specimen with a higher ψ_o will experience a more brittle failure compared to a specimen with a lower ψ_o even though the difference in axial strain development rate is very small at the matric suction ranges tested in this study.

Similar specimens consolidated using different ψ_o values will have significantly different stiffnesses, as supported by Ghayoomi et al. (2017). With an increase in ψ_o of 11 kPa between specimens M6 and Z4, the stiffness of specimen Z4 was over one order of magnitude greater than specimen M6. Specimens M6, Z2, Z4, and Z5, show the stiffness of unsaturated soil specimens increases significantly with an increase in initial matric suction.

5.3 – Field Applications of the Research

The slope stability of mine tailings embankments is a particular concern, as slope failures in these structures can lead to catastrophic loss of life (Nogueira & Plumb, 2020). The findings from this study can be applied to slope stability analyses of mine tailings embankments located in seismically active regions that experience wetting and drying cycles. This study, as well as the study by Fredlund and Xing (1994), has shown soils exposed to an equal matric suction along the wetting and drying paths will have significantly different degrees of saturation (S). Specimens prepared using the wetting path possessed significantly higher cyclic resistance compared to those prepared using the drying path. If a tailings embankment was recently constructed and had yet to experience a wetting and drying cycle, the significant difference in cyclic resistance between wetting and drying path specimens could be crucial to the analysis of the liquefaction potential of

the stored tailings as a part of the overall slope stability analysis. To be conservative, a geotechnical engineer may conduct an unsaturated cyclic triaxial test on a specimen prepared using the drying path and use the cyclic resistance of the specimen to determine the cyclic resistance ratio (CRR) for use in a liquefaction analysis of the tailings material.

In a natural, horizontal soil profile with a groundwater table (GWT) present, the unsaturated soils immediately above the GWT can experience matric suction values similar to the ones utilized in this study. A rain event can raise the GWT of the soil profile, increasing the (S) of the formerly unsaturated soils without causing full saturation, reducing the matric suction present in these soils. This study shows the reduction in cyclic resistance due to the reduced matric suction would increase the probability of liquefaction of the soils during an earthquake. A foundation engineer tasked with designing a building foundation on the soil profile in question should assess the liquefaction potential of the unsaturated soil immediately above the GWT and consider how changes in the GWT depth can affect the matric suction and cyclic resistance of the soil.

During a rain event, formerly dry soil with no matric suction above the GWT can be wetted by the rise of the GWT without becoming fully saturated. After the rain event ends and the GWT falls to its original depth, the cyclic resistance of the soil will have reduced significantly. For this reason, a foundation engineer designing a building foundation in the soil profile in question should consider the reduction in cyclic resistance between the wetting and drying path in a liquefaction analysis of the soils near the GWT.

Mine tailings stored at significant depths within unsaturated tailings embankments experience high net normal stress (σ_n) compared to tailings located at shallower depths. This study has shown specimens consolidated with σ_n of 500 kPa demonstrated

significantly higher cyclic resistance compared to those consolidated with σ_n of 100 kPa. A geotechnical engineer tasked with assessing the seismic slope stability of a tailings embankment can use this finding to select the depths of interest and corresponding stress states to conduct unsaturated cyclic triaxial tests to assess the liquefaction potential of the tailings material. Unsaturated cyclic triaxial tests are expensive to conduct and the ability to select a few representative stress states will allow the engineer to keep the subsurface exploration cost within the desired budget.

5.4 – Recommendations for Future Work

5.4.1 – Investigation of Late Stage CSR Values in Cyclic Triaxial Device

A study that attempts to answer why the cyclic stress ratio (CSR) increased in the last several cycles of the Z-series tests while decreasing in the last several cycles of the M-series would provide a greater understanding of the unsaturated soil failure mode.

5.4.2 – Study of Higher Initial Matric Suction Values to Find the Preconsolidation Stress

Research that studies the behavior of the silty sand material for matric suctions greater than 30 kPa. This study could measure the preconsolidation stress (σ_p') at different degrees of saturation in an effort to confirm the findings of Khosravi et al. (2016), which used a matric suction range of 0 to 71 kPa.

5.4.3 – Investigation of the Poisson's Ratio of Unsaturated Silty Sand Representative of Tailings Material

A study to determine an accurate Poisson's ratio for the unsaturated silty sand. This research study could develop an empirical correlation relating soil type, dry density, and degree of saturation to the Poisson's ratio. A comparison can also be done between natural silty sand and the artificial silty sand used in this study.

5.4.4 – Modification of the Current Triaxial Device for Volume Change Measurements

A study can assess the feasibility of a modification to the cyclic triaxial device in the University of South Carolina Geotechnical Engineering Lab to directly measure the change in sample volume during consolidation and undrained cyclic triaxial tests. The studies conducted by Tsukamoto et al. (2014) and Sawada et al. (2006) are excellent references on how to modify the equipment for this purpose. The study could confirm or contradict the findings of this study.

5.4.5 – Development of LC and SI Yield Curves for an Artificial Silty Sand

The constitutive model proposed by Alonso et al. (1990) can be used to develop yield curves for the silty sand used in this study. Several tests can be conducted to determine the stiffness parameters required to develop the yield curves. A comparison can be made to compare the yield curve of the tailings silty sand with natural silty sand.

5.4.6 – Assessment of Strength Difference Between Initial and Subsequent Wetting Cycles

A future study could assess the difference in strength between specimens prepared using the wetting and drying paths for multiple wetting and drying cycles. This study could determine if the difference in strength between the wetting and drying specimens is only significant during the first wetting and drying cycle.

REFERENCES

Allam, M. M., & Sridharan, A. (1981). Effect of Wetting and Drying on Shear Strength. *Journal of the Geotechnical Engineering Division, 107*(4), pp.421-438. http://dx.doi.org/10.1061/ajgeb6.0001117

Alonso, E. E., Gens, A., & Josa, A. (1990). A constitutive model for partially saturated soils. *Géotechnique, 40*(3), pp.405-430. http://dx.doi.org/10.1680/geot.1990.40.3.405

Bishop, A. W. (1959). The principle of effective stress. *Tek. Ukeblad,* 106(39), pp.859–863.

Dobry, R., & Alvarez, L. (1967). Seismic Failures of Chilean Tailings Dams. *Journal of the Soil Mechanics and Foundations Division, 93*(6), pp.237-260. http://dx.doi.org/10.1061/jsfeaq.0001054

Fang, H., & Gazetas, G. (1991). *Foundation engineering handbook*. New York, NY: VanNostrand Reinhold.

Fredlund, D. G., & Morgenstern, N. R. (1977). Stress State Variables for Unsaturated Soils. *Journal of the Geotechnical Engineering Division, 103*(5), pp.447-466. http://dx.doi.org/10.1061/ajgeb6.0000423

Fredlund, D., & Xing, A. (1994). Equations for the soil-water characteristic curve. *Canadian Geotechnical Journal, 31*(4), pp.521-532. http://dx.doi.org/10.1139/t94-061

Genuchten, M. T. (1980). A Closed-form Equation for Predicting the Hydraulic Conductivity of Unsaturated Soils. *Soil Science Society of America Journal, 44*(5), pp.892-898. http://dx.doi.org/10.2136/sssaj1980.03615995004400050002x

Ghayoomi, M., Suprunenko, G., & Mirshekari, M. (2017). Cyclic Triaxial Test to Measure Strain-Dependent Shear Modulus of Unsaturated Sand. *International Journal of Geomechanics, 17*(9). http://dx.doi.org/10.1061/(asce)gm.1943-5622.0000917

Guber, A. K., & Pachepsky, Y. A. (2010). *Multimodeling with Pedotransfer Functions. Documentation and User Manual for PTF Calculator* (United States of America, USDA, Environmental Microbial and Food Safety Laboratory). USDA. Retrieved December 20, 2020.

Hillel, D. (1980). *Fundamentals of soil physics*. New York etc: Academic Press.

Idriss, I. M., & Boulanger, R. W. (2008). *Soil liquefaction during earthquakes*. Oakland, CA: Earthquake Engineering Research Institute.

Khosravi, A., Salam, S., Mccartney, J. S., & Dadashi, A. (2016). Suction-Induced Hardening Effects on the Shear Modulus of Unsaturated Silt. *International Journal of Geomechanics, 16*(6). http://dx.doi.org/10.1061/(asce)gm.1943-5622.0000614

Kossoff, D., et al. “Mine Tailings Dams: Characteristics, Failure, Environmental Impacts, and Remediation.” *Applied Geochemistry*, vol. 51, Dec. 2014, pp. 229–245., https://doi.org/10.1016/j.apgeochem.2014.09.010

Yeh, H., Yeh, C., Lee, J., Lee, C., Etale, A., Mhlanga, S., . . . Mendoza-Promotor, J. A. (2016). *Groundwater: Contaminant and Resource Management*. Rijeka, Croatia: InTech.

Lu, N., Godt, J. W., & Wu, D. T. (2010). A closed-form equation for effective stress in unsaturated soil. *Water Resources Research, 46*(5). http://dx.doi.org/10.1029/2009wr008646

Lu, N., & Likos, W. J. (2006). Suction Stress Characteristic Curve for Unsaturated Soil. *Journal of Geotechnical and Geoenvironmental Engineering, 132*(2), pp.131-142. http://dx.doi.org/10.1061/(asce)1090-0241(2006)132:2(131)

Mulligan, D. R. (1996). *Environmental management in the Australian minerals and energy industry: Principles and practices*. Sydney: UNSW Press. Retrieved September 30, 2021.

Nogueira, M., & Plumb, C. (2020, January 08). Exclusive: Brazil prosecutor aims to charge Vale within days over mining waste dam disaster. Retrieved March 15, 2021, from https://www.reuters.com/article/us-vale-sa-disaster-exclusive-idUSKBN1Z72GS.

Oh, S., Lu, N., Kim, T., & Lee, Y. H. (2013). Experimental Validation of Suction Stress Characteristic Curve from Nonfailure Triaxial K0 Consolidation Tests. *Journal of*

Geotechnical and Geoenvironmental Engineering, 139(9), pp.1490-1503. http://dx.doi.org/10.1061/(asce)gt.1943-5606.0000880

Rico, M., Benito, G., Salgueiro, A., Díez-Herrero, A., & Pereira, H. (2008). Reported tailings dam failures. *Journal of Hazardous Materials, 152*(2), pp.846-852. http://dx.doi.org/10.1016/j.jhazmat.2007.07.050

Robertson, P.k., et al. "Characterization of Unsaturated Mine Waste: a Case History." *Canadian Geotechnical Journal,* vol. 54, no. 12, 2 June 2017, pp. 1752–1761., https://doi.org/10.1139/cgj-2017-0129.

Robertson, P. K., de Melo, L., Williams, D. J., & Wilson, G. W. (2019). Report of the expert panel on the technical causes of the failure of Feijão Dam I. *Commissioned by Vale*.

Rong, W., & Mccartney, J. S. (2020). Drained Seismic Compression of Unsaturated Sand. *Journal of Geotechnical and Geoenvironmental Engineering, 146*(5). http://dx.doi.org/10.1061/(asce)gt.1943-5606.0002251

Rong, W., & Mccartney, J. S. (2021). Undrained Seismic Compression of Unsaturated Sand. *Journal of Geotechnical and Geoenvironmental Engineering, 147*(1). http://dx.doi.org/10.1061/(asce)gt.1943-5606.0002420

Sarsby, R. (2000). *Environmental geotechnics*. London: Thomas Telford.

Sawada, S., Tsukamoto, Y., & Ishihara, K. (2006). Residual deformation characteristics of partially saturated sandy soils subjected to seismic excitation. *Soil Dynamics and Earthquake Engineering, 26*(2-4), 175-182. http://dx.doi.org/10.1016/j.soildyn.2004.11.024

Bishop, A. W. (1954). The Use of Pore-Pressure Coefficients in Practice. *Géotechnique, 4*(4), 148-152. http://dx.doi.org/10.1680/geot.1954.4.4.148

Troncoso, J. H. (1990). *Failure risks of abandoned tailings dams*. Lecture presented at International Symposium on Safety and Rehabilitation of Tailings Dams, International Commission on Large Dams, Paris, France. Retrieved October 5, 2021.

Tsukamoto, Y., Kawabe, S., Matsumoto, J., & Hagiwara, S. (2014). Cyclic resistance of two unsaturated silty sands against soil liquefaction. *Soils and Foundations, 54*(6), pp.1094-1103. http://dx.doi.org/10.1016/j.sandf.2014.11.005

Unno, T., Kazama, M., Uzuoka, R., & Sento, N. (2008). Liquefaction of Unsaturated Sand Considering the Pore Air Pressure and Volume Compressibility of the Soil Particle Skeleton. *Soils and Foundations, 48*(1), pp.87-99. http://.dx.doi.org/10.3208/sandf.48.87

United States, Congress, Corps of Engineers. *Engineering and Design: Bearing Capacity of Soils*, Dept. of the Army, U.S. Army Corps of Engineers, 1992.

Younger, P. L., & Wolkersdorfer, C. (2004). Mining Impacts on the Fresh Water Environment: Technical and Managerial Guidelines for Catchment Scale Management. *Mine Water and the Environment, 23*(S1), pp.2-80. http://dx.doi.org/10.1007/s10230-004-0028-0

Zhai, Q., Rahardjo, H., & Satyanaga, A. (2019). Uncertainty in the estimation of hysteresis of soil–water characteristic curve. *Environmental Geotechnics, 6*(4), pp.204-213. http://dx.doi.org/10.1680/jenge.17.00008

APPENDIX A

COMPREHENSIVE LAB TEST DATA

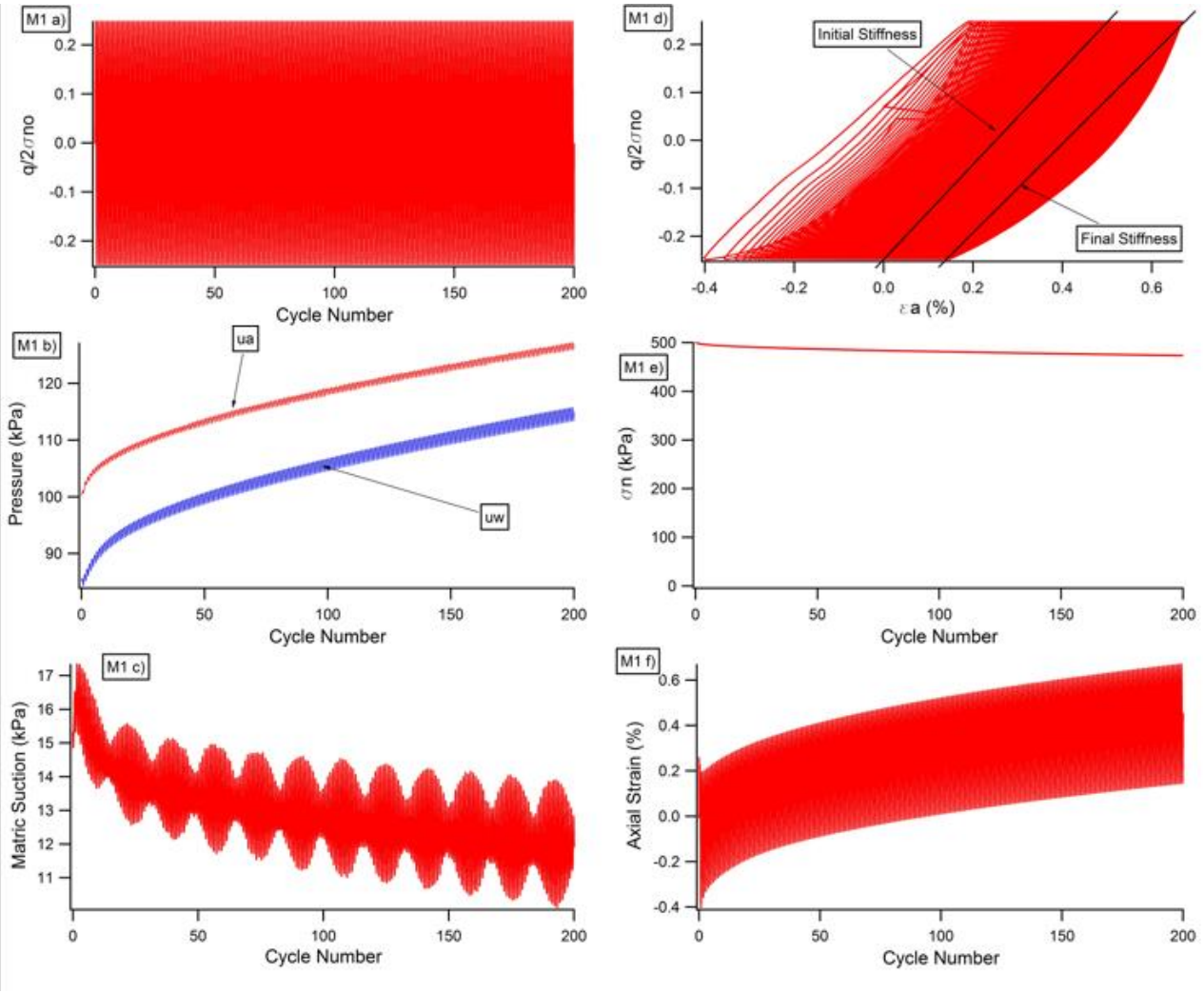

Figure A.1 – Test data for test M1

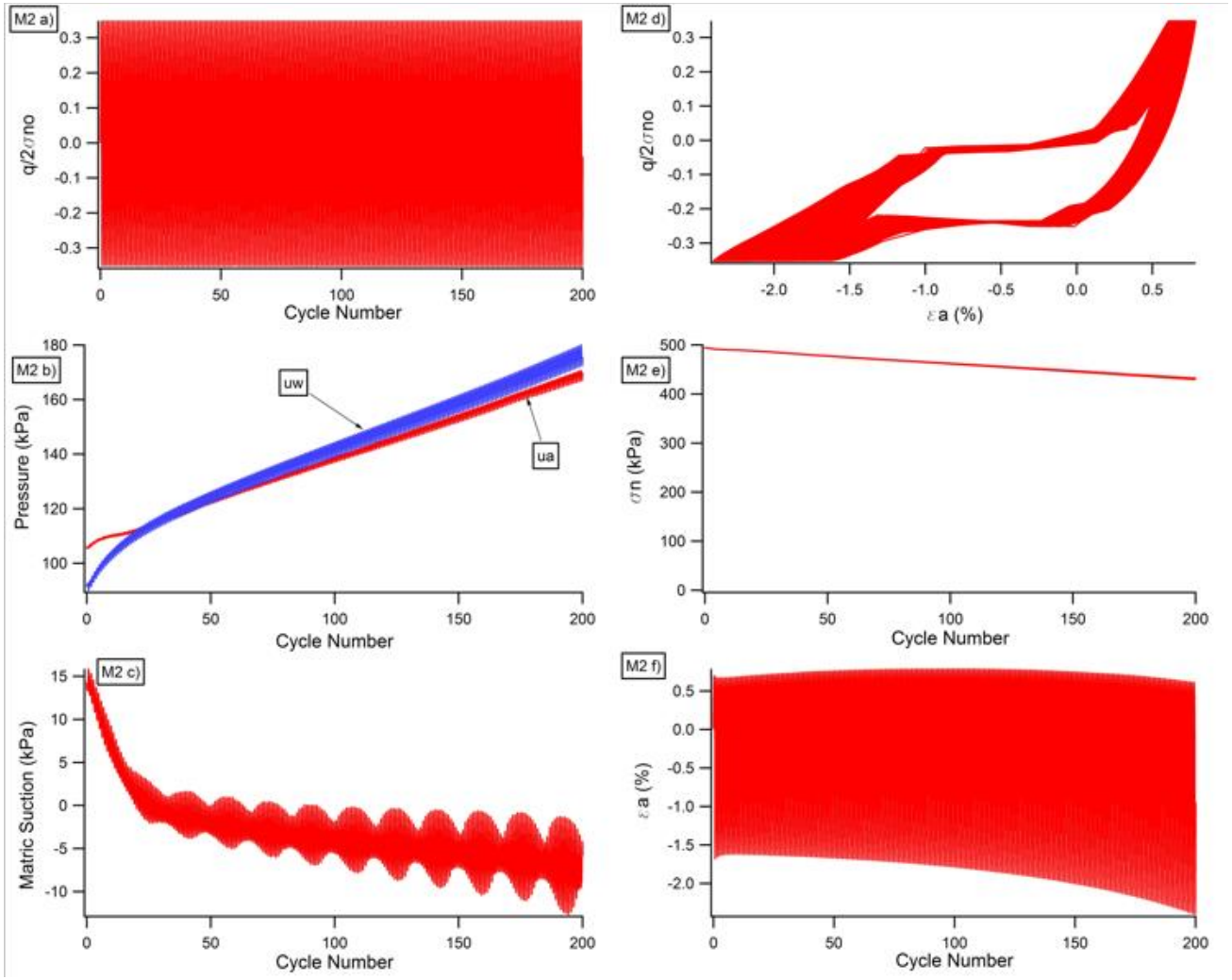

Figure A.2 – Test data for test M2

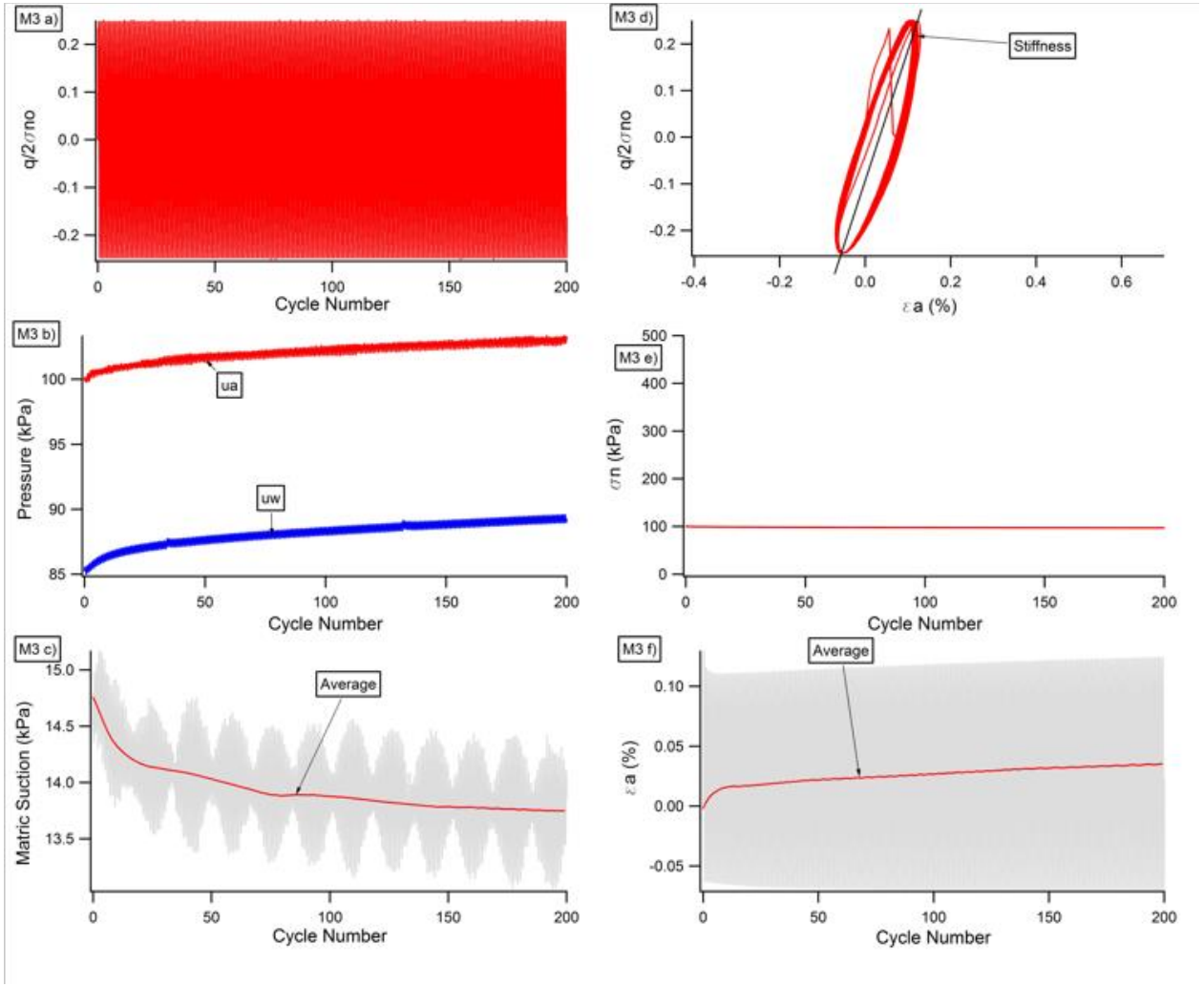

Figure A.3 – Test data for test M3

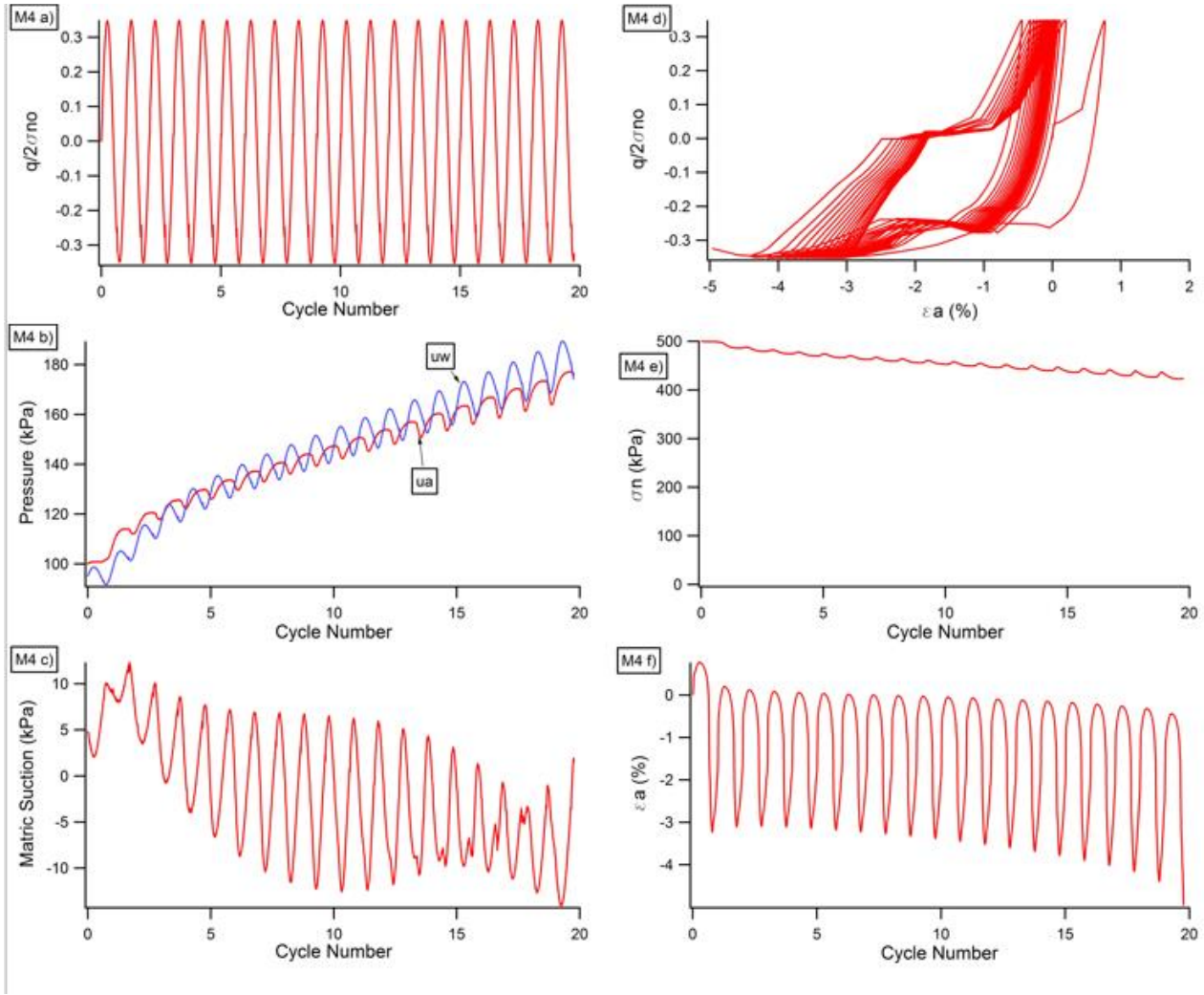

Figure A.4 – Test data for test M4

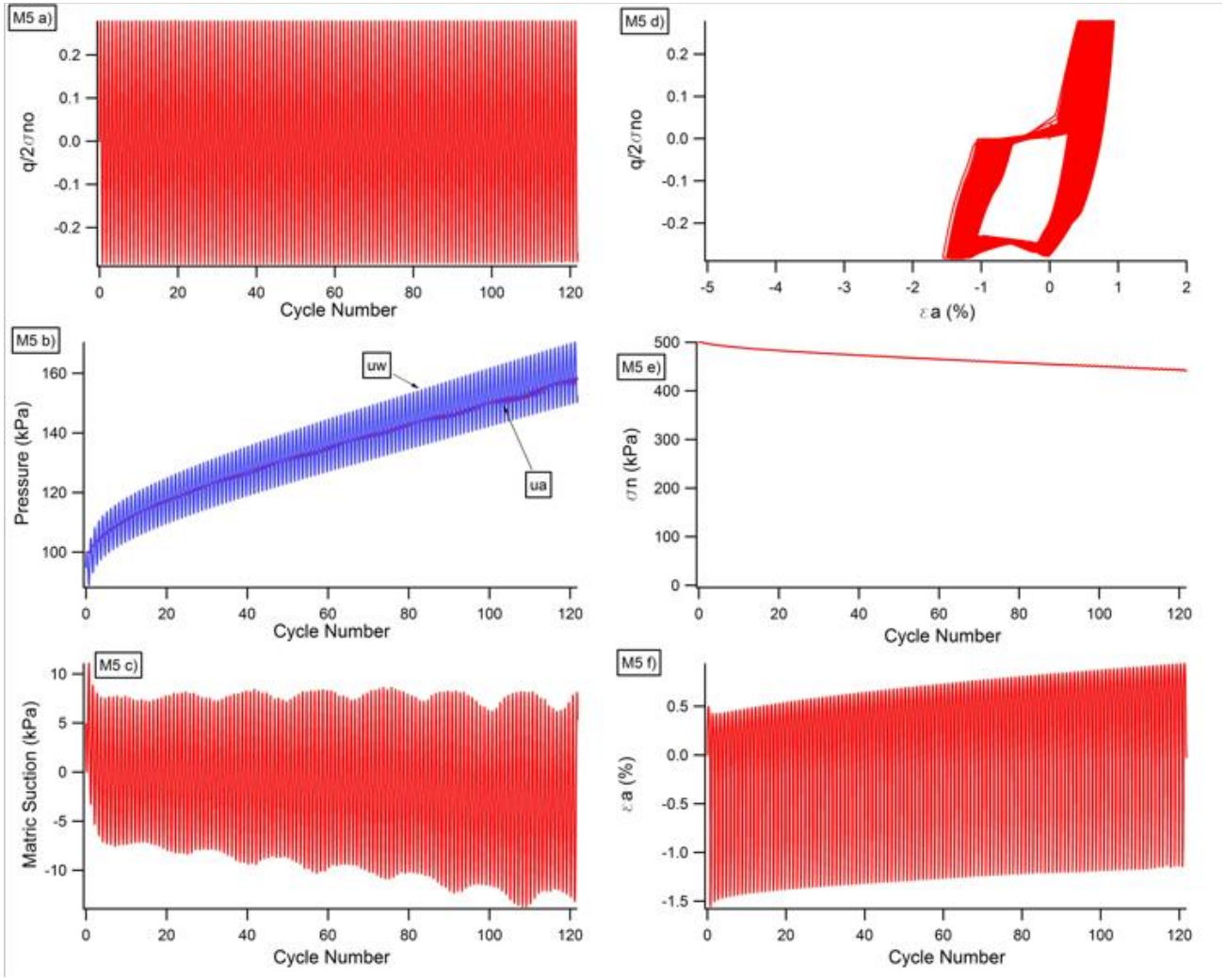

Figure A.5 – Test data for test M5

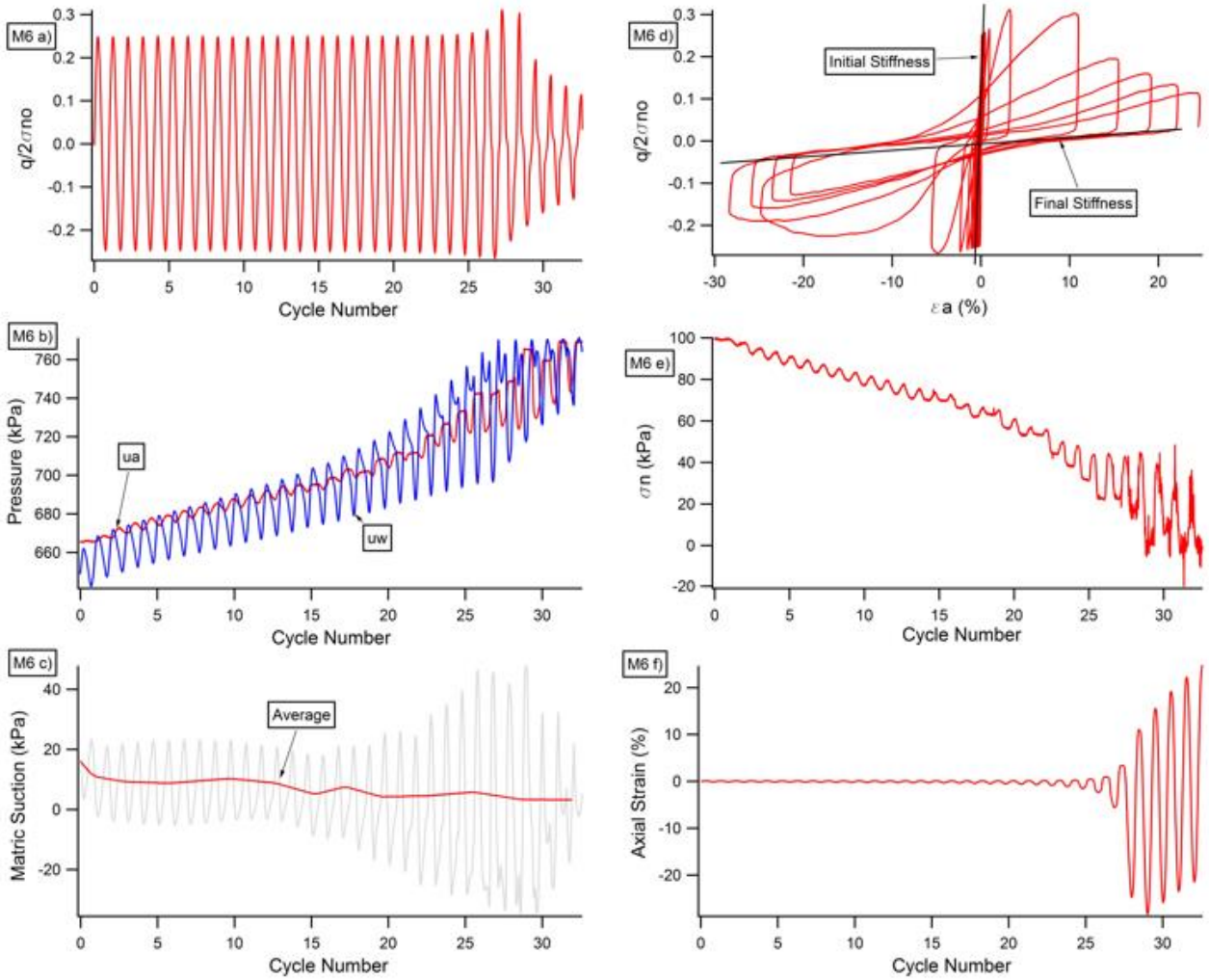

Figure A.6 – Test data for test M6

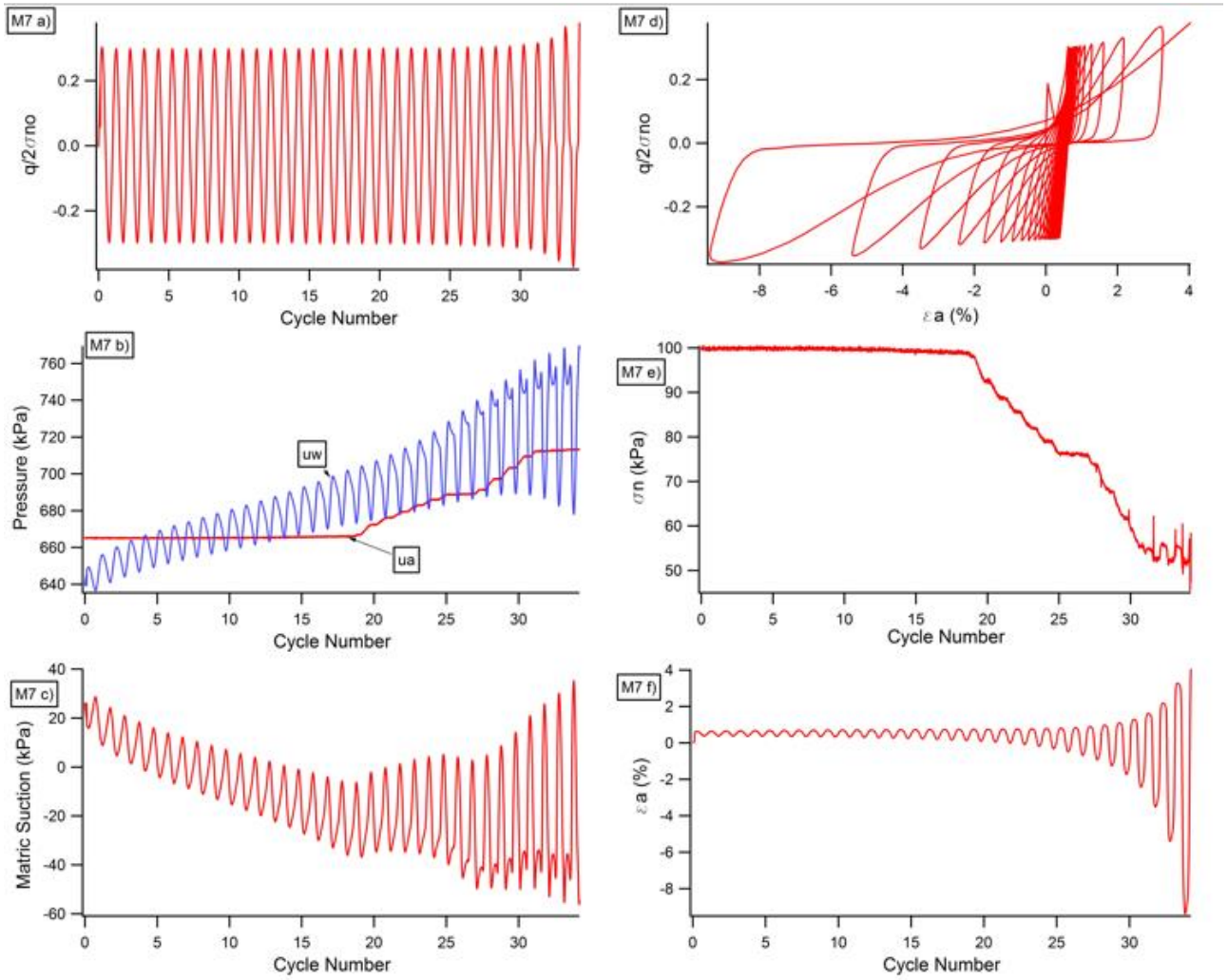

Figure A.7 – Test data for test M7

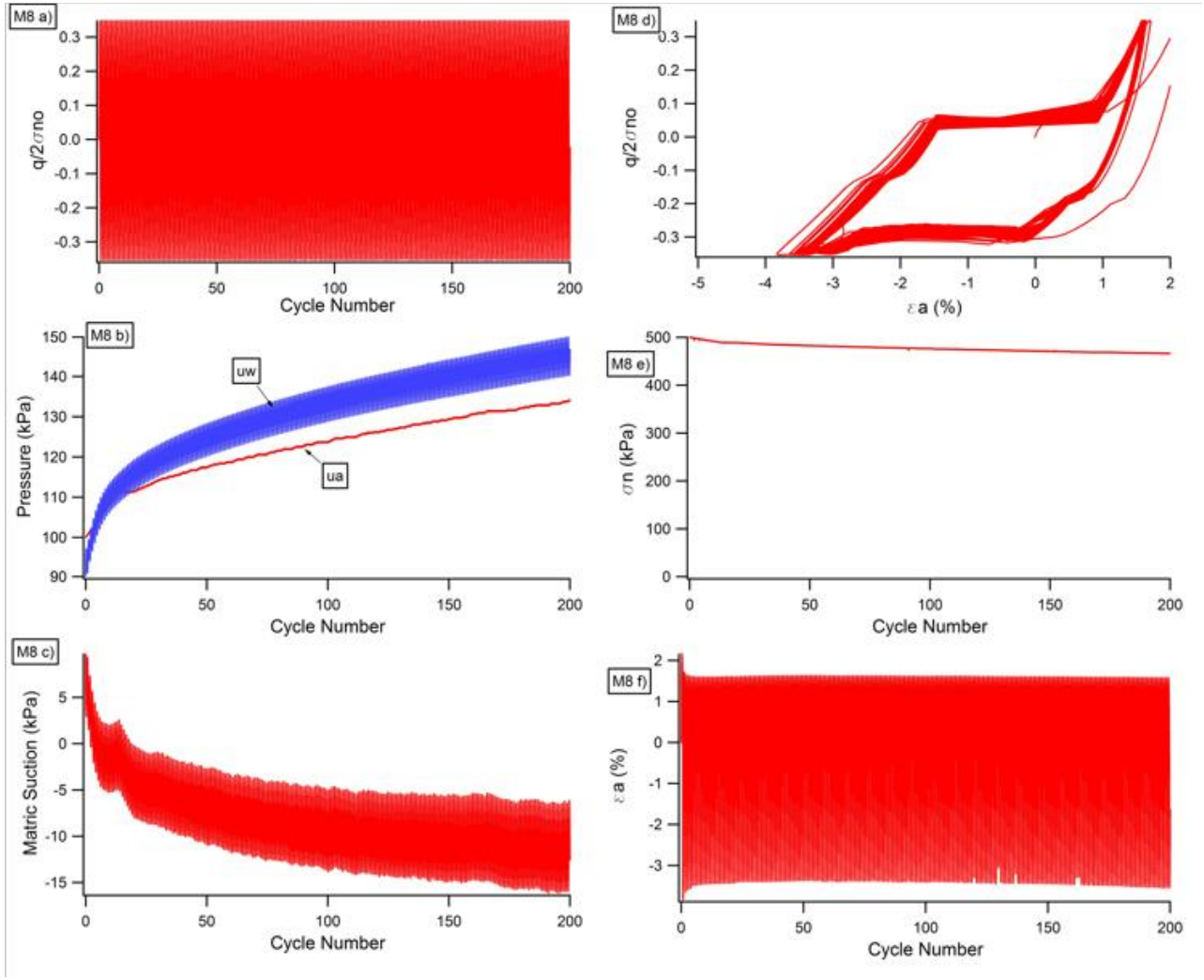

Figure A.8 – Test data for test M8

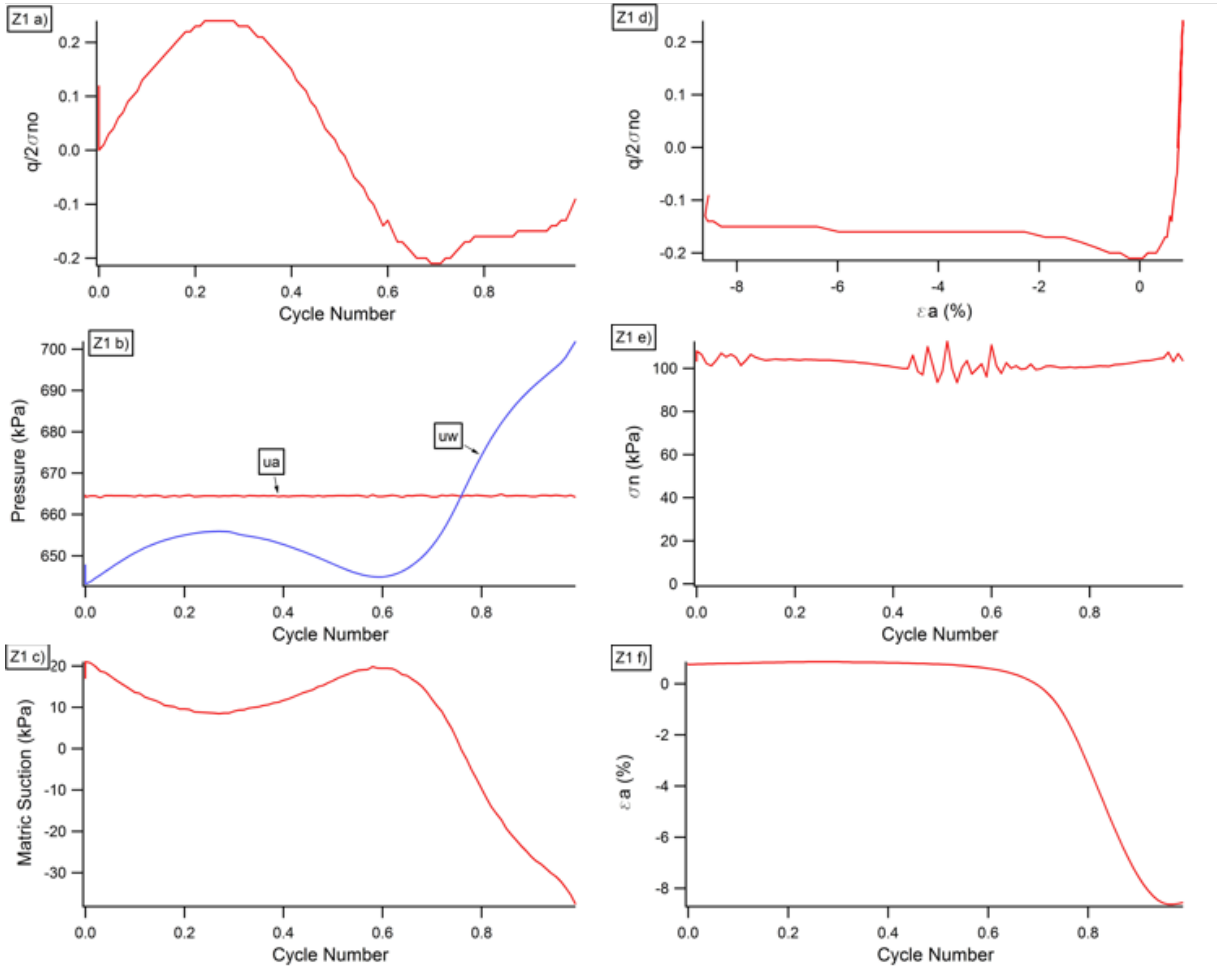

Figure A.9 – Test data for test Z1

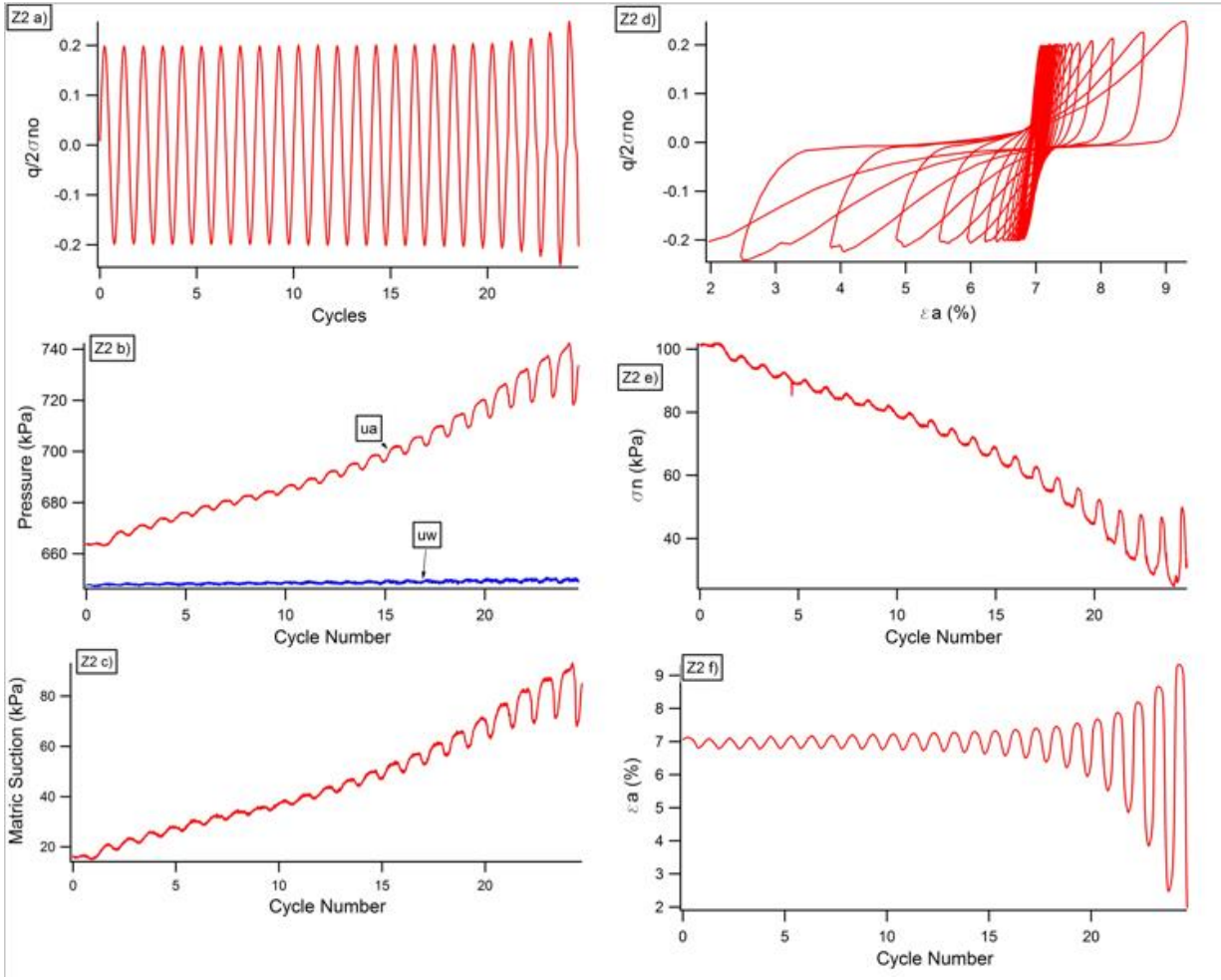

Figure A.10 – Test data for test Z2

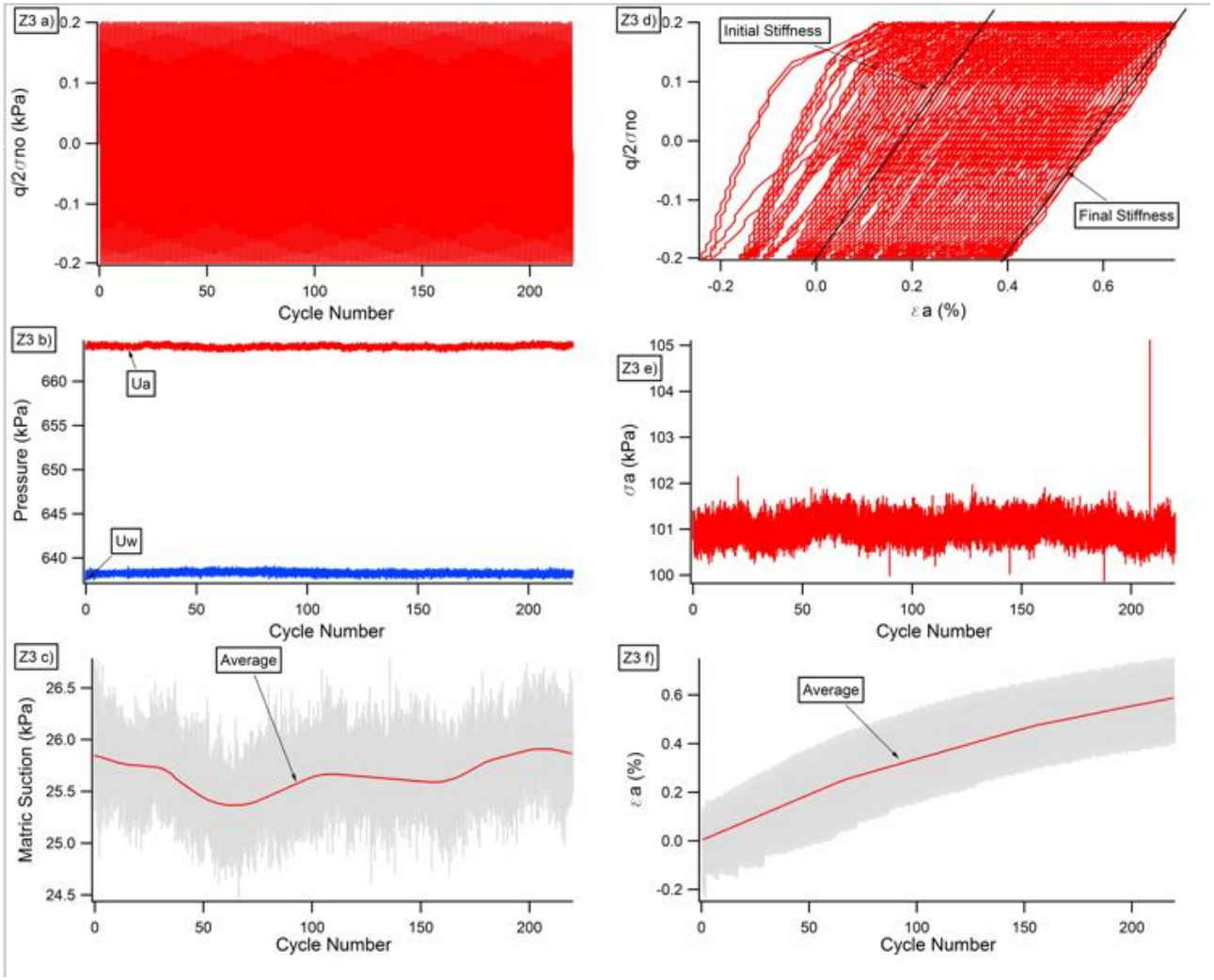

Figure A.11 – Test data for test Z3

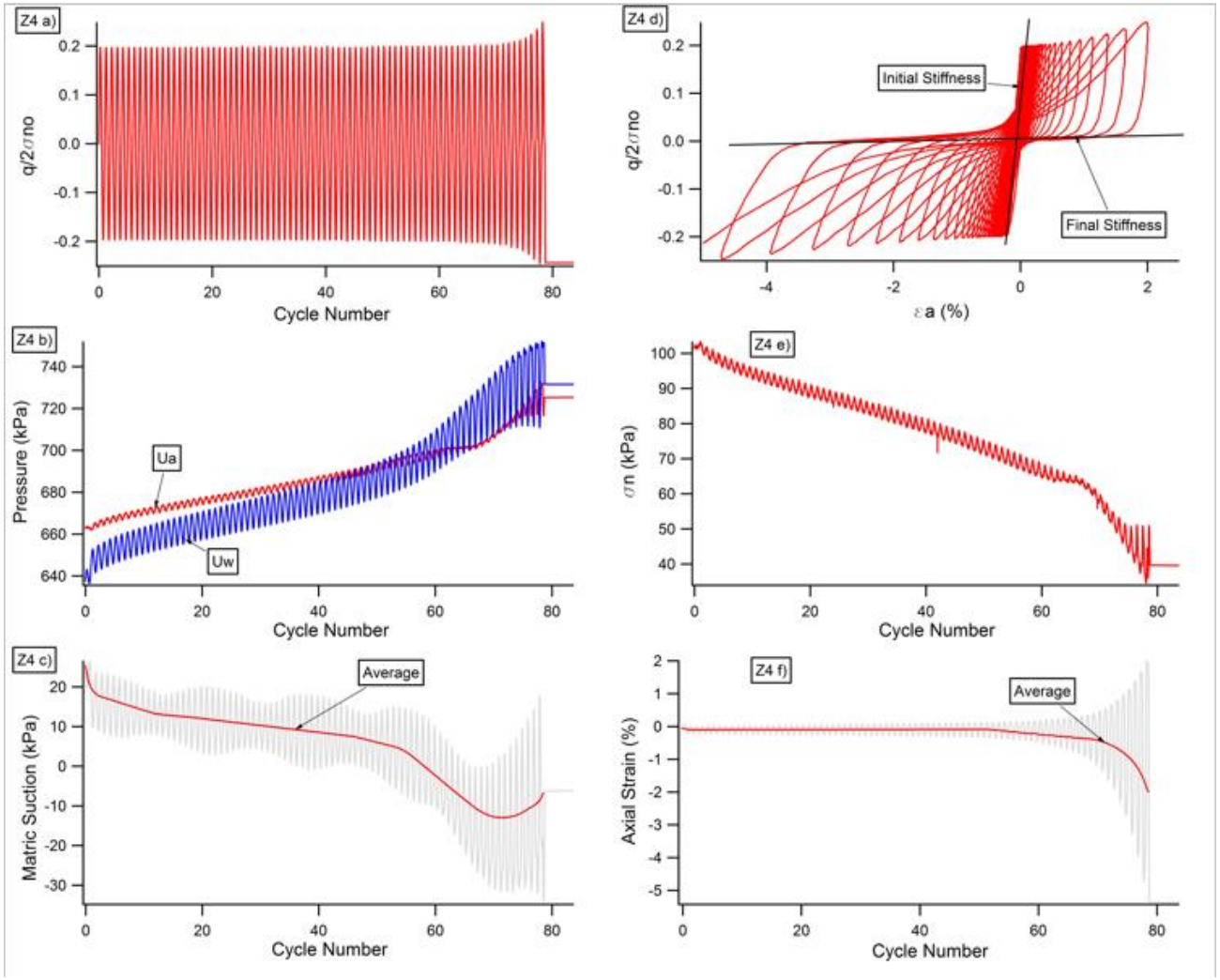

Figure A.12 – Test data for test Z4

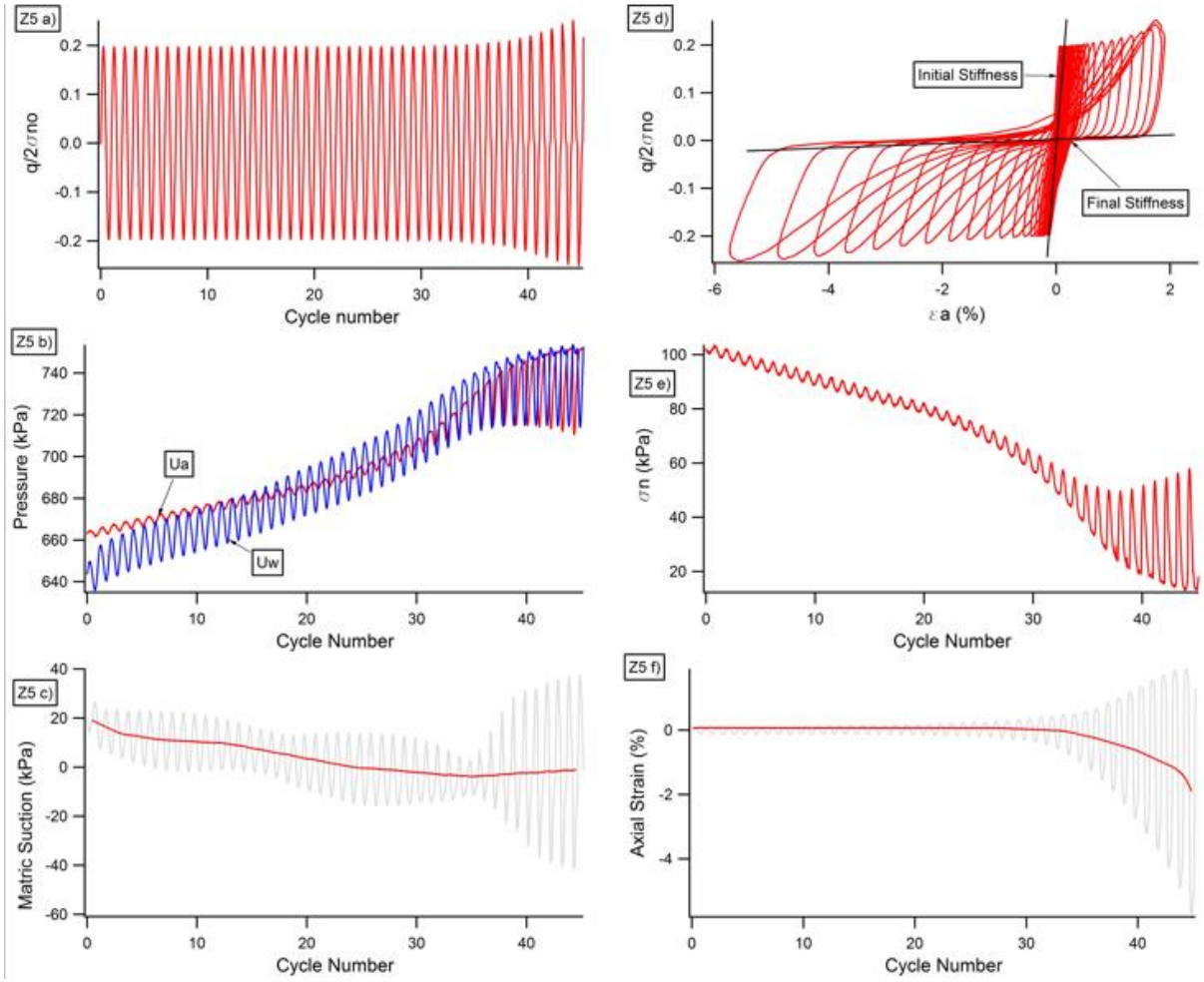

Figure A.13 – Test data for test Z5